

ALMA MATER STUDIORUM · UNIVERSITÀ DI BOLOGNA

---

**Scuola di Scienze**

**Dipartimento di Fisica e Astronomia**

**Corso di Laurea Magistrale in Fisica**

**BIOMECHANICAL MODELING  
OF PAROTID GLANDS MORPHING  
IN HEAD&NECK RADIATION THERAPY TREATMENTS**

Relatore:

Prof. GIUSEPPE BALDAZZI

Presentata da:

FRANCESCA ITTA

Correlatore:

Dott. GABRIELE GUIDI

Anno Accademico 2015/2016

*Alla mia famiglia*

# ABSTRACT

Head&Neck patients treated with radiation therapy during the course of the treatment (6-7weeks) are exposed to several side effects and in particular weight loss, alteration in muscle mass and radiation exposure that can induce inter-fraction deformation of the parotid salivary glands. Glands morphing makes them to move towards the centre of the neck and eventually intersect the main target volume of the therapy; as consequence parotids may be irradiated more than initially planned leading to a pathologic condition of reduced saliva flow rate known as xerostomia.

This thesis, realized at the “*Azienda Ospedialiera di Modena*” *Policlinico Medical Physics* and *Radiation Oncology* departments, as a part of a *Ministry of Health* research project, aims to handle the challenge of creating a biomechanical model of parotid gland morphing process, whose implementation could be useful for an adaptive radiation therapy (*ART*) protocol to take it into account, in terms of dose reduction to these structures. *ART* is a novel radiation therapy technique that includes human body temporal changes in anatomy during imaging, planning and delivery phases in order to personalize radiation treatment following patient organ motion over all treatment course.

The proposed biomechanical model has been computationally implemented due to the finite element software (*FEM*) COMSOL<sup>®</sup> multiphysics. Definition of soft tissue elastic behaviour, model fixed constraints and force field that causes parotid deformation, has required the understanding of parotid gland anatomy and radiosensitivity. The real phenomenon of parotid morphing is very complex involving several different effects and structures which interact with the gland; for these reasons some simplifications have been made considering acinar cells loss and gland surrounding structures.

The implementation of the biomechanical model of parotid morphing process, requires an initial phase consisting in the creation of 3D gland meshes from patient Computed tomography images. Mesh creation process has been realized by using the treatment planning system RayStation<sup>®</sup> and the medical images visualization software 3D Slicer<sup>®</sup>. RayStation<sup>®</sup>, by using a Python scripting procedure involving rigid and deformable registration, is able to automatically re-contour structures of interest on patient daily Megavoltage Computed Tomography (*MVCT*) images using contours traced by radiation oncologists at planning time. These contours will be used to create parotid meshes by using *marching cube* algorithm. The biomechanical model simulations performed, are able to represent parotid slimming process due to structural changes caused by radiation exposure, highlighting that facial slimming and tumour shrinkage play a key role in parotid gland morphing especially in the last part of treatment. The availability of parotid gland mesh surfaces for the whole treatment duration, allows us to make some quantitative analysis in order to investigate about the dynamic of parotid morphing and identify regions that experience the greatest pattern of deformation.

# SUMMARY

<b>Introduction .....</b>	<b>1</b>
<b>1. Radiation therapy treatments and organ morphing.....</b>	<b>5</b>
1.1 Conventional radiation therapy workflow .....	5
1.2 Display dose distribution: dose-volume histogram .....	8
1.3 Organ morphing and adaptive radiation therapy .....	10
1.4 Case of study: parotid morphing in Head&Neck patients .....	15
1.4.1 Parotid gland anatomy and radiosensitivity.....	16
1.4.2 Parotid gland morphing: state of art .....	20
1.5 Modeling organ morphing : statistical and biomechanical approaches.....	23
<b>2. Image based organ mesh creation .....</b>	<b>27</b>
2.1 Surface mesh creation workflow .....	27
2.2 Data acquisition .....	30
2.2.1 Tomotherapy .....	31
2.2.2 Image data set : kVCT vs MVCT .....	32
2.3 Automatic re-contouring.....	35
2.3.1 Image registration .....	35
2.3.1.1 Rigid registration: Mutual information algorithm .....	37
2.3.1.2 Deformable registration : The ANACONDA algorithm .....	39
2.3.2 Automatic re-contouring implementation.....	41
2.4 Contours to mesh conversion: marching cube algorithm .....	43
2.5 Mesh quantitative analysis.....	47
<b>3. FEM biomechanical model of parotid morphing .....</b>	<b>52</b>
3.1 Finite element modeling of parotid gland morphing .....	52
3.1.2 Continuum Mechanics and soft tissue .....	53
3.1.3 Introduction to the finite element method .....	56
3.2 FEM workflow implementation into COMSOL® multiphysics.....	59

3.2.1 Setting up geometry and materials .....	60
3.2.2 Loading and boundary conditions .....	62
3.2.3 FEM volumetric mesh generation .....	64
3.2.4 Run study and display results .....	66
3.2.5 Workflow of the simulations .....	67
<b>4. Results .....</b>	<b>69</b>
4.1 Quantification of parotid glands morphing.....	69
4.2 Accuracy of surface reconstruction .....	78
4.3 FEM biomechanical model results .....	80
<b>5. Future Challenges .....</b>	<b>87</b>
<b>6. Conclusions .....</b>	<b>90</b>
<b>Appendix 1.....</b>	<b>92</b>
Maths of FEM.....	92
<b>Appendix 2.....</b>	<b>96</b>
Slicer Python script.....	96
<b>Appendix 3.....</b>	<b>97</b>
Displacement maps .....	97
<b>Appendix 4.....</b>	<b>105</b>
FEM model results : morphed meshes .....	105
<b>Appendix 5.....</b>	<b>113</b>
Maths of statistical shape based model and Matlab code .....	113
<b>Sitography .....</b>	<b>118</b>
<b>Bibliography .....</b>	<b>119</b>
<b>Acknowledgement .....</b>	<b>123</b>

# INTRODUCTION

The conventional radiotherapy clinical workflow is based on the assumption that the simple re-positioning of the human body is sufficient to ensure adequate daily reproduction of the planned geometry through the course of fractionated radiotherapy treatment. However the human body is a dynamic system subject to temporal changes in anatomy due to physiological processes such as tumour shrinkage, weight loss or internal organ motion that the standard radiation therapy planning system doesn't take into account.

Given the steep dose gradients around the tumour volume reachable with intensity modulated and image guided radiation therapy (*IMRT/IGRT*) techniques, internal movements of organs during treatment may cause two possible scenarios: insufficient dose coverage of the targeted tumour volume or an over dosage of normal tissues. Both cases potentially compromise the clinical results of the treatment. It is therefore important to consider the extent and patterns of organ motion.

All these issues have led to the concept of image guided adaptive radiation therapy (*ART*): a radiation therapy technique that includes patient temporal changes in anatomy during imaging, planning and delivery phases.

In this context the present work focuses on one of the main organs involved in anatomical change in shape in head&neck (*H&N*) district and which plays a relevant role in the quality of life of patients: parotid salivary glands.

Several studies quantifying anatomic variations of parotid glands during conventional *RT* treatments, generally agree that parotids are subject to a volume shrinkage process with a shift of the centre-of-mass toward the midline that makes them to move towards the centre of the neck and eventually intersect the main target volume of the therapy. As a consequence dose received by parotids during *RT* treatment is greater than the planned one; this can lead to a pathologic condition of reduced saliva flow rate known as xerostomia.

The aim of this work was to handle the challenge of creating a biomechanical model of parotid gland morphing so that receiving in input parotid 3D mesh geometry at the start of treatment, it could be possible to say how its shape will change during treatment course. The biomechanical model of parotid gland morphing process could be useful for an *ART* protocol to take it into account in terms of dose reduction to these structures.

This work has been developed at “Azienda Ospedaliera di Modena” Policlinico Medical Physics Department, within a Ministry of Health research project named “Dose warping methods for IGRT and ADAPTIVERT: dose accumulation based on organ motion and anatomical variations of the patients during radiation therapy treatments”, whose aim is to develop novel techniques in the field of ART.

The computational implementation of our biomechanical model consists in solving continuum mechanics problems under consideration of material elastic properties and other environmental constraints. The definition of gland elastic behaviour, fixed constraints and force field responsible for parotid deformation has been a challenging task due to the complexity of the phenomenon investigated which involves several touching and interacting structures such as: mandible, muscles, ducts, veins and arteries. From literature search comes up that the loss of acinar cells that fill parotid lobuli is one of the main reasons for parotid morphing in radiotherapy patients. This effect has been introduced in our model as a force field acting on each parotid surface mesh element along normal direction in order to mimic lobuli shrinkage process. Fixed constraints have been placed taking into account the role of gland touching structures during its shrinkage process. Parotid soft tissue has been modelled as a linear elastic material.

The numerical method used to solve the physically based model of deformable glands is the finite element method (*FEM*): it represents the ultimate state of the art technique in physically based modeling and simulation when solutions of continuum mechanics problems defined over complex geometry, such as parotid one, have to be found. The optimal model parameters able to reproduce parotid shrinkage process, have been estimated by comparing pattern of deformation obtained from *FEM* simulations with the real one observed. Our model is able to correctly represent parotid volume reduction due to loss of acinar cells and results obtained point out that patient weight loss and tumour shrinkage play a key role in parotid morphing especially in the last days of treatment.

This thesis work is divided in six chapters:

- *Chapter 1*: it describes the problem of organ motion in radiation therapy treatments with particular regard about parotid gland morphing in head&neck patients. The normal anatomy and radiosensitivity of parotid is reported with an overview of the principal studies that have focused on quantifying parotid change in shape during *RT* treatments and its dosimetric consequences. Different approaches to model organ deformation are listed followed by the description of the implemented workflow.

- *Chapter 2*: it focuses on the workflow implemented in order to create each patient parotid mesh starting from image data acquisition of our tomotherapy patients. Steps necessary to implement automatic re-contouring process and mesh creation procedure are reported. At the end of this chapter we introduce some quantitative indices that will be used to compare real deformed parotid meshes with the simulated ones.
- *Chapter 3*: it contains an introduction to the finite element method with a focus on the aspects that have been relevant in the implementation of parotid morphing model within COMSOL<sup>®</sup> multiphysics environment such as: definition of soft tissue elastic model and parameters, model fixed constraints, loading conditions and volumetric *FEM* mesh creation.
- *Chapter 4*: it contains results of *FEM* model implementation with some quantitative analysis performed to characterize the dynamic of parotid slimming process.
- *Chapters 5-6*: they contain future challenges that we hope to solve in order to improve the performance of our model followed by conclusions.





# 1. RADIATION THERAPY TREATMENTS AND ORGAN MORPHING

## 1.1 CONVENTIONAL RADIATION THERAPY WORKFLOW

Radiation therapy uses ionizing radiation for cancer cells killing. It works due to the ability of ionizing radiation to produce DNA damages; tumour cells unlike healthy ones are not able to repair this type of damage whose accumulation leads them to stop growing and death.

The goal of radiation therapy is to deliver the maximum amount of radiation needed to kill the cancer cells, while sparing normal surrounding tissues. To accomplish this goal, radiation therapy relies on physics, radiobiology and computer science. The technological and medical advances made during the last decades have thrust radiation therapy into a new era, in which the highest level of accuracy and the ability to greatly reduce dose to normal tissues is possible. Numerous methods to deliver radiation exist such as:

- **3D-conformal radiation therapy (3D-CRT):** radiation therapy technique that uses patient's medical images such as Computed tomography (*CT*) images or Magnetic resonance (*MRI*) images to create a precise 3D model of the tumour used by a computer to set multi-leaf collimator (*MLC*) so the radiation beam matches tumour shape.
- **Intensity modulated radiation therapy (IMRT):** a 3D conformal radiotherapy approach that allows for the radiation beam produced by a medical linear accelerator to conform precisely to the 3D shape of the tumour by modulating its intensity in multiple small volumes using multi-leaf collimator.
- **Image-guided radiation therapy (IGRT):** all the radiation therapy treatment approaches that incorporate imaging techniques during each treatment phase. Its implementation makes it easier to monitor for anatomic modifications that may cause significant differences between planned and delivered dose distributions and make possible to correct systematic error in patients set up.
- **Intra operative radiation therapy (IORT):** it is a cancer treatment form where the radiation is delivered directly to a small area of the body, all at once directly to the tumour bed in the surgery room, right after the tumour has been surgically removed.

- **Volumetric modulated arc therapy (VMAT):** it is an advanced form of *IMRT* that delivers a precisely sculpted 3D dose distribution with a 360-degree rotation of the gantry in a single or multi-arc treatment. Unlike conventional *IMRT* treatments during which the machine delivery using fixed gantry and step and shoot methods or dynamic motion of the *MLC*, *VMAT* can deliver the dose to the entire tumour in a 360-degree rotation, typically in less than two minutes.
- **Stereostatic radiation therapy (SRT):** it allows to administer a high radiation dose to a localized volume sparing the surrounding healthy tissues, in a single or few sessions. With/without the aid of immobilization devices it can be performed with linear accelerators on both cranial and extra cranial target.
- **Tomotherapy, or Helical Tomotherapy (HT):** it is a form of *IGRT/IMRT* treatment characterized by a radiation delivery system which differs from older techniques where one or more radiation field would encompass the entire tumour resulting in significantly more radiation to normal structures. In Tomotherapy radiation is delivered slice-by-slice. In addition to its ability to deliver a highly conformal dose distribution, *HT* is equipped with xenon detectors that have been designed to obtain the Megavoltage computed tomography (*MVCT*) images that are used for pre-treatment patient set-up verification and dose delivered.
- **Proton/Hadron therapy:** it is a form of external beam radiation therapy using radiation beams produced by protons/carbon ions. The strength of hadron therapy relies in the peaked shape of hadron energy deposition that allows a precise definition of the region to be treated. Its implementation requires cyclotron and synchrotron.

Conventional *IGRT/IMRT* treatment workflow (*fig.1*) consists of several phases:

- **Treatment simulation:** its aim is to build patient virtual model
- **Treatment planning:** its aim is to perform virtual treatment
- **Treatment delivery:** its aim is to deliver planned dose distribution to the patient

*Simulation* phase starts with the acquisition of a *CT* image set for diagnostic and modeling purpose several days before radiation treatment delivery begins. A radiation oncologist traces contours of tumour area (*target*) and nearby healthy organ at risk (*OAR*) on the slices of the *CT* image data set and determines the total radiation dose that will be delivered to the target, taking into account the amount of radiation that normal tissue can safely receive. The manual target segmentation performed by the radiation oncologist,

defines regions such as the clinical target volume (*CTV*) which includes not only the contrast enhanced regions visible on cross-sectional images (the gross target volume (*GTV*)) but also suspected tumour burden at a microscopic level at the periphery of the *GTV*. *CTV* is typically further expanded to generate a planning target volume (*PTV*) that accounts for setup and motion uncertainties. During the simulation phase it is important to address to the patient coordinates (Cartesian, DICOM or absolute) on reproducible points. For this reason simulation phase involves the design of immobilization devices such as body molds and head mask to insure stable and reproducible positioning of the patient. During the **planning** phase the optimal radiation field configuration capable to produce the desired dose distribution is established by a medical physician by using a treatment planning system (*TPS*): a software which combine organ of interest contours, radiation transport simulations and optimization algorithms. Evaluating results obtained with *TPS* (see 1.2), the radiation oncologist authorizes the start of treatment **delivery**. Total dose necessary for cancer cell killing is usually fractionated for radiobiological purpose (normal cell repair, tumour cell oxygenation), so the cycle of therapy delivery can take up 6-7 weeks. Before each fraction of dose is delivered, a *CT* image set is acquired from a scanning technology implemented in the treatment delivery machine and a daily *rigid-registration* (see 2.3) with the planning *CT* is performed to correct patient position reducing systematic errors in reproducing planning set up.

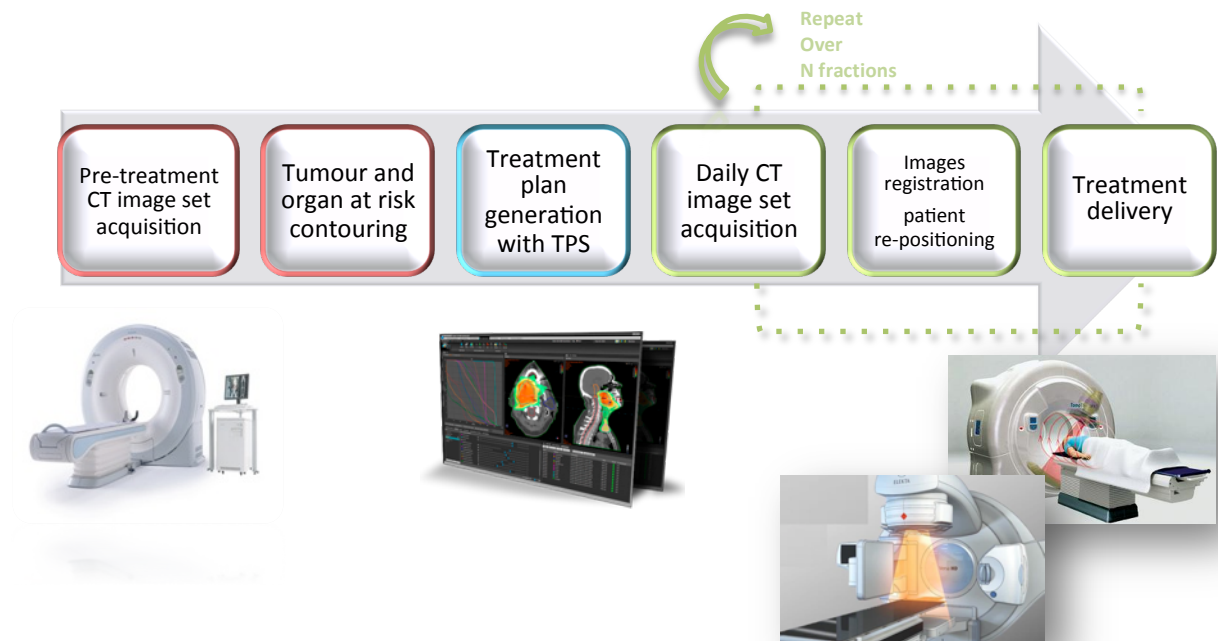


**Figure 1:** Schematic representation of the conventional IMRT/IGRT radiation therapy clinical workflow

## 1.2 DISPLAY DOSE DISTRIBUTION: DOSE-VOLUME HISTOGRAM

A graphical representation of the dose that is received by normal tissues and target volumes within a radiation therapy treatment can be obtained by:

- **Iso-dose contours/surfaces:** sets of closed contours/surfaces linking voxels receiving equal amount of dose. It is the most direct and informative method of assessing a treatment plan but it involves a huge amount of information to assess and it is difficult to quantify. An iso-dose distribution super positioned over Computed tomographic (*CT*) data is often insufficient to provide quantitative data for the radiation oncologist to determine the adequacy of a patient treatment plan.
- **Dose-volume histogram (DVH):** histogram, which provide information on the volume of a structure receiving a given dose over a range of doses. This graphical representation it's capable to quantify information about dose distribution but it offers no spatial information (*DVH* does not show where within a structure the dose is received). Dose–volume histograms provide key information to radiation oncologists when they assess the adequacy of a patient treatment plan in radiation therapy.

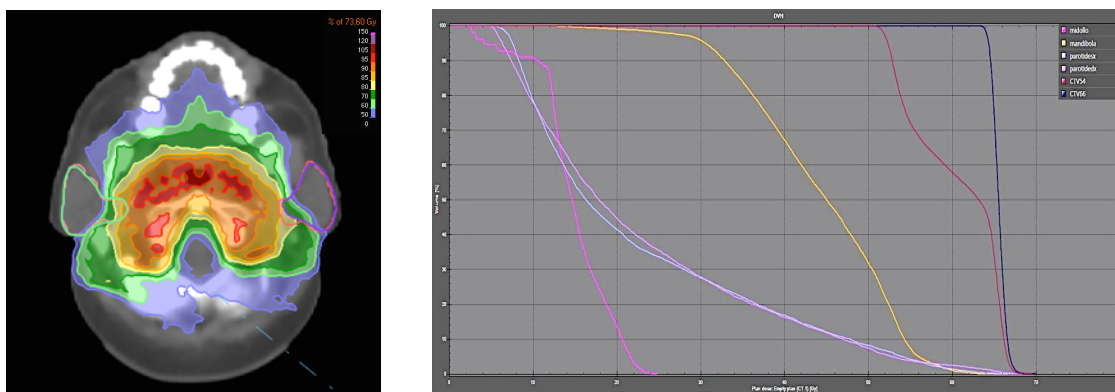


**Figure 2:** Iso-dose (left-box) contours displayed in colour washed and super positioned over axial view of CT images where parotid salivary glands of an head&neck patient are contoured. (Right-box) Head&neck structures of interest integral DVHs (RayStation®).

To form a *DVH* for any structure of interest it is necessary to look at the dose value for each voxel belonging to it and form a histogram counting the number of voxels that receive each dose level. Knowing the volume of each voxel, the volume of the organ receiving each dose level is known. The volume (vertical) and dose (horizontal) axes can be displayed in absolute terms (as cubic centimetres [*cc*] or Gray [*Gy*]) or in relative terms (*%volume* or *%dose*) depending on how planner wants to analyse the results.

DVH can be displayed in two ways:

1. **Differential DVH:** it is a histogram constructed using the sum of the number of voxels covered by a specific range of dose for the considered organ. It is helpful in providing information regarding dose changes within the structure considered.
2. **Cumulative or Integral DVH:** it is a function expressing the structure's volume that receives at least a certain amount of dose. It is calculated as the integral of the differential DVH and due to its intuitiveness it is used more than the differential DVH.

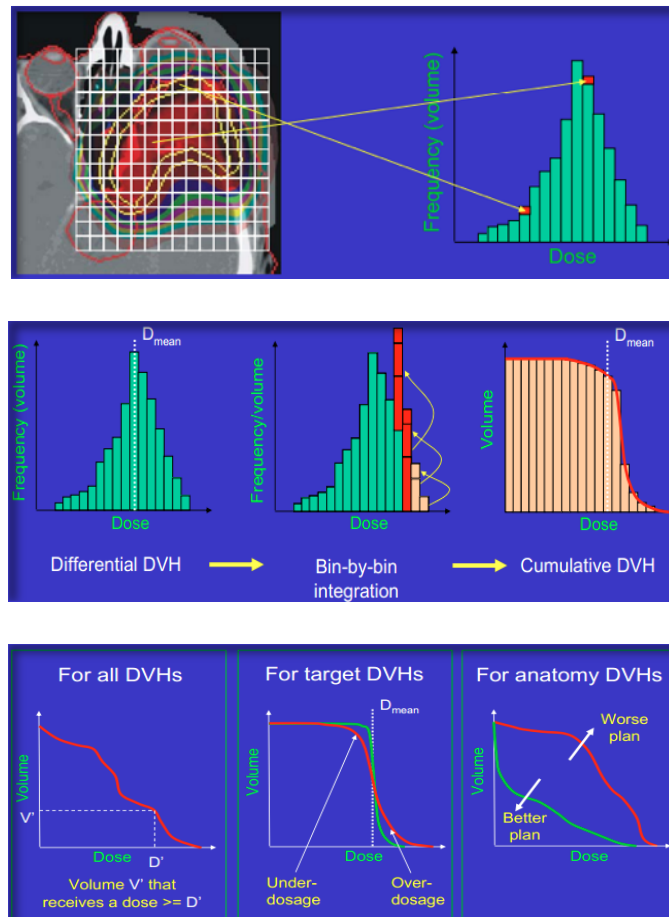


**Figure 3:** Schematic representation of differential and integral DVH calculation for a specific structure of interest<sup>1</sup>

DVHs from radiotherapy plan gives information about the doses that will be delivered to structures of interest. As treatment progresses and time elapses differences between actual and planning DVHs can arise due to organ motion as discussed in the following section.

<sup>1</sup> Images taken from [http://www.sasro.ch/SRO/TPS\\_Evaluation.pdf](http://www.sasro.ch/SRO/TPS_Evaluation.pdf) accessed on 11 June 2016

### 1.3 ORGAN MORPHING AND ADAPTIVE RADIATION THERAPY

The conventional radiotherapy clinical workflow described in 1.1 is based on the following assumption: the simple re-positioning of the human body is sufficient to ensure adequate daily reproduction of the planned geometry through the course of fractionated radiotherapy treatment. But the human body is a dynamic system subjected to temporal changes in anatomy due to physiological processes such as tumour shrinkage, weight loss or internal organ motion (peristaltic movement, bladder filling, respiratory movements, etc.) that the standard radiation therapy planning system doesn't take into account.

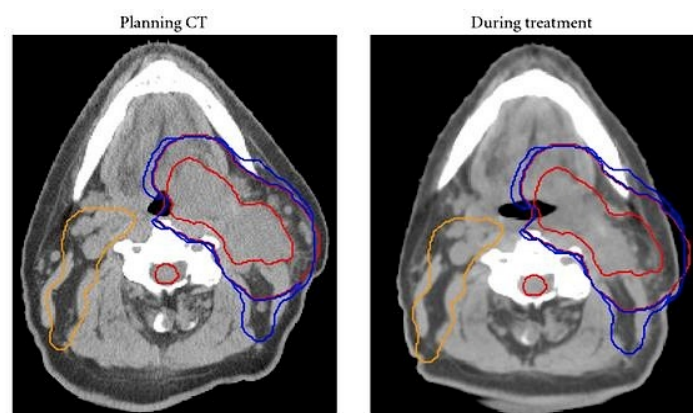


*Figure 4: An example of inter-fraction organ motion due to tumour shrinkage<sup>2</sup>*

Given the steep dose gradients around the tumour volume reachable with *IMRT/IGRT* planning, internal movements of organs during treatment may cause two possible scenarios: insufficient dose coverage of the targeted tumour volume or an over dosage of normal tissues. Both cases potentially compromise the clinical results of the treatment. It is therefore important to consider the extent and patterns of organ motion. In radiation therapy treatments phenomena of organ motion [1] are usually classified in terms of time scale in:

- **Intra-fraction organ motion:** organ changes in shape and position due to processes whose effects are significant even within the time frame of a single treatment session. The principal causes of this type of movements are the respiratory cycle, cardiac contraction, aortic pulsation and swallow. Among these factors breathing is the primary cause of organ intra-fraction motion, which affects mainly organs of the thorax and abdomen.

<sup>2</sup> Image taken from <http://www.hindawi.com/journals/jo/2011/690595/fig2/> accessed on 11 June 2016

- **Inter-fraction organ motion:** organ changes in shape and position that are visible only from a treatment session to another. The greatest part of this type of morphing relates organs belonging to the digestive system or which are next to it. A typical example is observed during treatment of the prostate cancer: in fact, position of this organ depends largely on the filling of the rectum and bladder, that causes shape changes day by day in closely correlated fashion with the intestinal functions. Inter-fraction movements are also caused by possible reductions (tumour shrinkage) or enhancements (tumour growth) of the tumour mass, rotations and translations of the same with respect to the bone structures and patient weight loss or gain due to radiotherapy or some other on-going therapies. A typical example of organ motion due to tumour shrinkage and patient weight loss regards parotid salivary glands in head&neck (*H&N*) district.

Organ deformation	Effect
Heartbeat	intra-fraction motion
Respiratory motion	intra-fraction motion
Bladder filling	inter-fraction motion
Radiation induced motion	inter-fraction motion
Weight loss/Tumour regression	inter-fraction motion

**Table 1:** Table representing organ deformations and their effects in terms of time-scale

Inter-fraction anatomic changes can be pronounced during treatment course. In the example reported in *figure 4*, planning *CT* scan and *CTV* contours of a patient with tumour in head&neck site are shown on the left. On the right, a mid-course *CT* (three weeks into treatment) demonstrates significant reduction in gross tumour (thick red line). Baseline *CTVs* have been overlaid via rigid image registration. These match current anatomy poorly and in fact extend past the skin contour into air.

Inter-fraction organ motions can occur in daily random or progressive pattern. The first are usually organ changes in anatomy related to peristaltic motion and variation of organ filling, the latter are organ motions due the progressive weight loss or tumour shrinkage.



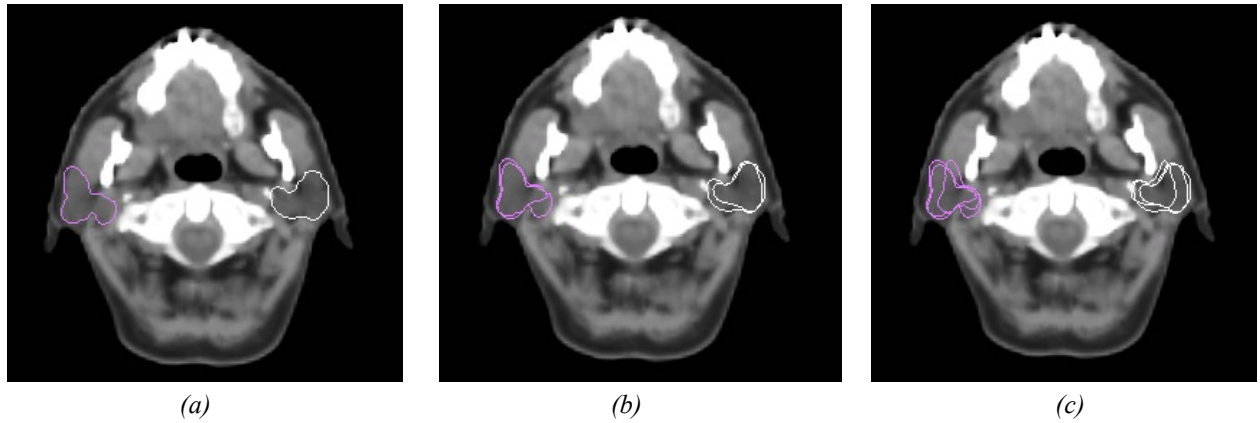


**Figure 5:** An example of inter-fraction progressive deformation of parotid glands due to patient weight loss and radiation exposure. Figure (a) shows CT image slice with PGs contours at planning time. Parotid contours at mid-course time (b) and at the end of treatment (c) have been overlaid.

Inter and intra-fraction movements can produce shape differences of organ at the time of treatment delivery relative to the time of simulation that can lead to a large variability in delivered dose. As an example we report about inter-fraction volume and dose variations of parotid salivary glands in *H&N* patients treated with Tomotherapy (see 2.2.1). It emerges that parotid glands are subject to a progressive volume reduction process (fig.5-6) that causes an over dosage of these structures compared to planning time (fig.7).

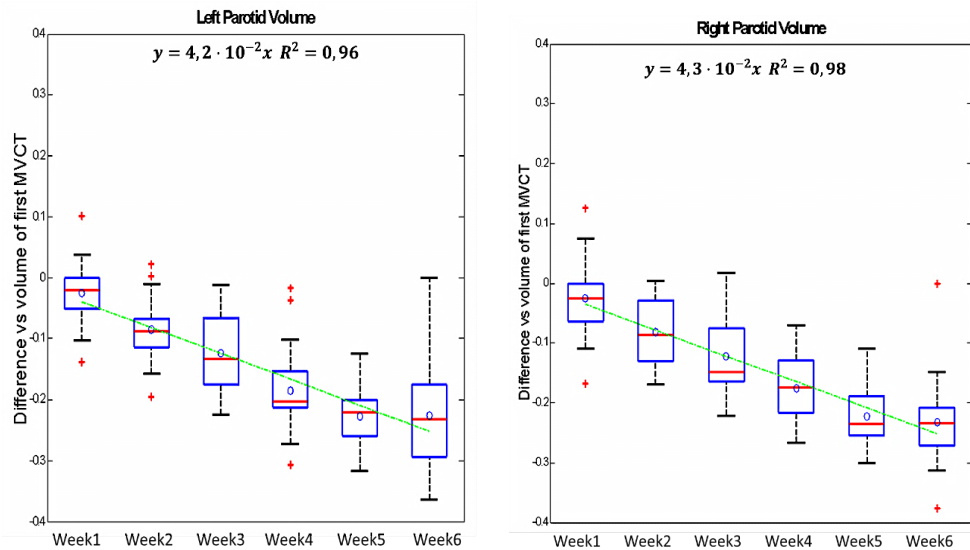


**Figure 6:** Box plots of right and left parotid glands volume variations as time of treatment elapses<sup>3</sup>. The green line is the linear regression of volume variation vs. week of treatment

<sup>3</sup> Images taken from Ciarmatori A., "Dose accumulation in head and neck cancer patients: through implementation of Adaptive Radiotherapy in clinical practice", Medical Physics School University of Bologna, 2015. [2]

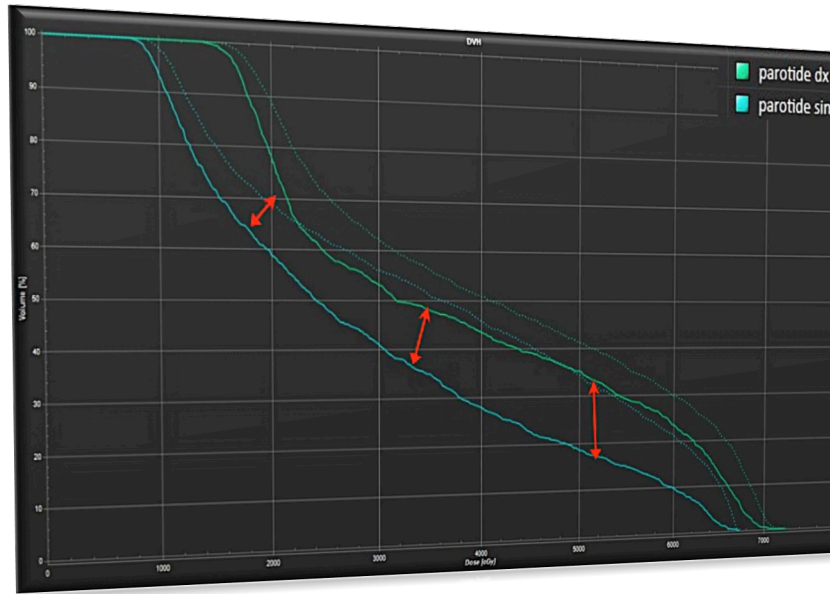


**Figure 7:** Comparison of left (light blue) and right (green) parotid integral DVHs at planning time (continuous lines) and at the end of treatment (dashed lines) that clearly shows an over dosage of these structures due to their change in shape. Vertical axis shows % structure volume values, x axis shows dose value [cGy].

So, due to organ motion and deformation, especially for some anatomical site a single plan designed before treatment start is insufficient to describe the actual delivered dose and often leads to suboptimal treatments. All the described issues have led to the concept of image guided **adaptive radiation therapy (ART)**. ART is a radiation therapy technique that includes temporal changes in anatomy during imaging, planning and delivery phases [3].

The ultimate goal of ART is to personalize radiation treatment following patient anatomy over all treatment courses. In theory, ART can occur at three different time scales: off line between fractions, on line immediately prior to a fraction, and in real-time during a treatment fraction:

- **On line ART:** this approach aim is to daily re-plan and use the new plan for the current treatment session. This strategy needs high automation in contouring, planning, dose accumulation and plan verification involving software and scripting procedure for auto-planning and automatic contouring. It is suitable for inter-fraction organ motion where a non-predictable change in anatomy occurs.
- **Off line ART:** this approach aim is to re-optimize radiotherapy planning according to a trigger condition obtained from patient anatomy of the earlier days. It is suitable for that cases in which an inter-fraction movement is characterized by a progressive and predictable change in anatomy.

- Real time ART:** this approach aims to follow in real time organ motion and deformation. It needs real time imaging and high computer resources to manage movement and adapt treatment delivery. It is suitable for intra-fraction movement. Several *real-time ART* techniques were implemented that aim to synchronize the diagnostic and treatment procedures with breathing. These include deep inspiration breath holding (*DIBH*) and respiratory gating. Respiratory gating involves the administration of radiation (during both imaging and treatment delivery) within a particular portion of the patient's breathing cycle, commonly referred to as the "gate". The position and width of the gate within a respiratory cycle are determined by monitoring the patient's respiratory motion, using either an external respiration signal or internal fiducial markers. On the contrary during the *DIBH* manoeuvre, the patient must voluntarily breathe to the required threshold. Among advanced strategies to compensate breathing motion *DIBH* gating is particularly advantageous in several aspects, for hypofractionated and normofractionated *RT* of intrathoracic and upper abdominal tumours in photon and proton *RT* [41].

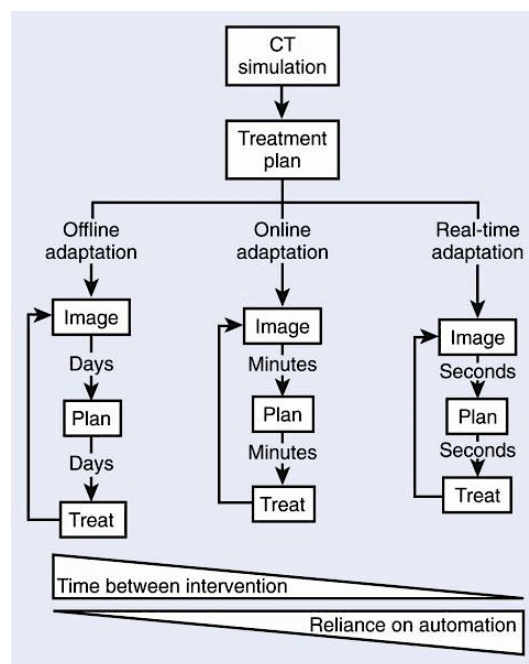


**Figure 8:** Schematic representation of ART procedure for different time scales

Modelling and prediction of organ deformation during radiotherapy treatment using daily *CT* images are highly interesting for the potential adaptation of an *ART* protocol taking these modifications into account, in terms of dose reduction to critical structures. In theory, information obtained from a system able to predict 3D organ morphing before treatment start, could be used by a *TPS* in order to optimize treatment plan taking into account the pattern of organ motion.

Especially head&neck tumour site<sup>4</sup>, due to the proximity between the *GTV* and critical organ at risk, represents specific challenges and opportunities for adaptive radiotherapy. Furthermore organs at risk such as parotid glands, have know to shrink progressively and considerably over the course of a fractionated treatment, so they are the best candidates to be studied in order to develop a predictive model.

#### 1.4 CASE OF STUDY: PAROTID MORPHING IN HEAD&NECK PATIENTS

Head&neck<sup>4</sup> patients treated with *RT* during the course of the treatment (6-7weeks) are exposed to several side effects and in particular weight loss, alteration in muscle mass and radiation exposure that can induce inter-fraction deformation of parotid glands. Parotid glands are the major salivary glands localized on either side of the mouth and responsible of half of the total saliva secretion. The deformation of parotid glands during *RT* treatments makes them to move towards the centre of the neck and eventually intersect the main target volume of the therapy (*fig.9*). As consequence parotids may be irradiated more than initially planned leading to a pathologic condition of reduced saliva flow rate known as xerostomia. In this section, an essential overview of the normal anatomy, functionality and radiosensitivity of parotid glands is reported, followed by an overview of the principal studies that have focused on parotid gland anatomic changes during conventional *RT* treatment and their dosimetric consequences.

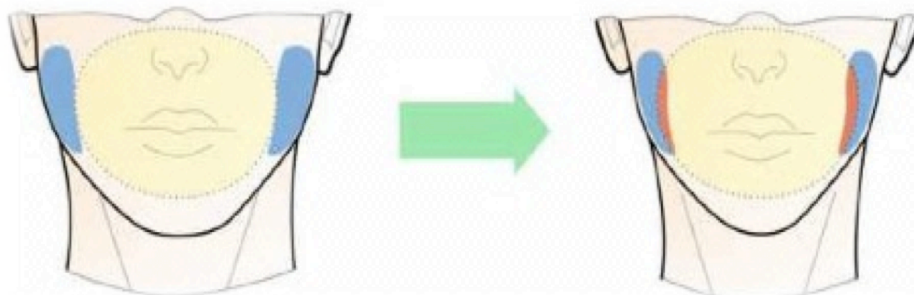


**Figure 9:** Schematic representation of parotid glands (blue) morphing due to patient weight loss and radiation exposure which cause intersection of these structures (orange) with the planning target volume (PTV in yellow).

<sup>4</sup> Head and neck patients are patients with tumour placed in one of the following anatomical site : larynx, oral cavity, paranasal sinuses, nasal cavity, tongue. In Italy head and neck cancer accounts for about 5% of all cancer for adults age 50 years and older ([http://www.registri-tumori.it/PDF/AIOM2015/I\\_numeri\\_del\\_cancro\\_2015.pdf](http://www.registri-tumori.it/PDF/AIOM2015/I_numeri_del_cancro_2015.pdf))

### 1.4.1 PAROTID GLAND ANATOMY AND RADIOSENSITIVITY

Three major pairs of salivary glands exist in human: parotid glands, submandibular and sublingual glands. We will now introduce several aspects of parotid gland anatomy that have been relevant in the development of our biomechanical model and that will be useful to localize gland regions subjected to deformation during conventional *RT* treatment. Parotids are the largest salivary glands and are located in the space that extends:

- Medially to the paraharyngeal space
- Anteromedially to the masticator space
- Posteromedially to the mastoid tip

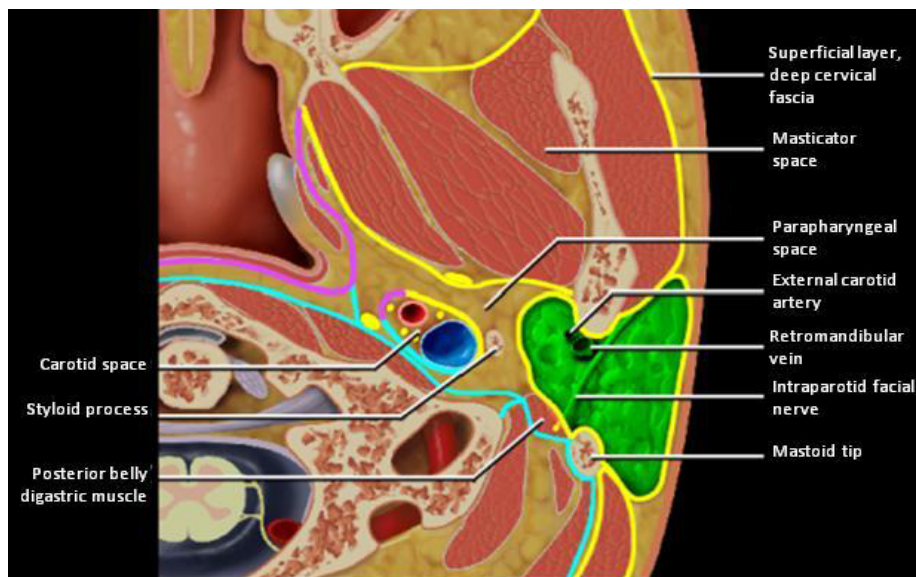


**Figure 10:** Axial graphic of the parotid space (PS) in green at the level of C1 vertebral body. The PS contains from medial to lateral the external carotid artery, retromandibular vein and facial nerve. The intraparotid Cranial Nerve (CN7) creates a surgical plane that divides the gland into superficial and deep lobes. The superficial layer of the deep cervical fascia encloses PS. Figure from Amirsys reference centers.

Parotid glands can be partitioned into deep and superficial lobe; despite this definition, there is actually no anatomic separation between these portions. By convention, parotid tissue situated deep to the facial nerve is referred as the deep lobe, while parotid tissue superficial to this plane is considered to be the superficial lobe. Another possible division of parotid portions can be done with respect to the mandible: parotid tissue external to the mandible is referred to as superficial, whereas the smaller amount of parotid tissue that resides behind and deep to the mandible is referred to as the retromandibular or deep portion of the parotid gland.

Different structures pass through the gland. From lateral to medial, the principal are:

- Facial nerve
- Retromandibular vein
- External carotid artery

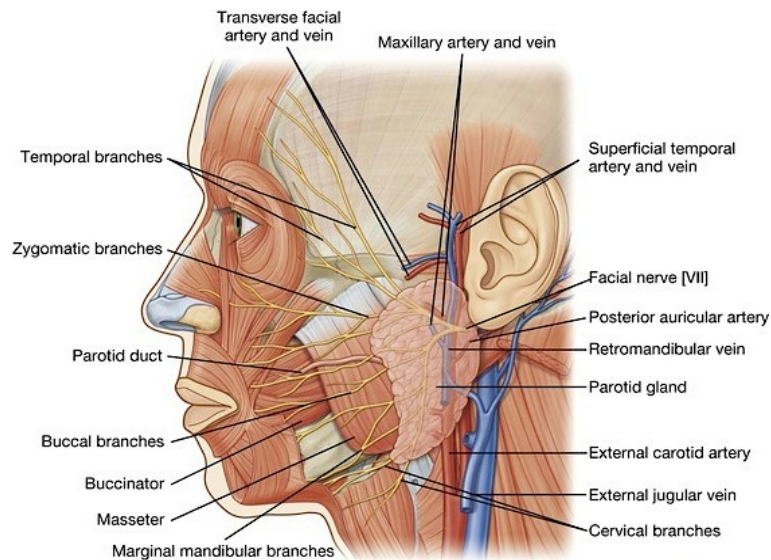


**Figure 11:** A representation of parotid anatomy where principal structures passing through it are visible<sup>5</sup>

Each parotid is wrapped around the mandibular ramus, and secretes saliva through the parotid duct into the mouth. The duct pierces the buccinator muscle, and then opens into the mouth on the inner surface of the cheek, usually opposite the maxillary second molar. From a structural point of view parotid gland is internally divided into lobules.

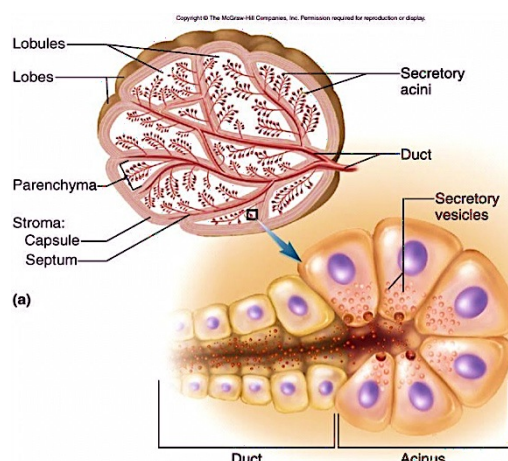


**Figure 12:** Parotid gland lobular organization.<sup>6</sup>

<sup>5</sup> Image from Drake R. et al : Gray's anatomy for students, ed. 2, Philadelphia, Churchill Livingstone, 2010, Elsevier.

<sup>6</sup> Source: Mesher AL: Junqueira's Basic Histology: Text and Atlas, 12<sup>th</sup>

Each salivary gland lobule contains secretory cells that form acini. Each acinus consists of a single layer of cuboidal epithelial cells surrounding a lumen, a central opening where the saliva is deposited after being produced by the secretory cells (*fig.12*). The acini can be of serous, mucous or mixed type. Parotid gland lobules may also contain adipose cells that in histologic exam appear as clear oval structures surrounding acinar cells (*fig.13*). To develop a proper biomechanical model it has been necessary to investigate about the radiosensitivity of these organs, in order to understand their structural changes in response to radiation exposure. As highlighted by texture analysis [4], histological studies [5] and ultrasound (US) imaging technique [6], during conventional *RT* treatment parotid of *H&N* patients are subject to a reduction of structural complexity mainly due to damage and loss of acinar cells<sup>7</sup>. The acinar cells loss occurs with a glandular shrinkage.

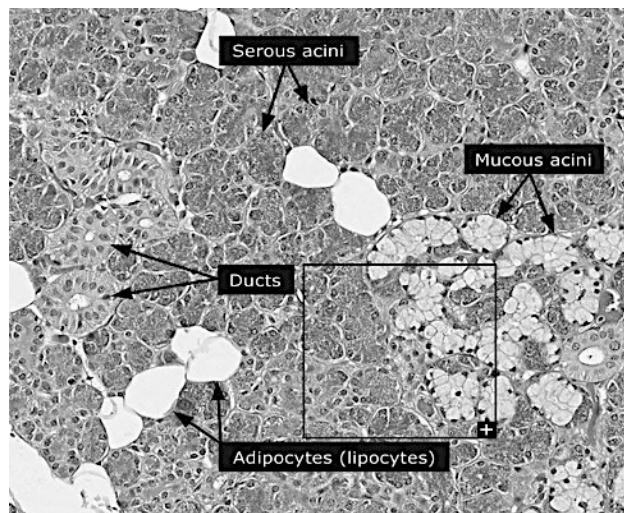
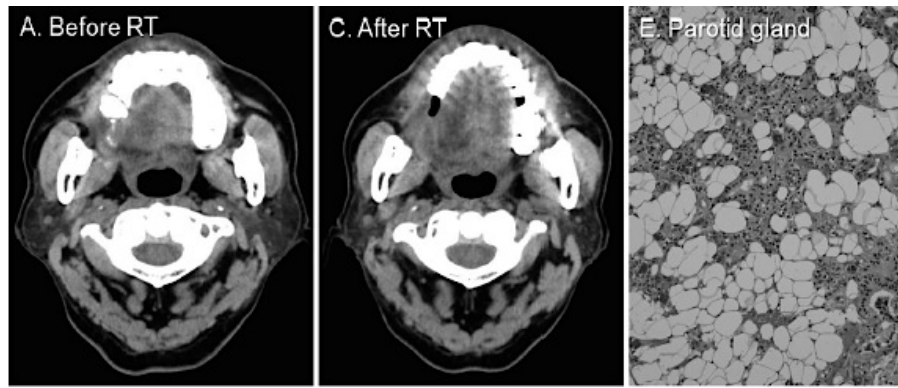


**Figure 13:** Histopathological slide of a non-irradiated and healthy parotid gland. Ducts, acini and adipocytes are highlighted<sup>8</sup>

Histopathological comparisons [5] of control subjects (selected from a group of non-pre-treated patients who had undergone neck dissection for head-and neck cancer) with *RT* patients treated with a total dose of 30 Gy delivered in daily fraction of 2 Gy over the course of 2 weeks, shows that a substantial reduction of acinar cells ratio (1.1%) occurred in *RT* patients while other tissues remain almost unchanged (*fig.14*).

<sup>7</sup> “Salivary glands are extremely sensitive to radiation, yet, unlike classically radiosensitive tissues, they proliferate slowly and are made up of highly differentiated cells. The most probable mechanism of action, explaining the enigmatic high radiosensitivity for early effects, is the radiation damage to the plasma membrane of the acinar cells, disturbing receptor stimulating watery secretion. Later damage is mainly due to classical mitotic cell death and to hampered replacement capacity of the gland for secretory cells.” [43]

<sup>8</sup> Image taken from <http://www.proteinatlas.org/learn/dictionary/normal/salivary+gland/detail+1> accessed on 8 June 2016



Parameter	Control group (n = 10)	CRT group (n = 6)
Parotid gland		
Acinar cells (%)	31.5 (17.7–49.0)	1.1 (0.3–2.2)
Duct cells (%)	4.5 (2.3–7.7)	5.8 (3.3–7.0)
Adipose cells (%)	41.9 (26.0–63.3)	49.7 (14.7–80.3)
Other tissues (%)	21.1 (12.1–31.6)	43.5 (13.5–77.4)

**Figure 14:** CT images of H&N patient before and after RT with a total dose of 30Gy delivered in daily fraction of 2 Gy over the course of 2 week and histopathological slide of PG at the end of treatment showing an increase in fat ratio and reduction of acinar cells. Median acinar cells ratio in non-irradiated human salivary gland is 31.5% while in chemo-radiotherapy (CRT) patients it is 1.1%<sup>9</sup>

Xiaofeng Y. et al. [6] comparing parotids of normal subjects with parotids submitted to RT, by using ultrasound images, also suggest that acinar cells loss plays a key role in the structural changes of PGs gland of irradiated H&N patients. Tissue of normal parotid glands, filled with homogenous serous acinar cells, provide uniform and highly reflective interfaces for the ultrasound beam. After RT, the loss of acinar cells in parotids leads to a more disorganized tissue organization, appearing in ultrasound images as an heterogeneous echographic pattern (fig.15).

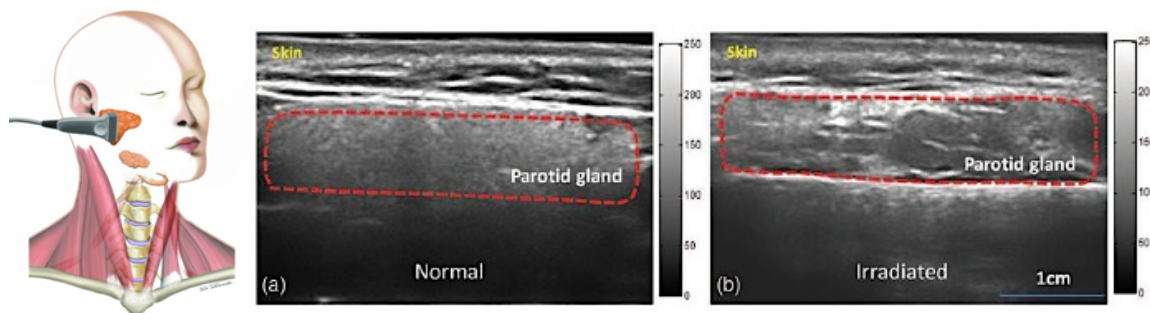


**Figure 15:** B-mode ultrasound image of the left parotid gland of a 41-yr-old healthy volunteer, revealing homogenous echotexture (a). Ultrasound image of the left parotid gland of a 52-yr-old laryngeal cancer patient, 22 months post-RT, revealing heterogeneous echotexture due to loss of acinar cells (b).

<sup>9</sup> Image and data taken from [5]



## 1.4.2 PAROTID GLAND MORPHING: STATE OF ART

With image-guidance techniques becoming more widely available, several studies have focused on anatomic variations of parotid glands during conventional *RT* treatments and generally agreed that parotid glands are subjected to 30% volume shrinkage with a shift of the centre-of-mass toward the midline that is about *3mm* at the last day of treatment. From image analysis studies [7] emerge that the voxels corresponding to larger compression values were generally more likely to be found in the posteromedial portion of the parotids; in contrast, the fraction of parotid that does not shrink or expand is generally located in the medial and anteriomedial portion of the parotid.

*Table2* summarizes the results of several studies reporting on parotid glands anatomic modifications. We performed a literature review in *MEDLINE*, *Science Direct* and *Medical Physic* using the following keywords: (synonyms for *parotid gland deformation*) *OR* (synonyms for *anatomic variations*) *AND* (synonyms for *head and neck radiotherapy*).

The search was completed by June 1, 2016. In addition, reference lists of papers were screened in order to retrieve additional relevant papers.

Author (Year)	Number of patients	Pre-treatment Imaging	Volume Analysis	Shape and positional analysis
Barker et al (2004)	14 patients	In room CT 3times/wk.	Reduction: PGs 0.6 % /day treatment	Centre of mass medially shift: 3.1 mm [0 - 9.9] mm
Hansen et al (2006)	13 patients	CT scan after a mean dose of 38 Gy	Reduction: Right PGs 15.6 % Left PGs 21.5%	Not available
Robar et al (2007)	15 patients	Weekly CT scans;	Superficial region of both PGs: 4.9 % / wk.	Medial shift: Left PGs $0.91 \pm 0.9$ mm/wk. Right PGs: $0.78 \pm 0.13$ mm/wk.
Castadot et al (2008)	10 patients	CT scan at mean doses of 14,25,35 and 45 Gy	Reduction: HomolateralPGs: 0.9%/day Heterolateral PGs: 1 %/day	Medial shift after 5 weeks of treatment: Homolateral PGs: 3.4 mm
Vasquez Osorio et al (2008)	10 patients	CT scan at 46 Gy;	Reduction after 46 Gy: Homolateral PGs:17.7% Heterolateral PGs: 5.4 %	Medial and posterior Shift after 46 Gy: Homolateral PGs 3mm
Vecchi C. (2014)	23 patients	kvCT and daily MVCT	Not available	Centre of mass medially shift: Right PG: $2.5 \pm 0.3$ mm Left PGs: $3.5 \pm 0.3$ mm
Maffei N. (2014)	23 patients	kvCT and daily MVCT	Reduction at the end of the treatment: PGs 30%	Not Available
Ciarmatori A. (2014)	23 patients	kvCT and daily MVCT	Reduction: Left PGs :4.3%/week Right PGsT 4.2 %/week	Not Available

**Table 2:** An overview of PGs change in shape in H&N patients obtained from different studies

Also the dosimetric consequences of the PGs anatomical changes have been studied.

It emerges that without any re-planning, the dose received by PGs at the end of treatment is 10% greater than the planned dose (*Table 3*).

Author (year)	Number of patients	Pre-treatment Imaging	Results
Hansen et al (2006)	13 patients	CT scan after a mean dose of 38 Gy	Right PG $V_{28Gy}$ increased by 10.9%
O'Daniel et al (2007)	11 patients	CT-on-rail 2 times/wk	Cumulative PG dose greater than planned. Median dose increase: 1 Gy
Robar et al (2007)	15 patients	Weekly CT scans;	$D_{mean}$ increase: Right PGs $0.2 \pm 4.0\%$ Left PGs $2.6 \pm 4.3\%$
Castadot et al (2008)	10 patients	CT scan at mean doses of 14,25,35 and 45 Gy	PGs $D_{mean}$ : Planned 17.9 Gy Actual 18.7 Gy
Lee et al (2008)	10 patients	Daily MVCT	PGs daily $D_{mean}$ different from the planned dose by an average of 15%
Ciarmatori A. (2014)	23 patients	Daily MVCT	Average dose increase Left PGs 2.7 %/week Right PGs 1.7 % week
Maffei N. (2014)	23 patients	Daily MVCT	PGs $D_{mean}$ different from the planned dose at the end of the treatment by an average of 10%

**Table 3:** An overview of the dosimetric impact of parotid morphing in H&N patients

Clinical data on H&N radiation therapy patients indicate that saliva production is reduced after the delivery of 10–15 Gy to the parotid gland and although functional recuperation over time is possible after irradiation with 40–50 Gy, higher doses produce irreversible and permanent xerostomia [5].

The resulting desiccant oral environment causes numerous clinical problems, including infections of the mucosa and teeth loss, impaired speech, difficulty in swallowing, reduced ability to gain nutrition, thus greatly impacting patient life quality and it may also lead to severe and long-term oral disorders.

Because management of xerostomia is rarely effective, prevention is paramount. Currently, the administration of saliva substitutes and sialogogues is the only way to treat xerostomia. However, such medications have only transient effects and must be frequently administered. Adaptive radiation therapy and tissue engineering for the creation of artificial salivary glands from culture of acinar cells [8], represent possible future solutions for such patients.

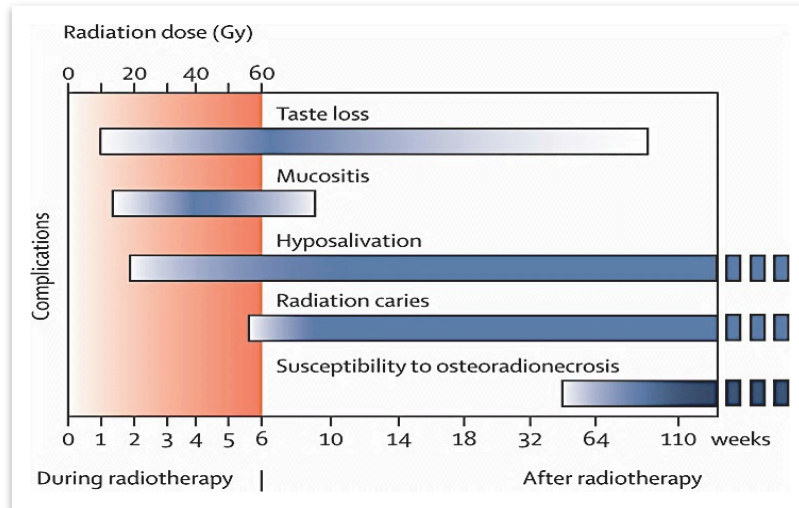


**Figure 16:** Complications affecting H&N patients with respect to time of treatment start and radiation dose delivered to parotid glands [10]

As shown in previous work developed at the “Azienda Ospedaliero Universitaria di Modena “ Policlinico [2] [11], retrospectively reviewing patient’s RT plans, adaptive radiation therapy workflow and time re-planning criteria considering PGs morphing can improve clinical result of H&N Tomotherapy treatments in terms of dose reduction to this structures (fig.17) .

As a consequence modeling and prediction of the progressive PGs shrinkage process over RT treatment duration can be useful for an ART protocol to take it into account .

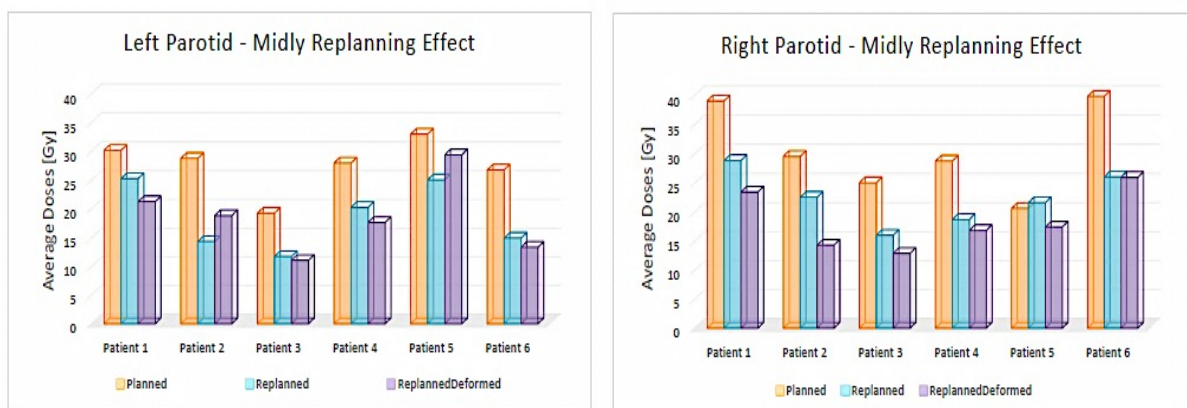


**Figure 17:** Dosimetric benefit for two different re-planning strategies showing decrease in average dose delivered to PGs compared to the one obtained by using dose distribution at planning time (orange columns). Light blue and purple columns represent results obtained by using mid-course re-planning strategies considering OAR morphing (replanned) and OAR + treatment target morphing (replanned deformed) respectively [2].

## 1.5 MODELING ORGAN MORPHING: STATISTICAL AND BIOMECHANICAL APPROACHES

Different approaches and strategies to predict parotid shrinkage in H&N patients are described in literature. Classical works studied the correlation between dosimetric features and parotid shrinkage in order to find a model for volume decrease [12]. More recent works developed models searching for predictors of parotid morphing among features extracted from *CT* images, such as parotid volume, Jacobian index, mean density or calculated from texture analysis [13-15]. Some biomechanical considerations about parotid morphing have been developed by evaluating parotid centre of mass motion [16].

However all the proposed approaches representing the whole parotid shrinkage process with a single parameter such as volume or its center of mass coordinates, don't provide any prevision about the spatial pattern of deformations. The aim of the present work is to develop a model of parotid gland motion and deformation due to radiation exposure, taking into account its 3D shape variation so that receiving in input parotid geometrical structure at the start of treatment, it could be possible to say how its shape will change during treatment course. From a general point of view 3D organ deformation can be modelled by:

- ***Statistical deformable models***
- ***Biomechanical deformable models***

The former require that the deformation of interest can be observed in a number of cases, which are treated as training samples from which a statistical predictive model is built. The latter are based on the knowledge of the biomechanical behaviour of biological tissues, the force field that causes the deformation and fixed constraints. Both methods require in input a 3D geometric representation of the deformable organ that can be obtained from *CT* images by using a mesh-creation technique. ***Biomechanical models***<sup>10</sup> are based on solving continuum mechanics problems under consideration of material properties and other environmental constraints. The biomechanical modeling of deformable organ is, in particular, of great interest for a wide range of medical imaging applications, where the realistic interaction with virtual objects is required such as virtual surgery [17]. In the last decade, various approaches and applications related to biomechanical modeling of deformable objects have been developed. These methods can be classified based on the type of the numerical technique used in the modeling approach.

---

<sup>10</sup> *Computational biomechanics is a challenging area of research combining medical imagery, computer graphics, mathematical modeling and material science to supply correct approximations to the mechanics of biological system.*

There are three common numerical methods for physically based modelling of deformable objects. These are:

- **Mass-spring-damper systems (*MSD*):** the physical body is represented by a set of mass-points connected by springs exerting forces on neighbour points when a mass is displaced from its rest positions. The major drawback of *MSD* systems is their insufficient approximation of true material properties.
- **The finite difference method (*FDM*):** the finite difference method is a discretization technique for solving partial differential equations. The general approach of the *FDM* is to replace the continuous derivatives within the given boundary value problem with finite difference approximations on a grid of mesh points that spans the domain of interest. The *FDM* achieves efficiency and accuracy when the geometry of the problem is regular.
- **The finite element method (*FEM*):** the finite element method represents the ultimate "state of the art" technique in physically based modelling and simulation. The *FEM* is superior to all previously discussed methods when accurate solution of continuum mechanics problems with a complex geometry has to be found. *FEM* subdivides a large problem into smaller, simpler, parts, called finite elements. The simple equations that model these finite elements are then assembled into a larger system of equations that models the entire problem.

Biomechanical models represent an important aspect of deformable modeling, since they utilize physical knowledge about properties of deformable organs and they give easy and quasi-realistic visual impact of organ morphing allowing to perform parametric studies and virtual experiments. However, they have two limitations. First, they require that material properties, constitutive equations, and boundary conditions are known. Second, they are computationally very demanding.

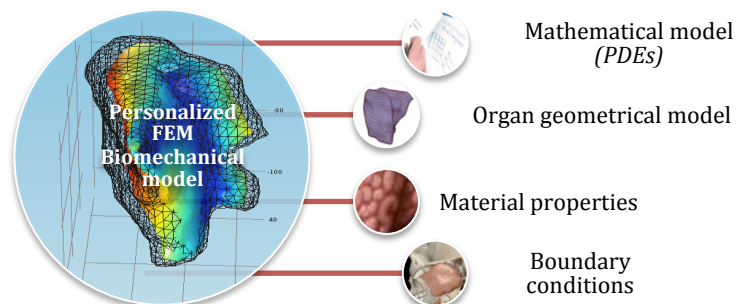


**Figure 18:** knowledge needed in order to implement *FEM* biomechanical model

An alternative approach, purely shaped-based, to model and predict organ deformation is the *statistical deformable model*. It utilizes the principal modes of co-variation between anatomy and deformation in order to statistically represent deformability.

For statistical shape model generation, the input required is a collection of 3D surfaces representing anatomy and deformation of our training shapes. Each input surface is described by a set of landmarks and stored as a single vector  $\mathbf{x}$ . The vectors of all training samples form the columns of the landmark configuration matrix  $L$ . Applying principal component analysis (*PCA*) to this matrix delivers the principal modes of co-variation  $\mathbf{p}_m$  in the training data and the corresponding eigenvalues  $\lambda_m$ . Restricting the model to the first  $c$  modes, all valid shapes  $\mathbf{x}$  can be approximated by the mean shape  $\bar{\mathbf{x}}$  and a linear combination of displacement vectors:

$$\mathbf{x} = \bar{\mathbf{x}} + \sum_{m=1}^c \gamma_m \mathbf{p}_m \quad (\text{Eq.1})$$

When presented with a new shape, which corresponds to the anatomy of an organ, its deformation can be predicted in terms of the principal eigenvectors via an optimization procedure (see Appendix 5).

The main challenge of the statistical deformable model is the point correspondence problem in the model construction phase: on every training sample for the model, landmarks have to be placed in a consistent manner.

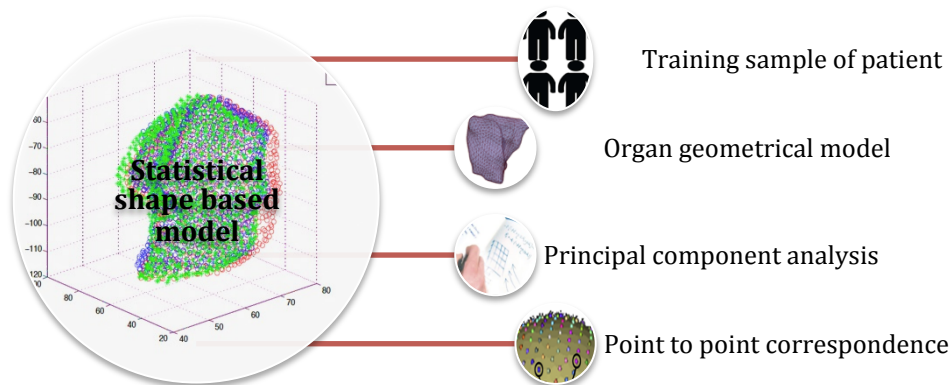


**Figure 19:** knowledge needed to implement statistical shape based model

In this work *FEM* biomechanical model has been implemented in order to represent parotid shrinkage in *H&N* patients treated with Tomotherapy. Also a statistical deformable model has been initially tested.

Starting from daily *CT* image data acquisition, the basic steps necessary to implement *FEM* biomechanical model and statistical deformable model of parotid glands morphing are:

1. Patients *CT* data acquisition
2. Images import into the TPS RayStation®
3. Parotid automatic re-contouring process automated via a Python scripting procedure
4. Import of the DICOM data and contours obtained in 3. into 3D Slicer®
5. Conversion of contours into 3D surface mesh representing parotid glands anatomy
6. Export of the created surface meshes
7. FEM biomechanical model implementation by using the FEM software COMSOL®
8. Statistical shape model implementation by using an home-made Matlab® script

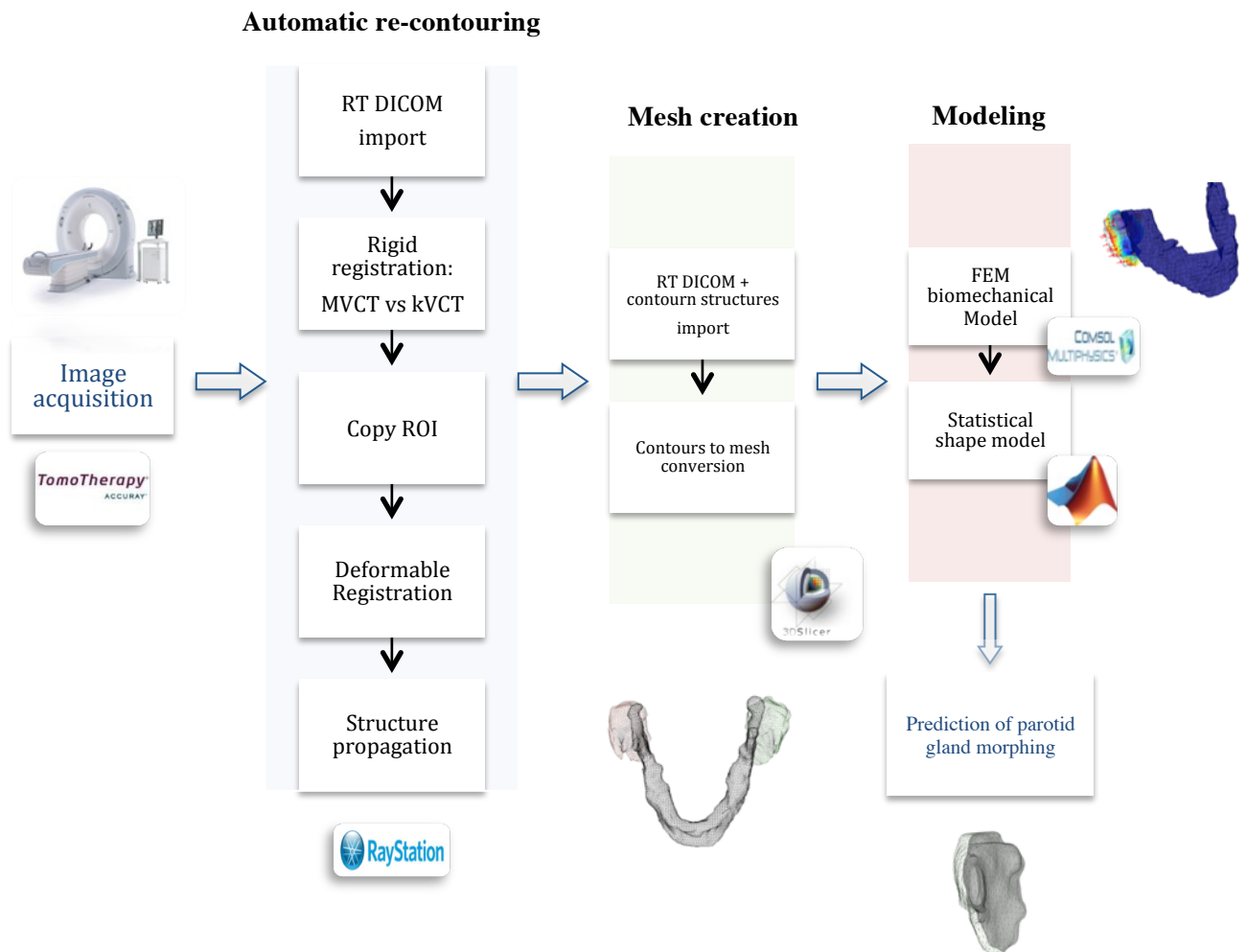


**Figure 20:** *FEM* biomechanical and statistical shape model implementation workflow

## 2. IMAGE BASED ORGAN MESH CREATION

### 2.1 SURFACE MESH CREATION WORKFLOW

Anatomical dimensions and geometry of parotid glands greatly differ from patient to patient due to various factors such as patient age, body size and weight and due to the presence of pathologies. Scanning procedures like Computed tomography are capable to get patient specific organ details including dimensions. Constructing a 3D model of an organ of interest from *CT* images leads to:

- Better visualization of the organ and its pathologies
- Benefit of the patient specific radiation therapy planning and simulation

In radiation therapy treatments, usually a set of 2D images with contours made by radiation oncologist are used to define organ shape. In this way a coarser representation of the organ is obtained. To have a better perspective of the distortions that occur in parotid glands we decide to represent structures in 3D using a mesh-based approach. The mesh-data structure is one of the most used techniques for rendering 3D objects. A mesh  $M$  is defined as a collection of points in  $\mathbf{R}^3$  (vertices), edges (a connection between two vertices) and faces (a closed set of edges) that define the shape of a polyhedral object. The faces could form polygons of any type but triangular polygons are commonly used since this simplifies rendering.

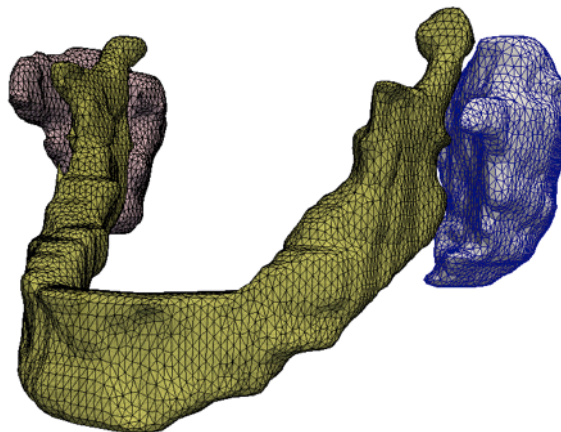


**Figure 21:** Examples of triangular meshes of parotid glands and mandible created from *CT* images by using the proposed method.



A triangular mesh  $M$  consist of geometric components that can be represented by a graph data structure with a set of vertices:

$$V = \{v_1, \dots, v_n\} \quad (Eq.2)$$

and a set of triangular faces connecting them:

$$F = \{f_1, \dots, f_F\} \quad f_i \in V \times V \times V \quad (Eq.3)$$

The geometric embedding of a triangle mesh into  $\mathbb{R}^3$  is specified by associating a 3D position  $p_i$  to each vertex  $v_i \in V$ :

$$P = \{p_1, \dots, p_n\}, p_i = \mathbf{p}(v_i) = \begin{pmatrix} x(v_i) \\ y(v_i) \\ z(v_i) \end{pmatrix} \in \mathbb{R}^3 \quad (Eq.4)$$

such that each face  $f \in F$  actually corresponds to triangle in 3D-space specified by its three vertex positions. Notice that even if the geometric embedding is defined by assigning 3D position to the discrete vertices, the resulting polygonal surface is still a continuous surface consisting of triangular pieces defining a segment of a piecewise linear surface representation via its barycentric parametrization of the corner points; every point  $p$  in the triangle  $[a, b, c]$  can be written as:

$$\mathbf{p} = \alpha \mathbf{a} + \beta \mathbf{b} + \gamma \mathbf{c} \quad \text{with } \alpha + \beta + \gamma = 1 \quad \alpha, \beta, \gamma \geq 0 \quad (Eq.5)$$

If a sufficiently smooth surface is approximated by such a piecewise linear functions the approximating error is of the order of  $O(h^2)$  with  $h$  denoting the maximum edge lengths. Due to this quadratic approximation power, the error is reduced by a factor of about  $\frac{1}{4}$  when halving the edge lengths as this refinement splits each triangle from  $F$  to  $4F$ . Hence the approximation error of a triangular mesh is inversely proportional to its number of faces, a sufficient approximation is possible with a moderate mesh complexity [18].

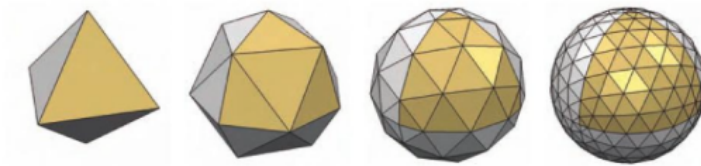


**Figure 22:** In triangular mesh creation process increasing the number of faces by a factor of 4 reduces the surface approximation error by a factor of  $\frac{1}{4}$

In general the process of automatic structure of interest mesh creation from 3D image data is known as image-based isosurface extraction and it involves two steps:

- 3D image data processing (segmentation or contouring of structures of interest)
- Surface mesh generation from segmented 3D data

The methodology implemented in this work to reconstruct organ of interest 3D meshes from daily *CT* image sequences of *H&N* patients undergoing tomotherapy treatment, is reported in the workflow in *figure 23*. It starts with the acquisition of *kVCT* image and daily *MVCT* images for each patient. Organ contours have been manually defined by radiation oncologist on *kVCT* and have to be automatically re-contoured on daily *MVCT*.

This goal has been reached within the *TPS RayStation® (v5.01 Raysearchlab, Stoklom, Sweden)* environment , by using both rigid and deformable image registration. Output contours obtained from automatic re-contouring process are then converted into triangular surface meshes by using the open source software *3D Slicer®*. Each step of the mesh creation process will be briefly described in the following sections.

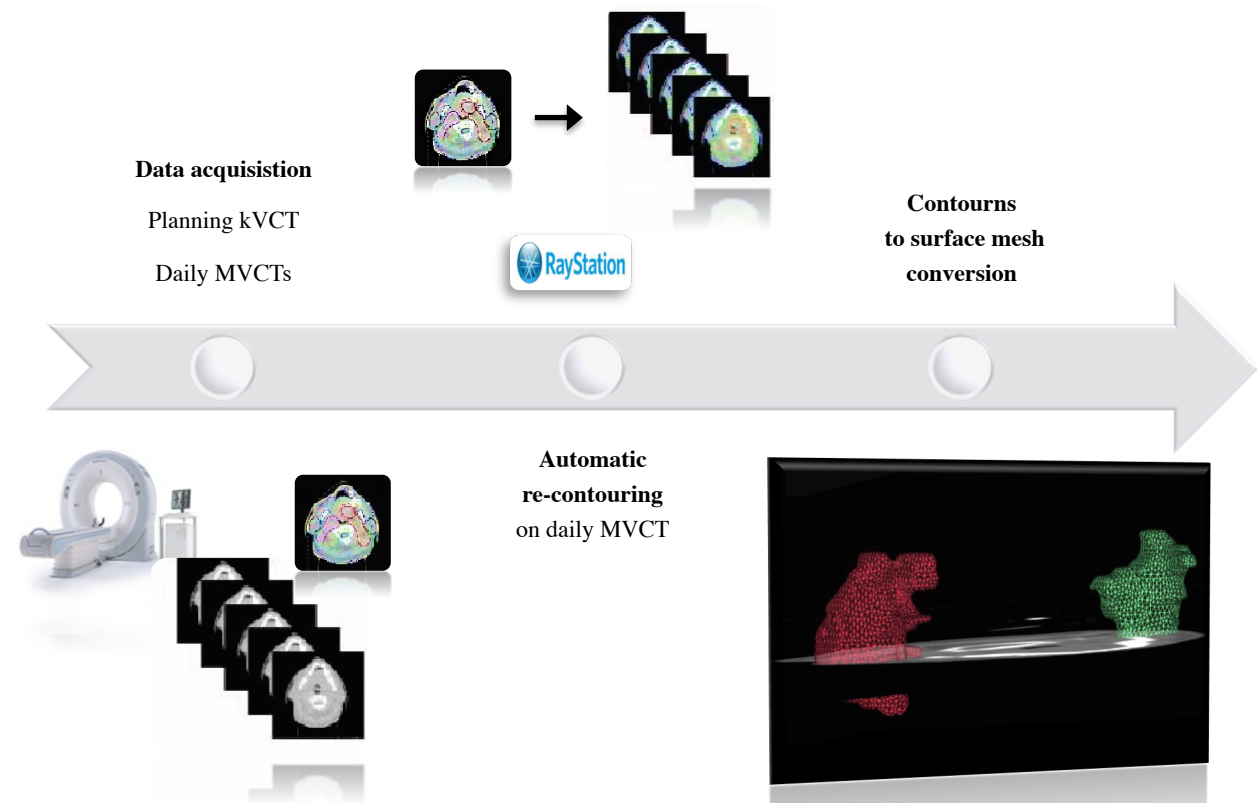


**Figure 23:** Workflow of the procedure implemented to create parotid surface mesh from CT images

## 2.2 DATA ACQUISITION

The data acquisition phase represents the starting point of our work. It involved 8 patients with H&N cancer treated with TomoTherapy® System. Daily CT images for all treatment duration have been acquired by using the scanning technology implemented in the Tomotherapy machine (fig.24). The planning kVCT image has been acquired for each patient by using the *Aquilion Large Bore CT System*. This latter image has been used by radiation oncologists to contour structures of interest such as mandible, spinal chord, *PTV*, *GTV*, *CTV*, body and parotid glands by using the contour tracing tool of the Pinnacle® treatment planning system used in the clinical practise at the “Azienda Ospedaliera Universitaria di Modena” Policlinico Medical Physics department.



**Figure 24:** Left: *Aquilion Large Bore CT system* Right: *TomoTherapy® Treatment system unit*

Patient	sex	age	Pathology	Dose Average Left PG (Gy)	Dose Average Right PG (Gy)
#1	M	72	H&N	32	23
#2	F	43	H&N	29	19
#3	F	48	H&N	25	29
#4	M	71	H&N	30	16
#5	M	56	H&N	23	21
#6	M	76	H&N	30	28
#7	M	46	H&N	25	24
#8	M	61	H&N	62	22

**Table 4:** summary of patients' data

## 2.2.1 TOMOTHERAPY

In order to monitor patient anatomy and position just before daily dose delivery, radiation treatment machines have to be equipped with imaging systems capable to provide on board patient image. The radiation therapy machine providing *OBI* (*on-board-imaging*) system used to treat patients analysed in this work is TomoTherapy<sup>®</sup> Treatment System.

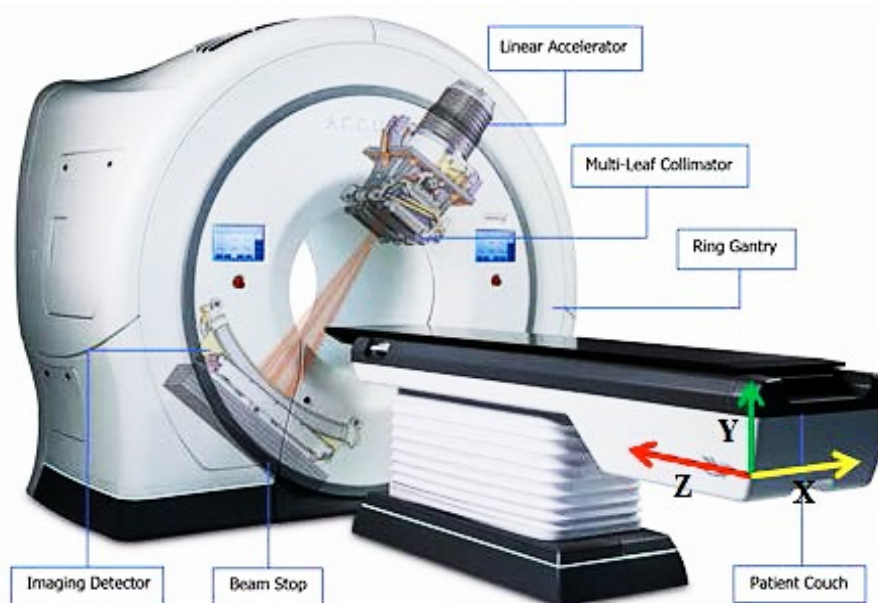


**Figure 25:** Scheme of the all-in one imaging and radiation treatment TomoTherapy unit

As can be seen in *fig.25*, the Tomotherapy machine is a combination of a helical *CT* scanner and a medical linear accelerator. Using the technology of diagnostic helical *CT* scanners the unit is capable of continuous rotation around the patient while the couch is moving into the gantry, providing smooth helical dose delivery. Mounted on the rotating gantry there is a compact (~40 cm long) linear accelerator generating a 6 MV photon beam. The beam from the accelerator is collimated by a multileaf collimator consisting of 64 leaves each of which project a shadow at the patient generating a total fan beam width of 40 cm. The *CT imaging detection system* consists of xenon detectors and it can be used for patient set-up verification and repositioning, verification of leaf positions during treatment and reconstruction of the actual dose delivered to the patient. To improve image quality and reduce the dose to the patient, when used for imaging purposes, the linear accelerator is slightly detuned leading to maximum electron energy at the target of 3.5 MeV rather than 6 MeV. The dose delivered to the patient per *MVCT* image acquisition is 0.5-3 cGy depending on resolution and body thickness.

### 2.2.2 IMAGE DATA SET: kVCT vs MVCT

The 3D image data set acquired for each patient, as described in the previous sections, is made up of:

- **1 planning kVCT** : the diagnostic image set acquired by using nominal photon beam energies of 120 kV and used by radiation oncologist to manually trace structures of interest contours.
- **30 daily MVCT**: daily *CT* images acquired from the scanning technology implemented in the treatment delivery machine by using the photon beam produced for treatment delivery whose energy has been detuned from 6 MV to 3.5 MV.

As we can see from *fig. 26* the *MVCT* scans will generally be inferior in quality respect to *kVCT* images (higher noise level and lower soft-tissue contrast with respect to *kVCT*), even though they still be able to verify the patient's position and anatomy prior to treatment, and provide information for dose reconstruction. It would be beneficial to have *kVCT* scanning capability built into the radiotherapy machine. However, because of the additional cost and complexity of incorporating this technology, Tomotherapy prototype will offer only Megavoltage *CT* scanning (recently development orient the technology to have *CT* integrated into the ring and will be available *MVCT* and cone beam *CT*).

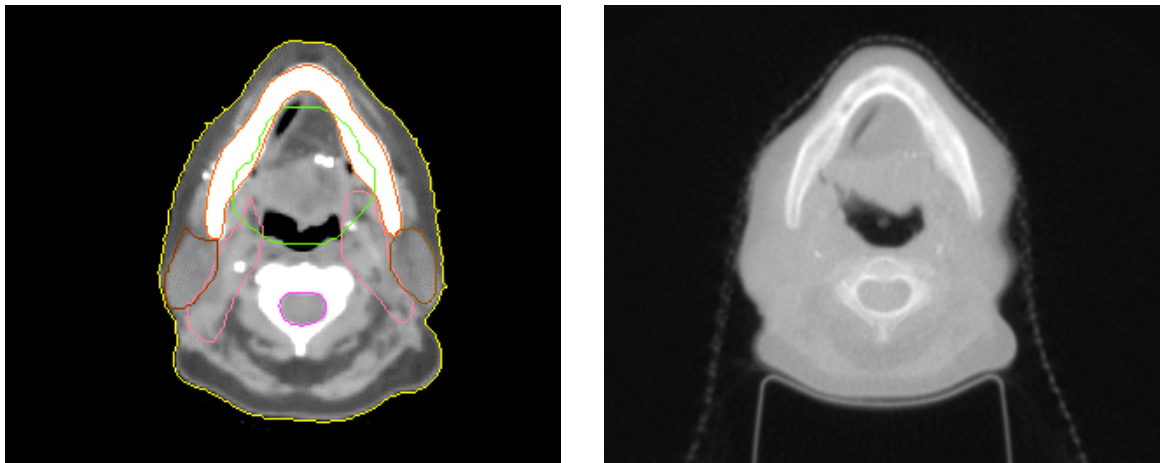


**Figure 26:** Left: An example of H&N patient *kVCT* with structures of interest contours traced by radiation oncologist. Right: *MVCT* of the same H&N patient acquired during the treatment delivery phase.

kVCT				MVCT			
NUMBER OF SLICES	DIMENSION X,Y (N° PIXELS)	DIMENSION X,Y,Z (CM)	IMAGE RESOLUTION: VOXEL SIZE (CM)	NUMBER OF SLICES	DIMENSION X,Y (N° PIXELS)	DIMENSION X,Y,Z (CM)	IMAGE RESOLUTION : VOXEL SIZE(CM)
180	512x512	53x53x54	0.103x0.103x0.3	30	512x512	38.9x38.9x12	0.076x0.076x0.4

**Table 5:** MVCT and KVCT image set dimensions where  $z$  coordinate refers to CT slices distance

The reason of the worst image quality of MVCT images realises on the fact that the ability to resolve soft-tissue contrast differences is fundamentally limited by the number of photons used to create the image. The kV and MV photons have similar mass energy-absorption coefficients, meaning that sending the same amount of photon with MV and kV energy a comparable *fractions* of each photon's energy are deposited in the patient. However the use of MV photons results in a greater absolute dose deposition per photon. In order to maintain comparable doses for MV and kV tomography, the number of MV photons must be significantly reduced. Unfortunately, this reduction decreases the signal-to-noise ratio (SNR) and thus impairs soft tissue contrast detectability [19].

	Mass energy-absorption coefficient, $\mu_{en}$ ( $\text{cm}^2 \text{g}^{-1}$ )	Mass attenuation coefficient $\mu/\rho$ ( $\text{cm}^2 \text{g}^{-1}$ )
60 keV photons	0.032	0.205
1.33 MeV photons	0.029	0.062

**Table 6:** Comparison of mass energy-absorption coefficients, and mass attenuation coefficient for kV and MV photons in water (Attix, 1986)

Furthermore since the attenuation coefficients of kV photons are higher than those of MV photons in soft tissue, the per cent density contrasts will be easier to detect at kV energies.

One mitigating factor for MV tomography is that the MV photons are more penetrating. Thus, a greater fraction of incident MV photons will travel through the patient and reach the detector. This effect provides some compensation for the reduced number of incident photons, especially for larger patients.

Due to the fact that MVCT will be used in the automatic re-contouring process it could be useful to consider the impact of the worst quality of MVCT compared to kVCT in organ surface

reconstruction phase. Results of preliminary investigations about volume differences for the same structure not attributable to anatomical changes but due to the different quality of kVCT and MVCT images are reported in *fig.27*. The *%volume* difference has been obtained comparing surface re-constructed from kVCT images contours and surface obtained from re-contouring procedure applied on first day of treatment MVCT; infact it is reasonable to consider that between kVCT image set acquisition time and start of treatment no considerable anatomical changes occurred in *H&N* structures, so volume differences for the same structure are only attributable to the different quality of kVCT and MVCT images. It emerges that for *H&N* organs belonging to volume classes grater than 100 *cc* values, *%volume* error can be considered equal to 1%value. Structures belonging to the volume class (0-100 *cc*), such as parotids involved in our study (mean PGs volume at start of treatment = 23.5 *cc* [*max* 32.5 *cc* – *min* 10.8 *cc* ] ), are affected by an average of 4% *volume* error .

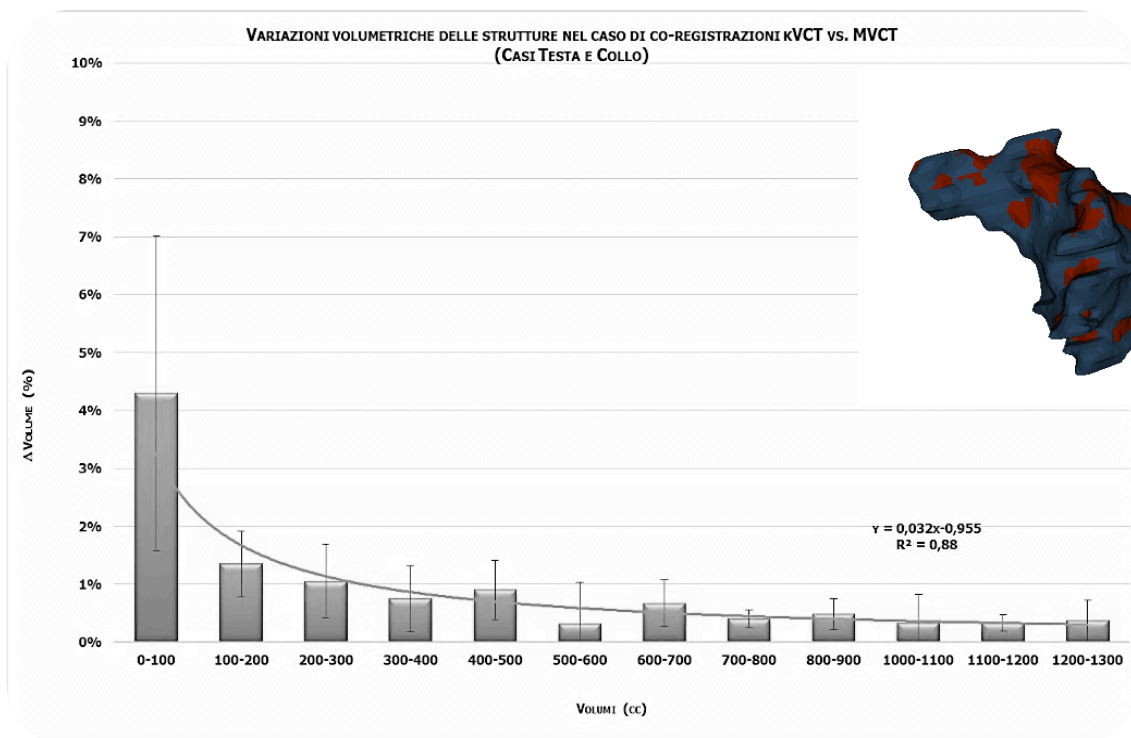


**Figure 27** : *%volume* differences for *H&N* structures belonging to different volume classes not attributable to anatomical changes but due to the different quality of kVCT and MVCT. An example of the overlap between parotid surface obtained using kVCT image contours (blue) and re-contoured MVCT at start of treatment is displayed on the top (red)<sup>11</sup>

<sup>11</sup> data taken from [11]

## 2.3 AUTOMATIC RE-CONTOURING

Contours<sup>12</sup> of parotid glands and other structures of interest have been traced by radiation oncologist only on the kVCT image set. In order to create a collection of mesh and to follow PGs shape deformation process for the whole treatment duration, contouring of PGs on daily *MVCT* is necessary. Automatic contours propagation on daily *MVCT* is of importance for an efficient workflow, avoiding tedious manual contouring procedure. Automatic re-contouring of parotid glands on daily *MVCT* has been performed by using the commercial treatment planning system RayStation® and the automated Python scripting procedure implemented in a previous work made at the “*Azienda Ospedaliero Universitaria di Modena*” Policlinico [16]. The automatic re-contouring process involves rigid and deformable registration of kVCT with daily *MVCT*.

In general, it is difficult to quantify the accuracy of an automatic re-contouring approach, due to the fact that even manual contouring can be affected by intrinsic uncertainty depending on operator contouring variability. On going work focus on asking a radiation oncologist to score the automatically re-contoured structures in order to quantify the accuracy of our procedure.

*C. Lee et al.* at *Department of Radiation Oncology M. D. Anderson, Orlando (USA)* [25], found that contours generated automatically, fall within the uncertainty range of a manual contouring procedure. Furthermore if we consider that an automatic contouring procedure is undoubtedly faster and require limited user operations, we can conclude that it can be used to efficiently estimate structures of interest temporal and geometric variation with respect to treatment start.

### 2.3.1 IMAGE REGISTRATION

Image registration, in medical field, is the process of overlaying two or more images of the same patient (or district) taken at different times and/or by different imaging modalities. To solve the registration problem means finding the geometrical transformation  $T$  that aligns points in one view of an object with corresponding points in another view of that object or another object.

The two sets to be registered are the inputs of image registration; the output is a map, derived from a geometrical transformation, from points in one view to points in the second one.

---

<sup>12</sup> *Contour tracing is a technique applied to digital images in order to extract connected pixels defining object contourn.*



One of the images is referred to as the *reference* or *source* (*fixed image*  $\Omega_f$ ) and the others are respectively referred to as the *target* or *subject* images (*moving images*  $\Omega_m$ ):

$$T(x, y, z): (x, y, z) \in \Omega_f \rightarrow (X, Y, Z) \in \Omega_m \quad (\text{Eq.6})$$

The aim of an image registration algorithm is to estimate the optimal geometrical transformation  $T$  optimizing an objective function that express similarity between target and reference images. Image registration algorithms can be classified according to the transformation models they use to relate the target image space to the reference image space in two broad categories:

- **Rigid registration:** the transformation models used are linear transformations, which include rotation, scaling, translation, and other affine transforms. Linear transformations are global in nature, thus, they cannot model local geometric differences between images.
- **Deformable registration:** non linear transformations models allow elastic or nonrigid transformations. These transformations are capable of locally warping the target image to align with the reference image.

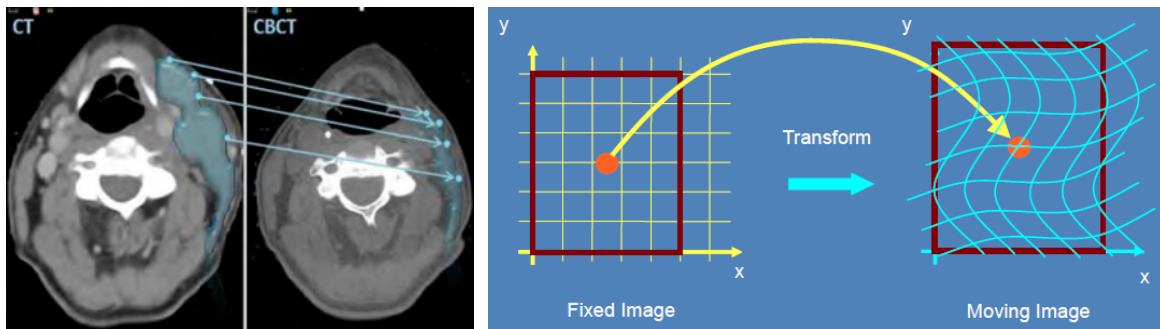


*Figure 28: Example of rigid (left) and deformable (right) registrations*

Image registration algorithms can be classified also into:

- **Intensity-based:** Intensity-based methods compare intensity patterns in images using image similarity measures including cross correlation, mutual information, sum of squared intensity differences and ratio image uniformity.
- **Feature-based:** feature-based methods find correspondence between image features such as points, lines, and contours. Knowing the correspondence between a numbers of points in images, a geometrical transformation is then determined to map the target image to the reference image.

### 2.3.1.1 RIGID REGISTRATION: MUTUAL INFORMATION ALGORITHM

The RayStation® rigid registration algorithm used in this work is *intensity-based* (based on the assumption that regions of similar tissue and hence similar grey value in one image would correspond to regions in the other image that also consist of similar grey values) and uses *mutual information*. The objective function of mutual information image registration algorithm is a similarity measure based on Shannon entropy  $H$ :

$$H = -\sum p_i \log(p_i) \quad (Eq.7)$$

Where  $p_i$  is the probability of signal intensity. A probability distribution of grey values can be estimated by counting the number of times each grey value occurs in the image and dividing those numbers by the total number of occurrences. An image consisting of almost a single intensity will have a low entropy value; it contains very little information. A high entropy value will be yielded by an image with more quantities of many different intensities, which is an image containing a lot of information. In this manner, the Shannon entropy is also a measure of dispersion of a probability distribution. It is possible to construct a feature space, which is a two-dimensional plot showing the combinations of grey values in each of the two images for all corresponding points. The feature space (or joint histogram) changes as the alignment of the images changes. When the images are correctly registered, corresponding anatomical structures overlap and the joint histogram will show certain clusters for the grey values of those structures. For two images A and B, mutual information  $I$  can be defined as:

$$I(A, B) = H(A) + H(B) - H(A, B) \quad (Eq.8)$$

Where  $H(B)$  is the Shannon entropy of image B,  $H(A)$  is the Shannon entropy of image A,  $H(A, B)$  denotes the joint entropy.

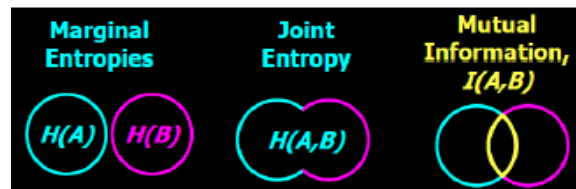


**Figure 29:** Venn diagram representation of marginal entropies, joint entropy and mutual information concept

Due to the fact that  $A$  and  $B$  can be interchanged,  $I(A, B)$  is named mutual information. Registration is assumed to correspond to maximizing mutual information: the images have to be aligned in such a manner that the amount of information they contain about each other is maximal which means minimizing joint entropy.

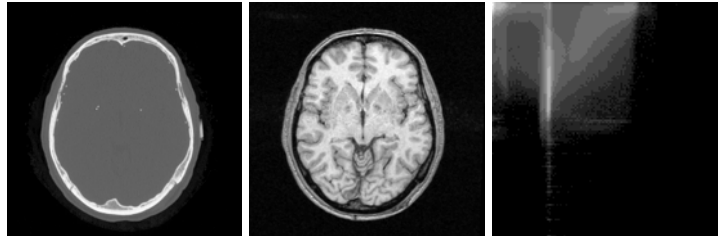


**Figure 30(a):** Example of a feature space for a CT image (left) and an MR image (middle). Along the axes of the feature space on the right, the grey values of the two images are plotted: from left to right for CT and from top to bottom for MR. The feature space is constructed by counting the number of times a combination of grey values occurs. For each pair of corresponding points  $(x, y)$ , with  $x$  a point in the CT image and  $y$  a point in the MR image, the entry  $(ICT(x), IMR(y))$  in the feature space on the right is increased. A distinguishable cluster in the feature space is the stretched vertical cluster, which is the rather homogeneous area of brain in the CT image corresponding to a range of grey values for the MR image. [20]

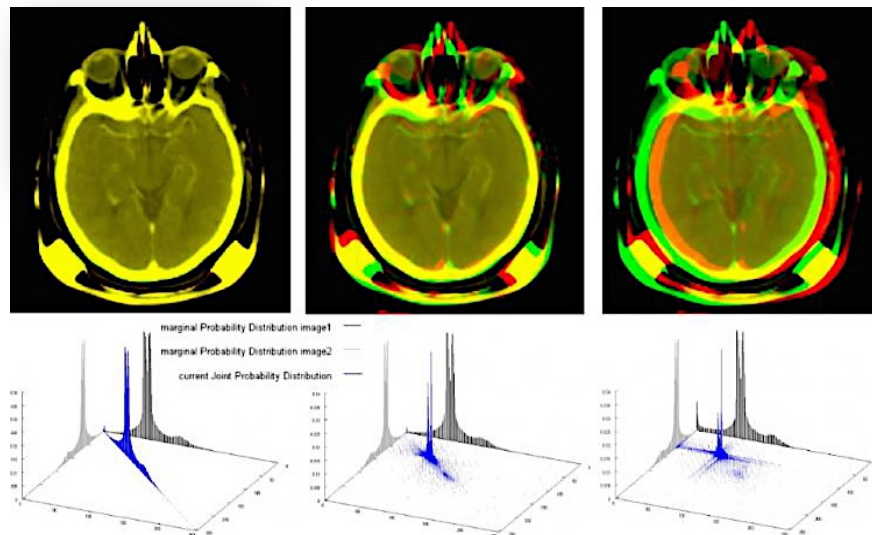


**Figure 30(b):** From left to right: MRI-CT brain registration of good, medium and poor quality. More spread is the joint histogram worse is the registration

We report an example of the RayStation rigid registration output, obtained using grey level based mutual information option and setting KVCT image as target image and daily MVCT as source image.

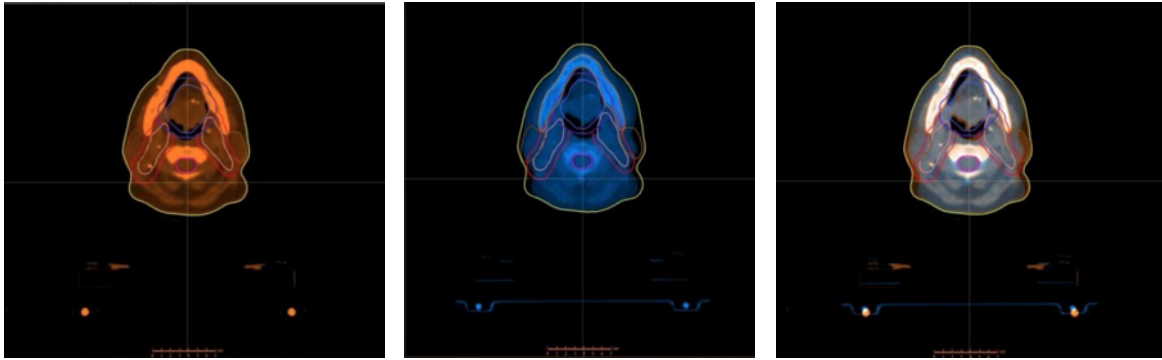


**Figure 31:** Example of rigid registration result performed with RayStation intensity-based image registration algorithm between kVCT (orange) and daily MVCT (blue).

### 2.3.1.2 DEFORMABLE REGISTRATION: THE ANACONDA ALGORITHM

Through deformable image registration algorithm (*DIR*), we can propagate contours from one image set to another. To compute a *DIR* we need a measure of similarity, acting as a driving force for the registration computation. The similarity measure can be based on geometrical structures or image intensities.

For the *geometric approach*, we need landmarks (surfaces, curves, points) marking out relevant structures defined in the two image sets. By sophisticated selection of landmarks, which can be tedious and time consuming, we can obtain a deformation vector field (defining voxel-voxel mapping between reference and target images) which is anatomically reasonably close to the landmarks without being dependent on the underlying image data. This makes it robust to noise or choice of image modality. However it has two drawbacks:

- We have no information of movements in regions where no landmarks have been selected
- No guarantee of a reasonable deformation vector field in such regions

For the *intensity-based approach*, intensities are matched voxel or patch-wise using some mathematical or statistical criterion. In this case, all voxels or at least patches of voxels take part in driving the *DIR* algorithm. On the other hand, it leads to:

- No guarantee that the deformation is anatomically reasonable
- More sensitiveness to unexpected contrast variations such as surgery implant and air cavities

The deformable registration algorithm implemented in the commercial treatment planning RayStation platform and used in this work is ANACONDA (ANatomically CONstrained Deformation Algorithm) [21]. ANACONDA combines image information (i.e., intensities) with anatomical information as provided by contoured image sets. Using a hybrid solution, either geometric or intensity based, ANACONDA can have the benefit of both while avoiding their previously noted drawbacks.

Denoted the reference image  $R$  and the target image  $T$ , to reduce the influence of image artefacts, the images  $R$  and  $T$  are filtered using a Gaussian filter with  $\sigma = 1/3 \text{ voxel}$  by the ANACONDA algorithm.

Let the deformation grid be a set of grid points arranged in a regular manner on a lattice dividing image-space into box shaped elements (voxels). The *DIR* algorithm ANACONDA computes a vector field defined on the grid. This vector field is called a deformation vector field. The deformation vector at grid point  $x_i \in \mathbb{R}^3$  is denoted  $v_i \in \mathbb{R}^3$ . The deformable registration problem in ANACONDA algorithm is formulated as a nonlinear optimization problem with objective function  $f: \mathbb{R}^n \rightarrow \mathbb{R}$  :

$$f(v) = \alpha C(v) + (\beta H(v) + \gamma S(v)) + \delta D(v) \quad (\text{Eq. 9})$$

where

1. The image similarity is measured by the correlation coefficient  $C(v)$  .
2.  $\gamma S(v)$  is a shape based regularization term, which works to keep the deformation anatomically reasonable when regions of interest are present in the reference image.<sup>13</sup>
3.  $\beta H(v)$  is a grid regularization term, which aims at keeping the deformed image grid smooth and invertible .
4.  $\delta D(v)$  is a penalty term (which is added to the optimization problem when controlling ROI structures are used), aimed at deforming the selected structure in the reference image to the corresponding structure in the target image.

---

<sup>13</sup> Assume there is a triangular mesh representing an anatomical region defined in  $\mathbb{R}^3$ . We would like the deformation algorithm to deform the mesh in a reasonable manner. For example, although smooth and invertible, a deformation vector field could potentially deform structures in a non intuitive way, if the driving similarity measure is not reliable. The aim of the shape based regularization term is to add robustness to protect against erroneous image data.

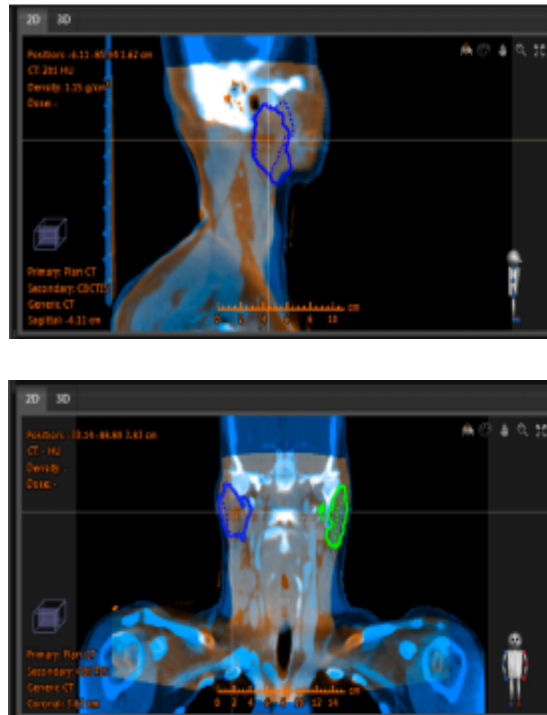


**Figure 32:** Head and Neck with Plan-CT and 15- day CT are shown rigidly fused. Parotid contours at planning time have been deformed to match 15-day anatomy by using deformable ANACONDA algorithm. ROIs Parotid (left) (green) and Parotid (right) (blue) shown as solid lines on PlanCT and dashed lines on 15 day CT.

### 2.3.2 AUTOMATIC RE-CONTOURING IMPLEMENTATION

The automatic re-contouring process used in this work and performed by using RayStation<sup>®</sup> platform starts with a mutual information rigid image registration between *MVCT* (reference image) and *kVCT* (target image). After rigid registration is performed, original contours ROI defined on *kVCT* are copied over daily *MVCT*. Then elastic registration is performed between daily *MVCT* and *KVCT*. Setting structures of interest as focus ROIs and body ROI as the external ROI defining the limit of the deformable grid, the hybrid deformable registration algorithm ANACONDA is applied: it creates deformed vector fields (*DVF*) that define a voxel-to-voxel mapping between the reference and the target image (*fig.34*). Subsequently, the *DVF* deforms the copied ROIs contours and new ROIs contours are automatically traced on the daily *MVCT* defined as reference image. The adaptive process available allows also to deform the planned dose grid in such a way as to adapt the treatment plan to the morphological changes of the patient occurred during *RT* sessions (*dose warping*, *dose accumulation and summation*, *dose super-imposed steps* of the workflow in *fig.33*).

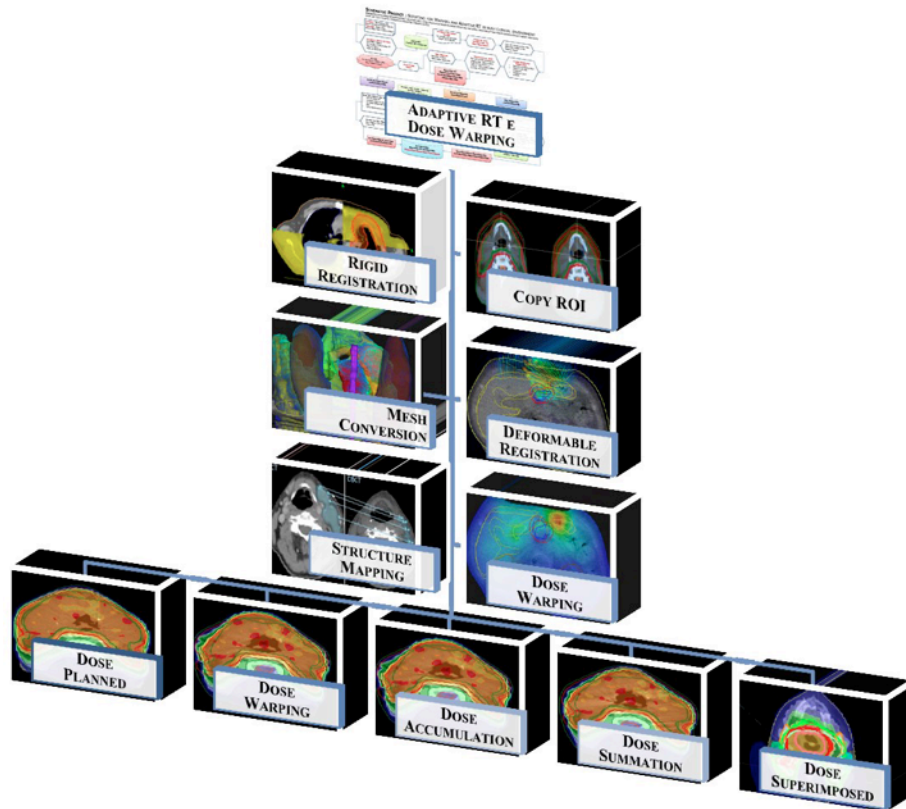


**Figure 33:** Step by step of the re-contouring process automated via Python scripting used in this work and proposed by [16]. We stop at structure propagation step to re-contour parotid glands on daily MVCT even if the adaptive process allows also to deform dose distribution as shown in the last steps of the workflow.

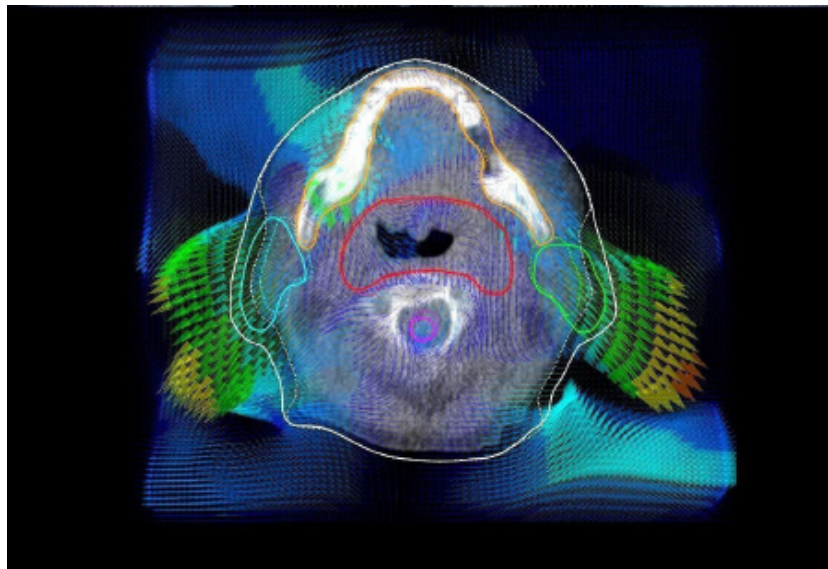


**Figure 34:** Deformed mesh grid and deformation vector field visualization. Parotid gland at planning time are represented as continuous green and light blue lines while their re-contours on the current daily patient anatomy are represented by dashed lines

## 2.4 CONTOURS TO MESH CONVERSION: MARCHING CUBE ALGORITHM

Software packages that can produce high quality meshes are usually commercial. In this paragraph we describe the implementation of a surface mesh generation process within the open source software package for visualization and medical image computing 3D Slicer<sup>14</sup> [22]. Slicer uniquely integrates several facets of image-guided medicine into a single environment. It provides capabilities for generation of 3D surface models (for viewing the segmented structures), 3D visualization, and quantitative analysis (measuring distances, angles, surface areas, and volumes) of various medical scans.

Slicer is a modular environment supporting three types of modules:

- **Command Line Interface (CLI):** standalone executable with a limited input/output arguments complexity.
- **Loadable modules:** plugins that are built against Slicer, loadable by using the *extension wizard*.
- **Scripted modules:** Python scripts launched by using Slicer Python interactor window.

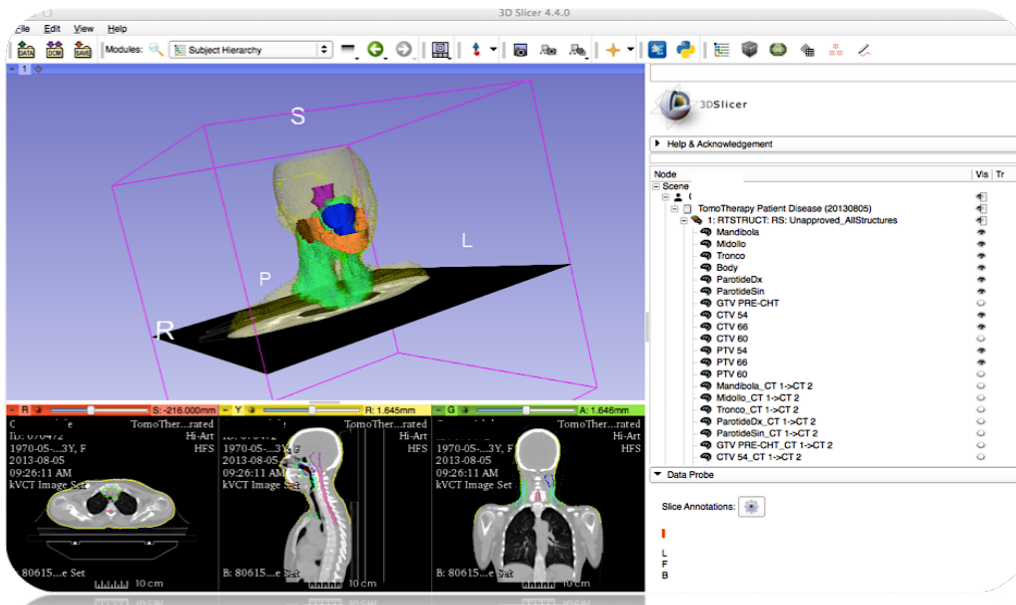


**Figure 35:** Layout of 3D Slicer environment with graphic window on the left and SubjectHierarchy on the right. In the graphic window we can see surface representation of structures of interest contoured on CT image set of an H&N patient.

<sup>14</sup> 3D Slicer is available for download at (<http://www.slicer.org>)



In order to create each patient's set of parotid meshes, a combination of the different modules type will be used. The surface mesh creation procedure implemented (*fig.36*) starts by using the *CLI DICOM* module to import each patient *CT* images and contours obtained from the previous step of automatic re-contouring. The Subject Hierarchy module manages all data that has been loaded from DICOM module. Contours module is then used to manage contours nodes in the hierarchy.

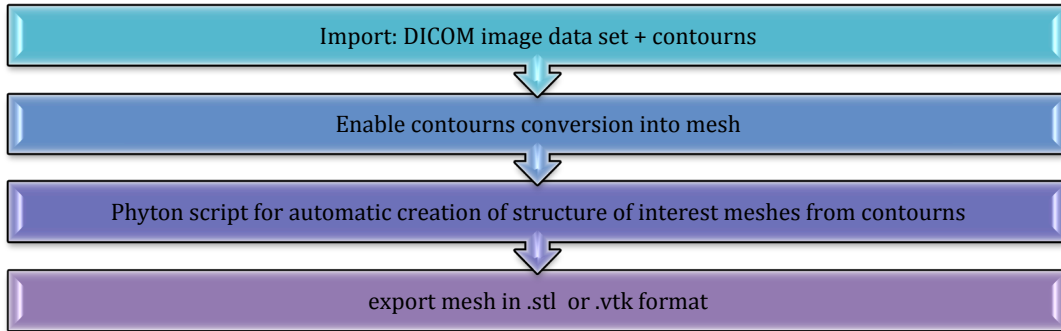


*Figure 36: Workflow of mesh creation from contours procedure implemented*

Each contours node can contain multiple data representations for the same structure, and the contour module supports conversion between these representations. The default ones are (*fig.37*) :

- **Planar contour:** stack of contours defined on diagnostic image set.
- **Label map:** 3D scalar volume with voxel numbered to indicate the type of tissue at that location.
- **Closed surface model or mesh:** collection of vertices, edges and faces that define the shape of the organ.
- **Ribbon model:** stack of ribbon obtained considering planar contours and the distance between two slices of the diagnostic image set.



*Figure 37: The default representations of a contour node in 3D Slicer: A) planar contours , B) closed surface model, C) binary label map , D) ribbon model*

There is currently no *CLI* solution to extract a model node from a contour node, but it can be done by using a Python script launched by the Slicer Python interactor (see Appendix 2), once contours to mesh conversion has been enabled. For models creation Slicer uses the *marching cubes algorithm* [23]; it produces triangles meshes of constant density from 3D medical image data. Marching cube uses a divide-and-conquer approach to locate the surface mesh in a logical cube created from eight pixels; four each from two adjacent slices (*fig.38*).

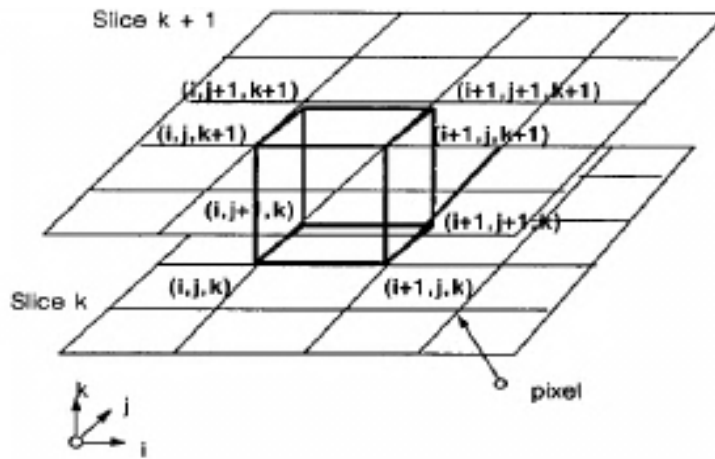


*Figure 38: Marching cube*

The algorithm determines how the surface intersects this cube, then moves (or march) to the next cube. To find the surface intersection in a cube, it assigns a one to a cube's vertex if the image data value at that vertex equals the value of the surface we are constructing. Cube vertices with values different from the surface value receive a zero. The mesh surface we create intersects those cube edges where one vertex is outside the surface (one) and the other is inside the surface (zero). With this assumption, the topology of the surface within a cube is determinate. Since there are eight vertices in each cube and two states, (one and zero), there are only  $2^8 = 256$  ways a surface can intersect the cube. By enumerating these 256 cases, it is possible to create a table to look up surface-edge intersections. Triangulating the 256 cases is possible but tedious and error-prone. Two different symmetries of the cube reduce the problem from 256 cases to 14 patterns (*fig.39(a)*). The simplest pattern, 0, occurs if all vertex values are above (or below) the selected contours value and produces no triangles. The next pattern, 1, occurs if the surface separates one vertex from the other seven, resulting in one triangle defined by the three edge intersections. Other patterns produce multiple triangles. Permutation of these 14 basic patterns using complementary and rotational symmetry produces the 256 cases.

An index for each case, based on the state of the vertex is stored. Using the vertex numbering in *figure 39(b)* the eight-bit index contains one bit for each vertex. This index serves as a pointer into an edge table that gives all edge intersections for a given cube configuration. Using the index to tell which edge the surface intersects, we can linear interpolate the surface intersection along the edge.

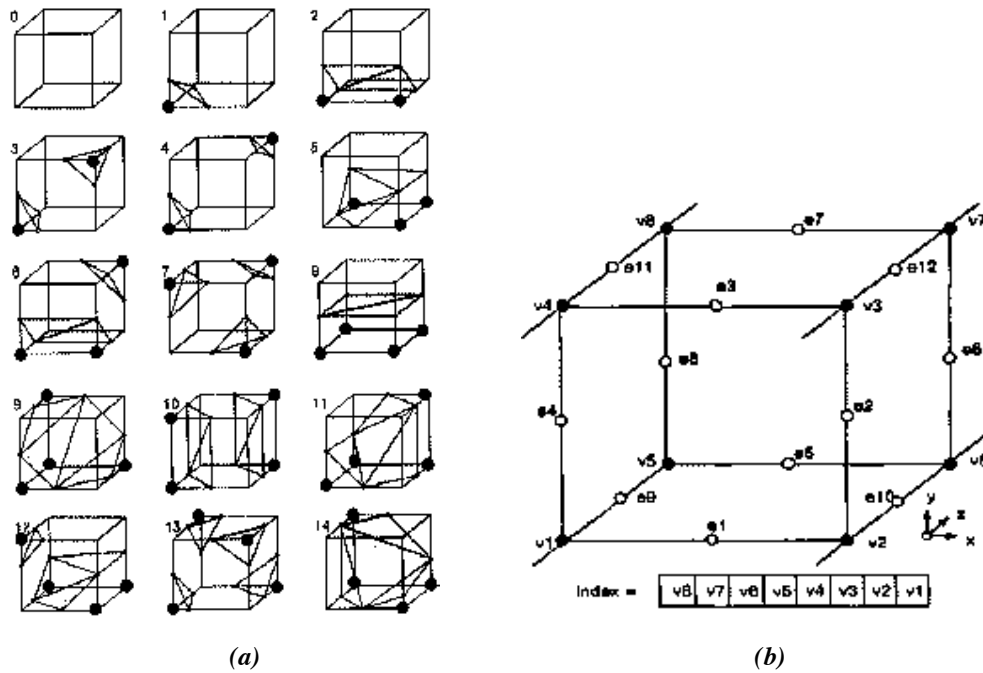


**Figure 39:** (a): Triangulated cube. (b): Cube Numbering

Fixed structure of interest name, the Python script lunched in the 3D Slicer environment (see Appendix 2) by using the marching cube algorithm outputs model's node obtained from the corresponding contours representation (*fig.40*). Once all meshes represented structure of interest have been created for each patient, some quantitative mesh-analysis can be done using 3D Slicer loadable modules such as *Mesh statistic*, *Model to Model distance*, *DICE computation*.

In the next section we will define quantitative index used in this work. Finally the obtained meshes can be exported in the .vtk or .stl<sup>15</sup> file format in order to be used in the implementation of the *FEM* biomechanical model.

<sup>15</sup> .Stl file format describes a solid whose surface was discretized in triangles in terms of coordinates X, Y and Z for each of the three vertices of each triangle, with a vector to describe the orientation of the normal to the surface. The .Stl file format can be viewed or corrected with open source tools such as MeshLab or Paraview and it is one of the major formats used in the field of 3D printing. Vtk file format describes a solid discretized in triangles in terms of mesh point coordinates allowing to assign them scalar or vector data type.

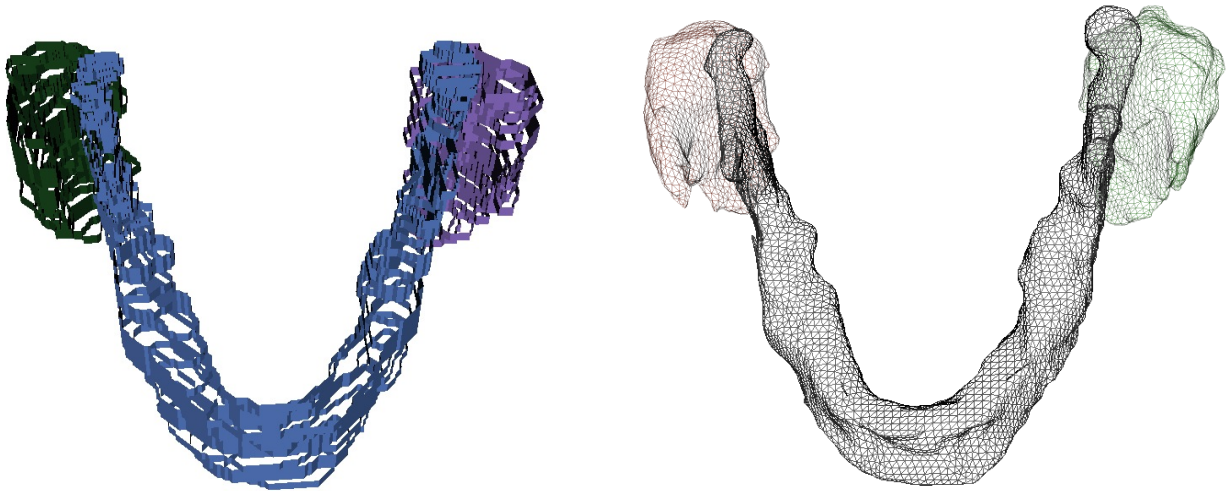


**Figure 40:** (left) Ribbon model representation of parotid glands and mandible contours obtained from the automated re-contouring procedure and their mesh representation (right) obtained with the procedure implemented in 3D Slicer.

## 2.5 MESH QUANTITATIVE ANALYSIS

Several quantitative indices of 3D mesh surfaces can be used in order to evaluate the differences between parotid real geometry and the predicted one obtained by the *FEM* biomechanical model. These can be also used to make some quantitative consideration about parotid shrinkage process. Mesh quantitative indices can be divided in two groups:

- Indices that give spatial and geometrical information of an *individual mesh*, such as volume and surface area.
- Indices that make a *comparison between two meshes*: volume difference, dice similarity coefficient (*DICE*), maximum distance between meshes (*DMax*) also named *Hausdorff distance*.

*DICE* index is a metric that express the overlap between two surfaces that ranges from 0 (no spatial overlap) to 1 (complete overlap) (fig.41). *Hausdorff distance* [24] represents the maximum distance between two surfaces and gives an idea of the worst local distance mismatch, which is 0 for a perfect match (fig.42).

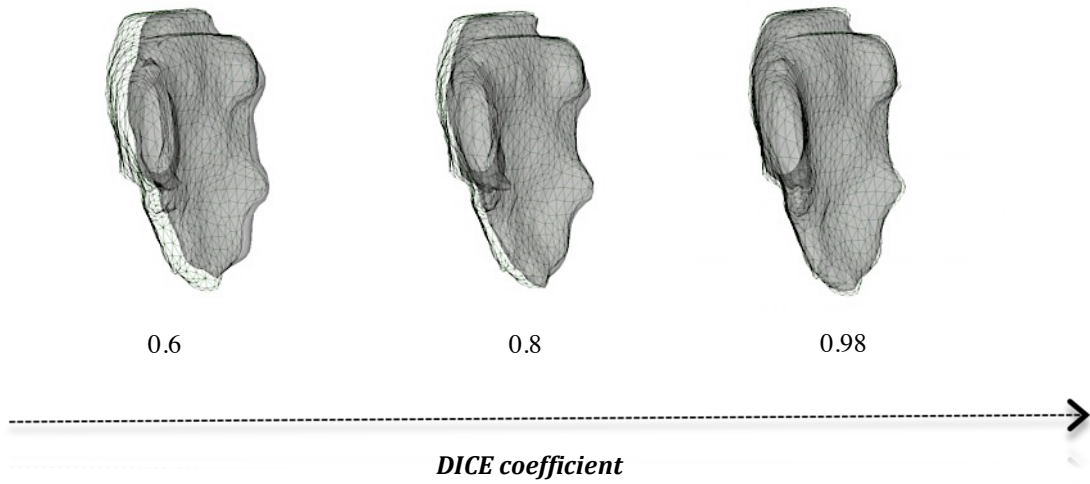


**Figure 41:** Example of DICE coefficient values corresponding to different amount of overlap between meshes of parotid glands.

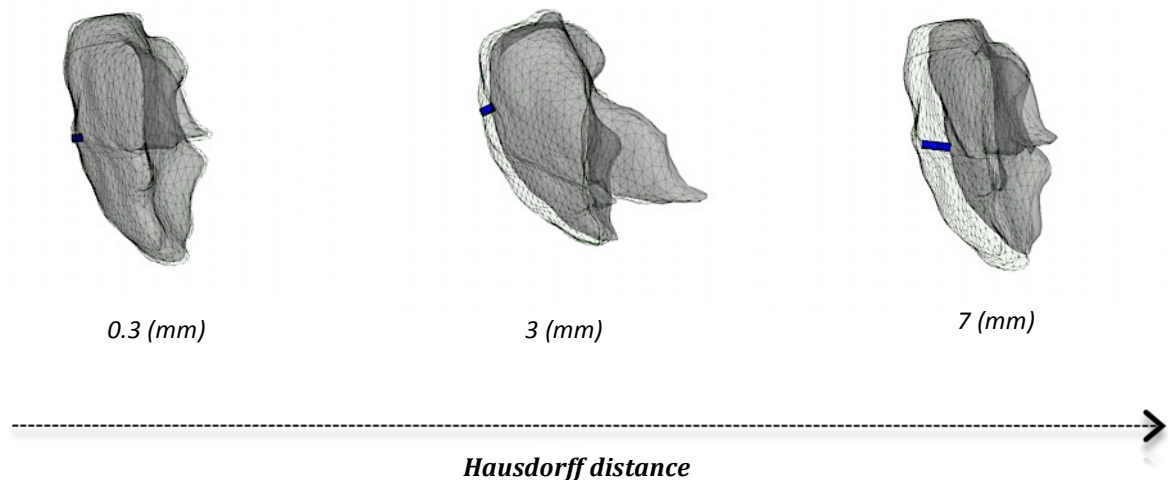


**Figure42:** Example of Hausdorff metric corresponding to different mismatch condition between parotid glands.

For *DICE* and *Hausdorff distance* calculations, sets of classes that enable computation of Boolean operations on meshes have to be used. Boolean operations over meshes can be computed using the signed distance field (distance from a point in one mesh to the nearest point on the surface defined by another mesh). The sign of the distance field corresponds to whether a point is inside (negative), outside (positive), or on (zero) the other mesh.

In this context, the Boolean operations of union, intersection and difference were defined as:

- **Union:** set of cells in each mesh such that the distance from each cell point to the other mesh is  $\geq 0$ .
- **Intersection:** set of cells in each mesh such that the distance from each cell point to the other mesh is  $\leq 0$ .
- **Difference:** set of cells of the mesh  $A (M_A)$  whose points are a non-negative distance from meshes  $B (M_B)$  combined with the cells of  $M_B$  whose points is a non positive distance from  $M_A$ .

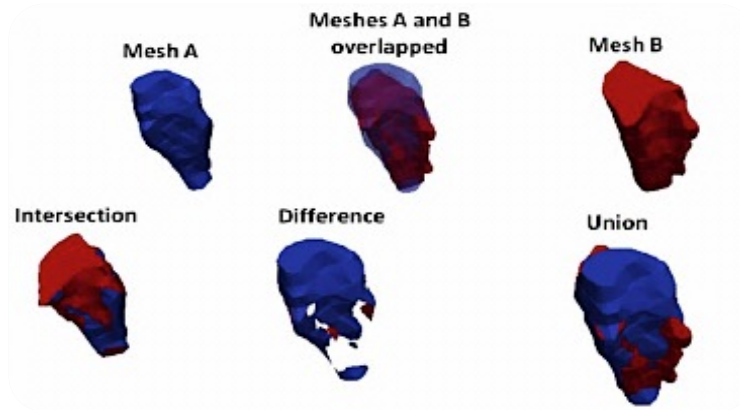


Figure 43: Boolean operations over meshes<sup>16</sup>

Taking these assumptions into account and given two meshes A and B, the *DICE* and *DMax* indices were calculated as:

$$DICE = 2 \frac{V_A \cap V_B}{V_A + V_B} \quad (Eq.10)$$

$$DMax = \max \left\{ \max_{p_A \in M_A} d(p_A, M_B) \mid \max_{p_B \in M_B} d(p_B, M_A) \right\} \quad (Eq.11)$$

where  $V_A$  and  $V_B$  are the set of voxels within A and B respectively,  $d(p_A, M_B)$  and  $d(p_B, M_A)$  indicate the shortest distance between an arbitrary point to A or B respectively. *DICE* index and *Hausdorff distance* can be calculated by using *3D Slicer CLI* modules.

<sup>16</sup> Image taken from Mejia-Rodriguez, AR et al, "Mesh-based approach for the 3D analysis of anatomical structures of interest in radiotherapy.", 2012 Annual International Conference of the IEEE Engineering in Medicine and Biology Society, San Diego, CA (USA), Aug. 28 2012-Sept. 1 2012

*Model to model distance* and *Mesh statistic* modules have been used to compute *Hausdorff distance* between two parotid meshes. The first module computes a signed distance map between two models *VTK file 1* and *VTK file 2*.

The output mesh (*VTK out*) has the same number of vertices as the first input model (*VTK file 1*). The distances are saved in the input model as a point data array under the name "*Distance*". *Model to model distance* module is based on *vtkDistancePolyDataFilter* [40] that computes the distance from a point of *VTK file 1* to the nearest point on *VTK file 2*. *VTK1* points interior to the *VTK2* geometry have a negative distance, points on the exterior have a positive distance, and points on the *VTK2* have a distance of zero. Then *Mesh statistic* module reads in the *VTK out* mesh and returns the maximum distance value stored in it.

*DiceComputation* module is able to calculate the *DICE* coefficient between multiple label map structures. For this reason, before running this *CLI* module it is necessary to convert models to label map by using the suitable *3D Slicer* module (*Model to label map*).

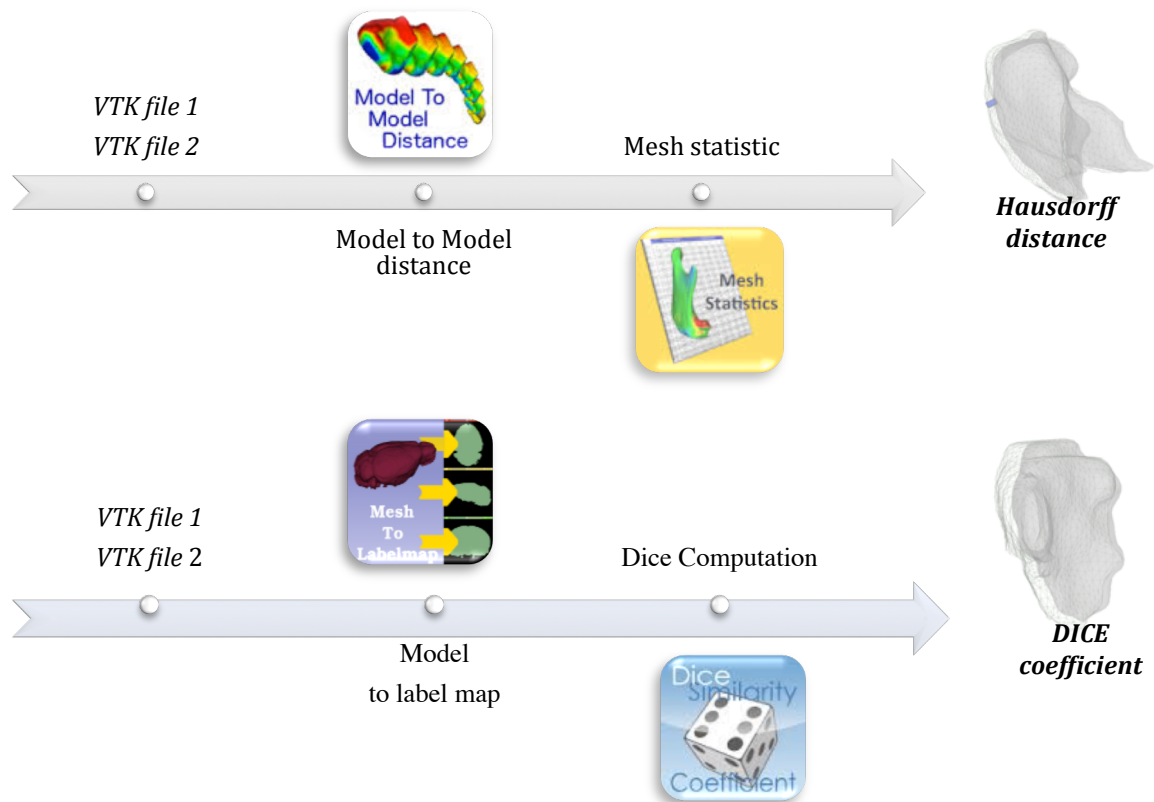


**Figure 44:** Schematic representation of the procedure implemented within 3D Slicer environment to perform mesh quantitative analysis.

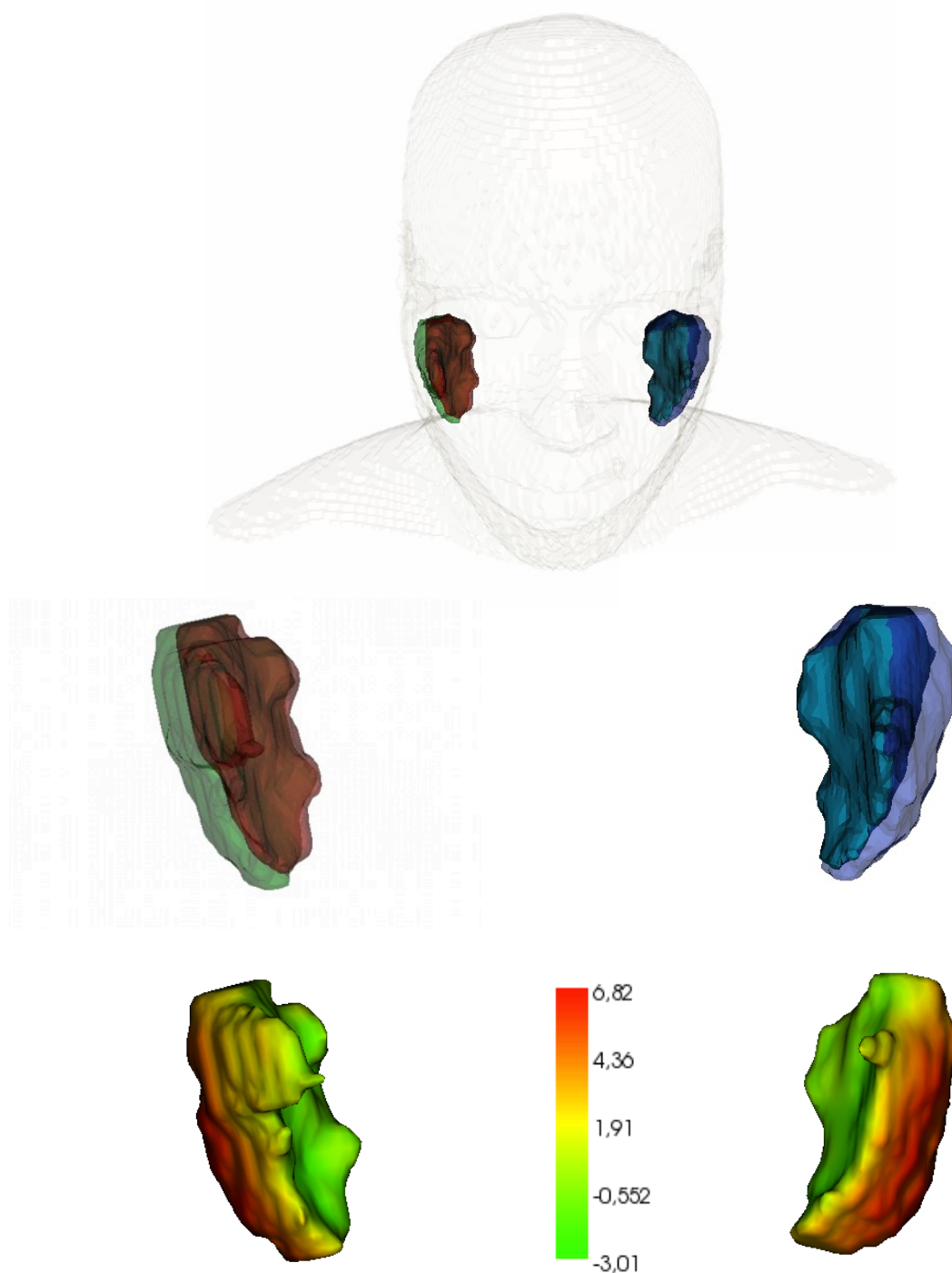


**Figure 45:** Visualization of PGs surface meshes at the first day of treatment (light green and blue) and at the end of the treatment duration overlaid (red and light blue full color surface) and the correspondent distance maps (VTK1 = PGs 1-st day of treatment, VTK2 = PGs 31-st day of treatment) obtained with model to model distance CLI module (distance values mm).



### 3. FEM BIOMECHANICAL MODEL OF PAROTID MORPHING

#### 3.1 FINITE ELEMENT MODELING OF PAROTID GLAND MORPHING

In this paragraph we will introduce a novel approach designed to handle the challenge of modeling parotid gland deformation in a realistic way by using knowledge about its elastic properties and the processes responsible of its deformation during *RT* treatment. The biomechanical model of parotid gland morphing proposed in this work has been implemented by using the finite element software COMSOL® multiphysics. The modeling construction phase has required a comprehensive knowledge of the following major fields of study:

- Parotid gland anatomy and radiosensitivity
- Continuum mechanics
- Soft tissue modelling
- The finite element method (*FEM*)

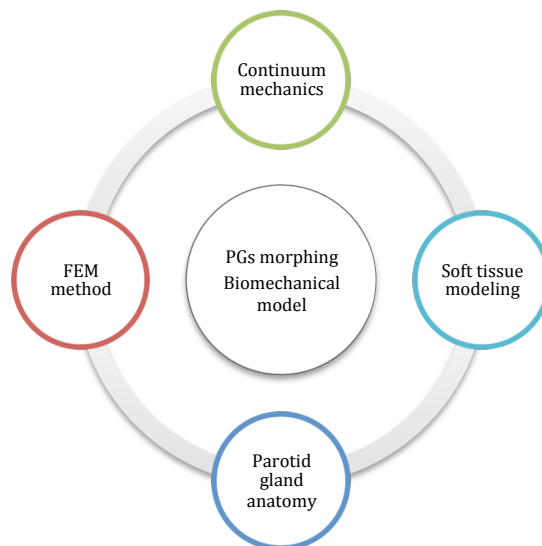


**Figure 46:** Different fields of study necessary to develop *FEM* biomechanical model of parotid morphing

Anatomy of parotid gland and its radiosensitivity has been discussed in 1.4. This paragraph is ordered in two major sections, which cover the basics of continuum mechanics, soft tissue modeling and *FEM* method and contains issues that have been relevant to the numerical modeling

of PGs morphing. At the end we describe steps necessary in order to create parotid gland morphing *FEM* model by using COMSOL® multiphysics software.

The real observed phenomenon of parotid morphing is very complex involving change in shape and position and interaction between parotid gland and all the different structures surrounding it; for this reason it has been necessary to find an adequate simplified model of the given problem. In the proposed approach the model simplification is based on the hypothesis that parotid glands deformation is attributable to two different processes acting simultaneously leading to gland changes in shape and position:

- Loss of volume due to damage and loss of acinar cells
- Change in position due to patient face shrinkage process

### 3.1.2 CONTINUUM MECHANICS AND SOFT TISSUE

Continuum mechanics (*CM*) is a field of mechanics concerning with the analysis of the kinematic and mechanical behaviour of materials modelled as a continuum. This hypothesis allows the approximation of physical quantities over the materials at the infinitesimal limit and differential equations can thus be used in describing phenomena. Let  $\Omega$  be a volumetric domain defined in 3D and  $P$  a point inside  $\Omega$ . A deformation occurs in  $\Omega$ , giving rise to a deformed domain  $\Omega'$ , when external forces  $\mathbf{f}$  are applied to some  $P$  in  $\Omega$ . If  $\Omega$  is considered as an elastic body, the deformation is characterized by:

- A displacement vector field  $\mathbf{u}$  caused by  $\mathbf{f}$  applied over one or more  $P$ .

$$\mathbf{u} : P(x, y, z) \in \Omega \rightarrow P'(x, y, z) \in \Omega' \quad (Eq.12)$$

- An internal state of deformation, mathematically defined by a strain tensor for each  $P$  in  $\Omega$ , where strain  $\boldsymbol{\varepsilon}$  is defined as as the ratio of total deformation to the initial dimension of the material body.
- The force reaction of the body to the external forces; this is mathematically defined by a stress tensor  $\boldsymbol{\sigma}$  for each  $P$  in  $\Omega$ .

The analytical relationship defined for each  $P$  in  $\Omega$  that links the displacement, the strain and the stress tensor through *Partial Differential Equations (PDE)* is known as the constitutive law of the material.

The computation of soft tissue deformation for simulation purpose requires some hypotheses about the constitutive law governing soft tissue material elastic behaviour.

Most of the soft tissue modeling works proposed in the literature assumed both, the small strain and the linearity (*Hook's law* based ) of the constitutive law hypotheses.

The term “linear elasticity” is then commonly used, assuming both linearity of the geometry and the mechanics. The rationale behind this hypothesis is clear: the linear relation between applied forces and points displacements leads to very computationally efficient algorithms.

But, linear elasticity is not only a convenient mathematical model for deformable organs: it is also a quite realistic hypothesis; however there is a great diversity of mechanical properties among different soft tissues, usually biological tissue forming liver, lung and glands is expected, in first approximation, to behave as a linear elastic material when the strain is small because these organs are rich in elastin a component with the most linear elastic properties of soft tissue.

The choice of a linear elastic material in modeling parotid gland soft tissue can be considered reasonable: capsule and septa surrounding acinar cells are made up of dense connective tissue which is rich in elastin (*fig.47*).

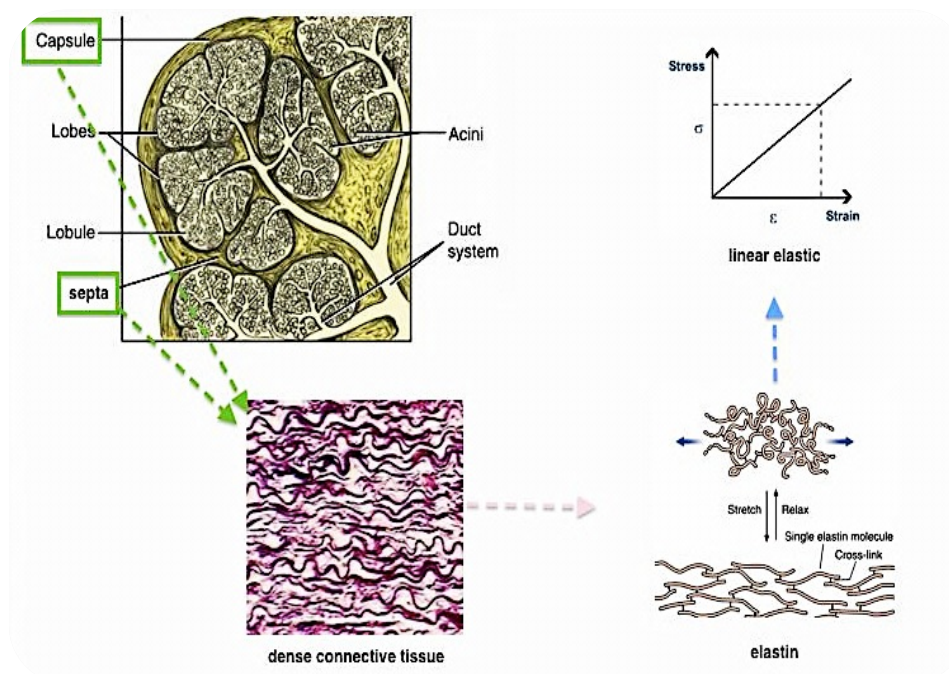
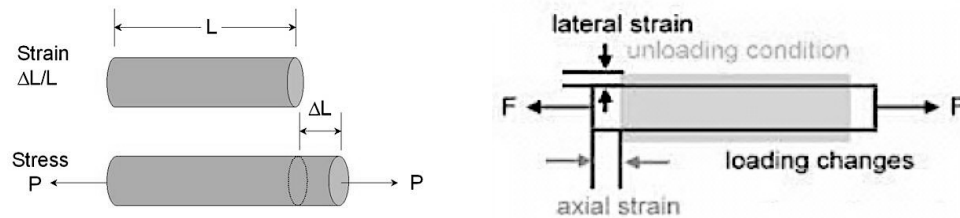


**Figure 47:** cross sectional view of parotid gland structure where capsule and septa structures are highlighted: they are made up of dense connective tissue rich in elastin fibres characterized by linear elastic behaviour.

In the linear elastic case, it can be shown that the constitutive behaviour of the material can be characterized by only two parameters:

- **Young's modulus ( $E$ ):** a coefficient of elasticity of a substance, expressing the ratio between a stress that acts to change the length of a body and the fractional change in length (*strain*) caused by this force (*Eq.13*) (greater the modulus, stiffer the material).
- **Poisson's ratio ( $\nu$ ):** it is related to the compressibility of the material defined as the ratio of transverse contraction strain to longitudinal extension strain in the direction of stretching force (*Eq.14*).



$$E = \frac{\text{stress}}{\text{strain}} = \frac{\sigma}{\epsilon} = \frac{P}{\Delta L/L} \quad (\text{Eq.13})$$

$$\nu = \frac{\text{lateral strain}}{\text{axial strain}} \quad (\text{Eq.14})$$

**Figure 48:** schematic representation of Young's Modulus (left) and Poisson ratio (right) definitions

In modeling parotid gland morphing a linear isotropic elastic material will be used and the governing equations to be solved for a linear elastostatic<sup>17</sup> body is the *Navier-lamè* equation (*eq.15*):

$$\mu \nabla^2 \mathbf{u} + (\lambda + \mu) \nabla (\nabla \cdot \mathbf{u}) + \rho \mathbf{b} = 0 \quad (\text{Eq.15})$$

where

$\mu, \lambda = \text{Lamè coefficients}$  ,  $\rho = \text{body density}$

$\mathbf{b} = \text{force per mass unit}$  ,  $\mathbf{u} = \text{displacement vector}$

*Lamè coefficients* can be related to *Young's modulus*  $E$  and *Poisson ratio*  $\nu$  :

$$\mu = \frac{E}{2(1+\nu)} \quad \lambda = \frac{E\nu}{(1+\nu)(1-2\nu)} \quad (\text{Eq.16})$$

<sup>17</sup> *Elastostatics is the study of linear elasticity under the conditions of equilibrium, in which all forces on the elastic body sum to zero, and the displacements are not a function of time.*

### 3.1.3 INTRODUCTION TO THE FINITE ELEMENT METHOD

Whatever the modeling assumptions are, the *PDEs* that govern *CM* of an elastic body cannot be analytically solved over the full domain for complex shape. They need to be numerically solved over a piecewise discretization of the domain. The finite element method (*FEM*) is one of the most powerful numerical methods available for solving boundary value problems for partial differential equations defined over complex shapes. *FEM* name is due to the principle that the continuous space that we want to model is subdivided in a finite number of smaller and simpler geometries, namely the elements where *PDE* can be numerically solved. This subdivision of the continuous space is called the *FEM* mesh. The subdivision of a whole domain into simpler parts has several advantages:

- Accurate representation of complex geometry
- Inclusion of dissimilar material properties
- Easy representation of the total solution
- Capture of local effects

Performed the discretization of the spatial domain  $\Omega$  with “*finite elements*” interconnected at points called “*nodes*”, the *PDE* of the *CM* can then be solved inside each element which geometry is quite simple and regular. For a given set of boundary conditions (i.e. forces and constraints applied on nodes) and assuming an analytical constitutive law, the unknowns of the systems, i.e. node's displacements, are solved for each element. Then due to interpolation “*basis functions*” (usually linear or quadratic), displacements, strains and stresses can be computed at each point inside the elements. One of the benefits of using the finite element method is that it offers great freedom in the selection of discretization, both in the elements that may be used to discretize domain and the basis functions. Because of element interconnections and continuity of the shape functions from one element to another one, the *FEM* provides solutions of the system inside the full domain. *Figure 49* shows an example of a deformed domain obtained using *FEM*. In this example, an external force  $\mathbf{f}$  is applied over node A. Node B is considered as fixed (this is an example of constraint applied over a node). The position of the other nodes in the mesh is obtained in function of  $\mathbf{f}$  and all the model parameters in each node (strain, stress and constraints). Finally the position of each point in the domain is obtained by the interpolation function over each element.

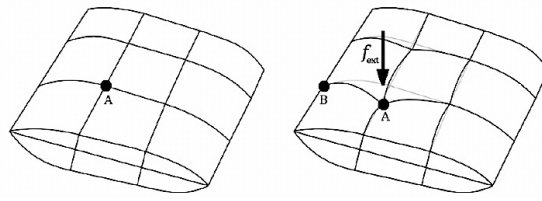


**Figure 49:** An example of a deformed domain simulated with FEM. Left: the initial system Right: the domain is deformed under the influence of an external force

In general the following steps are necessary to solve a boundary value problem by using *FEM* method:

- 1) Formulating the problem as in variational form
- 2) Discretization of the continuous domain
- 3) Choosing basis functions
- 4) Deriving the numerical matrix expression for all elements
- 5) Assembling them into a global matrix equation and solving the derived matrix equation

For the sake of simplicity we will report in detail the basic procedure using FEM to solve steady state heat transfer equation in 2D domain (see appendix 1). However, the procedure and principles are the same for higher dimension and boundary value problems with different equations. The accuracy of the *FEM* calculation depends on the number of the elements we choose to have in the *FEM* mesh. In 3D a discretization of the domain we want to model, requires the creation of a volumetric mesh (*fig.50*). The more element we have more accurate will be the result, however more elements means more calculation to be done for this reason it is necessary to choose the number of elements so that we can obtain adequate accuracy within reasonable computing time. Achieving this subdivision of the space is not an easy task; therefore many ways to produce this tessellation exist.

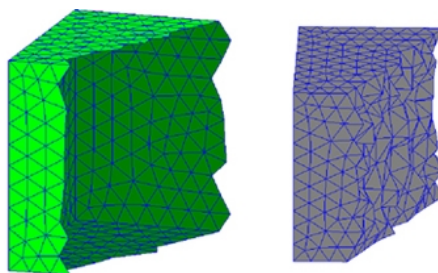


**Figure 50:** Surface mesh (green) and volumetric mesh (grey)

There are different types of elements that can be used to mesh 3D geometries such as linear or quadratic tetrahedron and hexahedron. As *figure 51* shows, in a linear element the element edges are represented as an interpolation of the border points. In the case of quadratic elements, the edges are quadratic functions and therefore an additional middle point is necessary to describe them. If linear tetrahedron have 4 points, its quadratic counterpart has the same 4-point plus 6 others located on each edge of it.

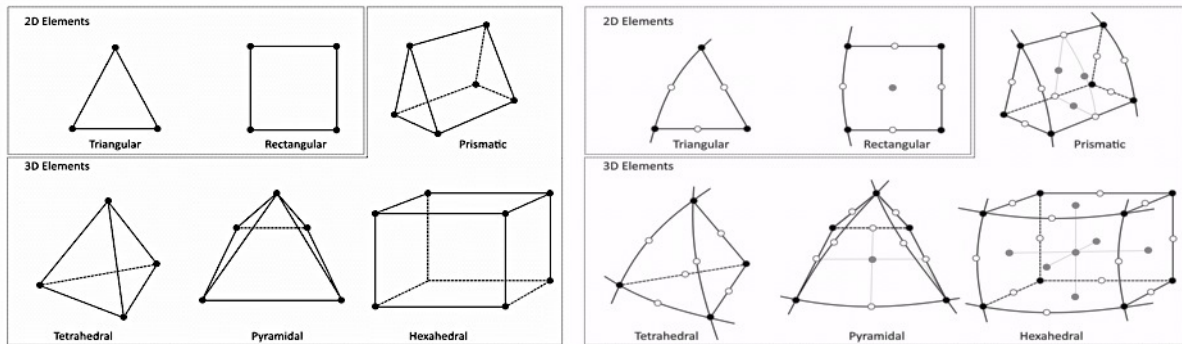


**Figure 51:** Representation of different type of linear and quadratic mesh elements in 2D and 3D domain

As shown by Benzely, Perry et al (1995) [31] from the mechanical point of view FEM meshes made up of second order elements are more adequate in modeling deformable elastic domain providing acceptable results even whit relative coarse mesh; in fact second-order element may assume either concave or convex shape under load condition and furthermore they map precisely to curvilinear geometry.

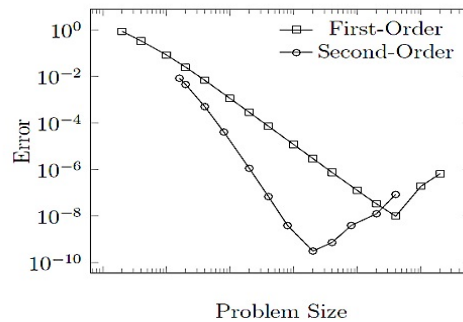


**Figure 52:** plot showing trend of the error<sup>18</sup> in FEM solution estimate for second/first order element vs problem size. Notice that, after a point, the error starts to go back up. This happen once the individual mesh elements start to get very small, and we run into the limits of numerical precision (numbers are smaller than can be accurately represented on a computer.)

<sup>18</sup> Error is defined as integrate the scaled difference between the true and computed solution over the entire model.

$$\epsilon = \int_{\Omega} \left| \frac{u_{computed} - u_{true}}{u_{true}} \right| d\Omega$$

The plot in *figure 52* shows that *FEM* error in solution estimate goes down faster for second order element and decreases as all of the elements in the model are made smaller (increase number of elements). Error estimates can be used to create a denser mesh where the error is large. This goal can be addressed via *Adaptive Mesh Refinement technique*, which first solves on an initial mesh and iteratively inserts elements into regions where the error is estimated to be high, and then re-solves the model as COMSOL® provides.

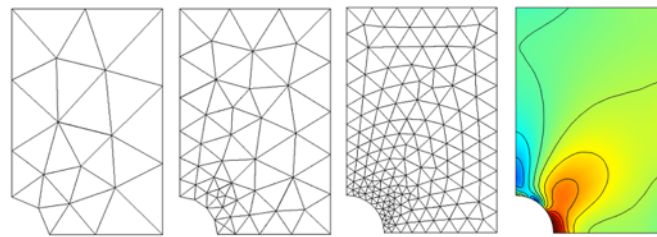


**Figure 53:** *FEM* initial mesh, as well as the results of several adaptive mesh refinement iterations, along with the computed solution of stress analysis<sup>19</sup>

### 3.2 FEM WORKFLOW IMPLEMENTATION INTO COMSOL® MULTIPHYSICS

In order to implement the *FEM* biomechanical model of parotid gland morphing we used the *FEM* software COMSOL® multiphysics. The basic steps necessary to implement our model within COMSOL® environment are reported in the following workflow:

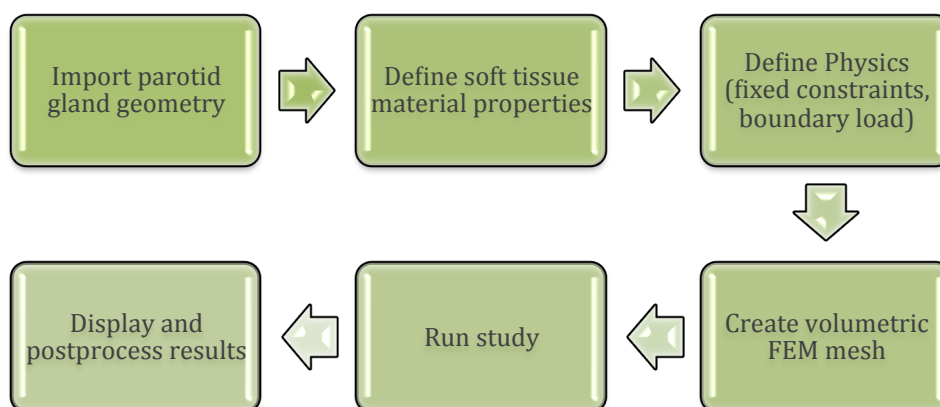


**Figure 54:** Steps necessary to implement parotid morphing *FEM* model into COMSOL® multiphysics

<sup>19</sup> Image taken from <https://www.comsol.com/blogs/meshing-considerations-linear-static-problems/> accessed on 11 June, 2016.



In the model builder window (*fig.55*) every step of the modeling process from defining global variables to final report of results is displayed in the model builder tree. In the following sections we will describe how to implement these steps.

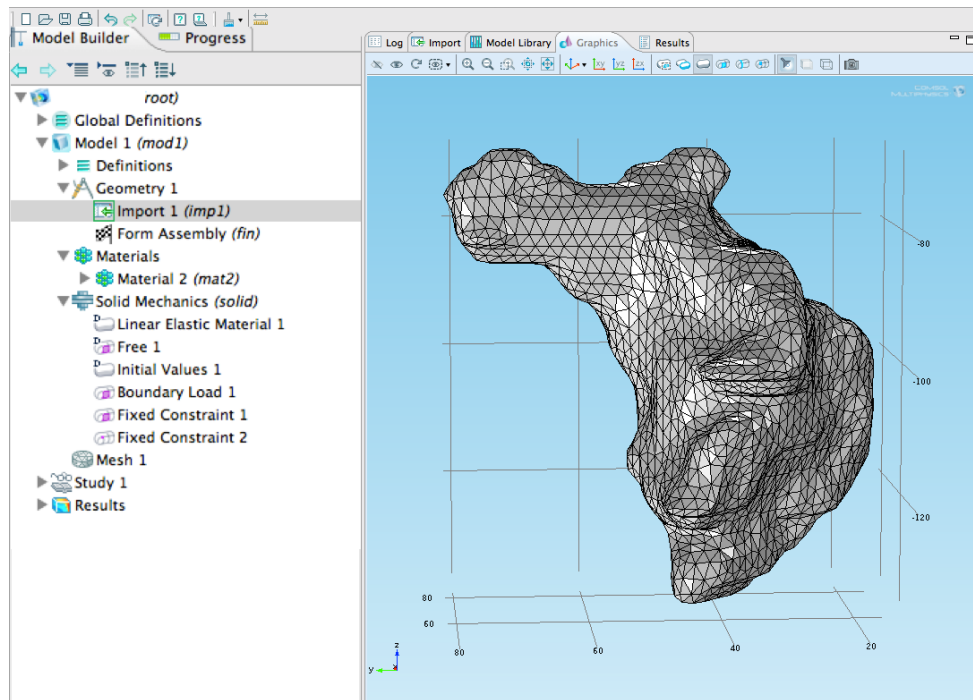


**Figure 55:** Typical example of COMSOL® desktop interface and the model builder window on the left showing every step of the modeling process implemented. In the graphic window the imported parotid gland mesh can be visualized.

### 3.2.1 SETTING UP GEOMETRY AND MATERIALS

Using the model builder window it is possible to import parotid gland mesh exported in *.stl* file format from 3D Slicer and obtained as described in chapter 2 from patient *CT* images. Then it is possible to convert it into solid and finally display the imported geometry in the Graphics window (*fig.55*). One of the most important issues in modeling construction phase is the material selection. The material node allows to choose among different material models for structural mechanics analysis. To simplify the analysis and in agreement with information reported in 3.1.2, parotid gland tissues are idealized as homogeneous, linear elastic and isotropic. COMSOL® material library contains data for more than 2,700 materials such as semiconductors, metal alloys, minerals and other materials that characterize mechanical components of systems commonly analysed by using this software.

In order to match COMSOL<sup>®</sup> capabilities with our requirements of modeling soft tissue, a new material type has been defined. In the linear elastic material node it is possible to create the specific material needed for the simulation of parotid gland tissue, defining density, Poisson ratio and Young's modulus value. Current imaging techniques such as *CT*, do not directly measure the elastic properties of soft tissue, furthermore clinical workflow of our tomotherapy patients doesn't provide any type of clinical examination able to give us this type of information; for this reason for what concern Young's modulus a rough estimate have been obtained by using values reported in literature. Ultrasound scanners are the most frequently applied imaging method able to provide information about the local elastic properties of soft tissues. Elasticity values of parotid gland were determined with shear-wave ultrasound elastography by Kernal Arda et al. [30] finding mean Young's modulus value of  $10.6 \pm 2.9$  kPa for men and  $10.2 \pm 3.7$  kPa for woman. The optimal Young's modulus parameter value for each patient parotid gland will be find using a parametric sweep study.

Parotid gland *CT* Hounsfield unit is around *15-25 HU* corresponding to density value of  $1 \text{ g/cm}^3$ . Next evolution of the present work could be to discretize gland subvoxels in specific density value due to MRI imaging, PET imaging or fluorescent imaging.

Poisson ratio has been fixed to 0.49 value as suggested by other soft tissue modeling works. Soft tissue in fact is a composite material that consists of both incompressible and compressible ingredients. Tissues with high proportion of water, for instance water-rich parenchymal organs such as parotid gland can be modelled as incompressible materials (Poisson ratio  $\sim 0.49$ ).

	Elastic model	Young's Modulus (Pa)	Poisson ratio	Density (g/cm <sup>3</sup> )
<b>Parotid glands</b>	Linear, homogeneous and isotropic <sup>20</sup>	$\sim 10000$	$\sim 0.49$	1

**Table 7:** Material model and properties of the implemented parotid gland morphing model

<sup>20</sup> Linearity :Directly proportional relation between stress and strain

Elasticity: Time-independent mechanical behavior. Loading and deformation independent of time.

Isotropy:The elastic constants are independent of loading direction

Homogeneous: The elastic properties are the same over all organ domain

### 3.2.2 LOADING AND BOUNDARY CONDITIONS

With the geometry and materials defined, it is now possible to set loading condition and boundary condition. It is reasonable to consider that loss of acinar cells due to radiation exposure empties parotid lobules; as a consequence we can consider that the surrounding capsule and septa, previously stretched by the acinar cells presence, relax producing shrinkage of the gland.

In our biomechanical model the shrinkage process of PGs due to damage and loss of acinar cells exposed to radiation, has been modelled as a force field acting on each parotid surface mesh element along surface element's normal direction and pointing in the internal region of the gland (*fig.56*).

The optimal intensity value of the force field will be find running a parametric sweep and comparing real deformation of parotid gland with simulation results.

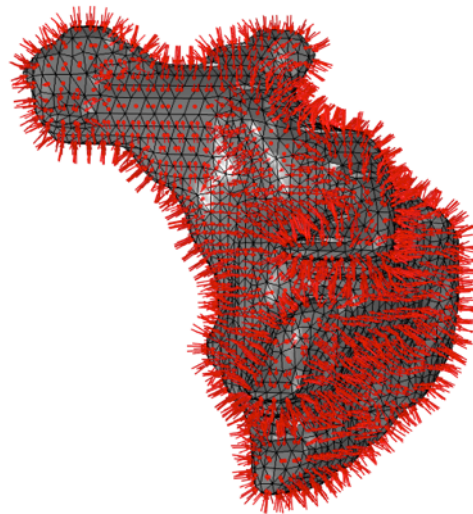


**Figure 56:** *example of loading condition implemented in our model approach showing a force field acting on each parotid mesh element along surface element's normal direction  $\mathbf{n}$  and pointing in the internal region of the gland. In our approach it represents parotid shrinkage process due to loss of acinar cells*

During parotid shrinking process it must be take into account that parotid hold on to the structures that pass through it (parotid duct, external carotid artery) and those it touches (mandible, masticator space muscle). Making simulation which enables interaction of touching structure is computational very damaging, furthermore parotid duct ,veins and artery that pass through it are

not visible from our *CT* images, so some simplifications have to be made in order to define the *FEM* model fixed constraints.

In our approach fixed constraints were defined by manually selecting the points of the imported parotid mesh which come into contact with reconstruction of tubular structures whose aim is to mimic the motion block carried out by parotid touching structures during gland shrinkage process. This structures were obtained by using a 3D Slicer tool (*curve maker*) that lets you create tubular objects connecting landmarks defined on the slices of *CT* images, that were respectively placed taking into account the position of the second molar and the retro mandibular branch.

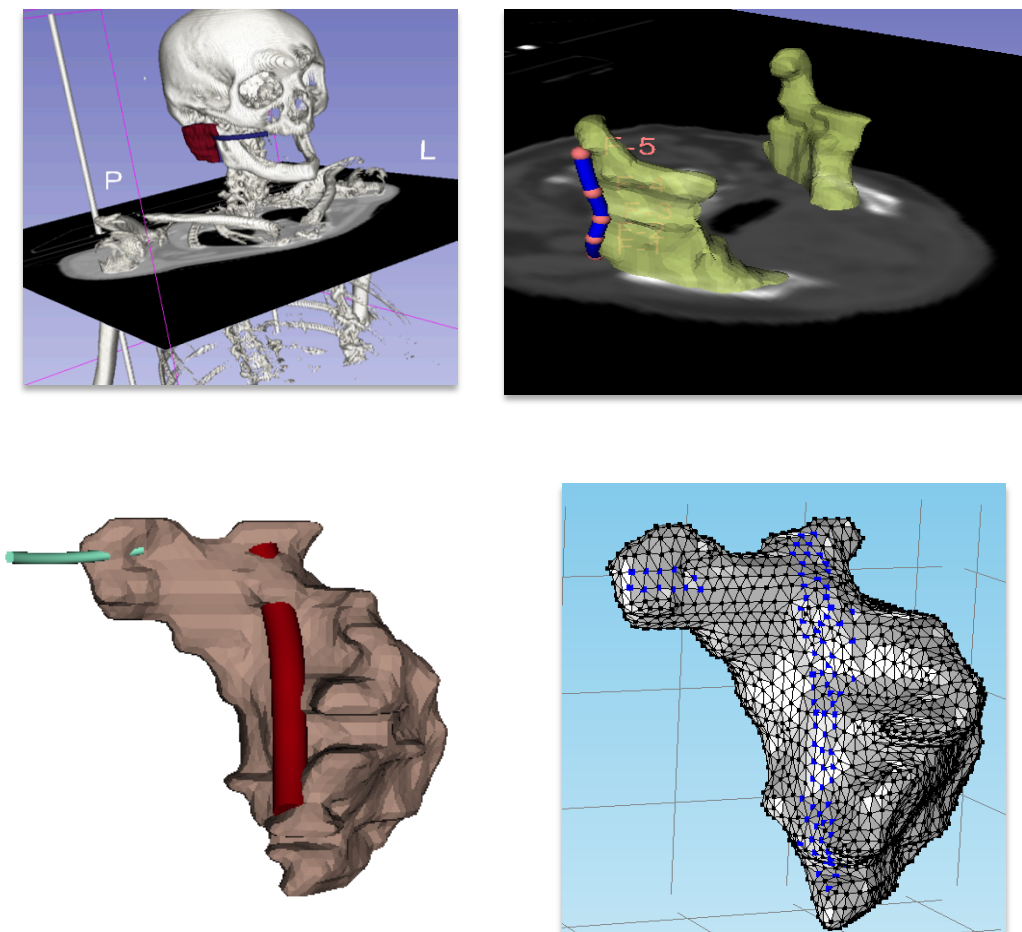


**Figure 57:** Right bottom box shows *FEM* fixed constraints points obtained manually selecting points of the imported parotid mesh which comes into contact with the reconstruction of tubular structures mimics the motion block carried out by parotid touching structures (mandible, retromandibular vein, carotid artery, parotid duct, masticator space muscle) during gland shrinkage process. Tubular structures were obtained using curve maker 3D Slicer toolbox considering second molar position and retro mandibular branch as shown in top boxes. Bottom left image shows an example of the final tubular structures obtained

### 3.2.3 FEM VOLUMETRIC MESH GENERATION

Meshing geometry is an essential part of the simulation process, and can be crucial for obtaining the best results in the fastest manner. Although the element edges always appear straight for graphics performance purposes, by default COMSOL<sup>®</sup> uses second-order element. In our model tetrahedron second order elements will be used to construct volumetric 3D *FEM* mesh (fig.59). COMSOL<sup>®</sup> has nine built-in size parameter sets for *FEM* mesh creation ranging from extremely fine to extremely coarse with normal sitting right in the middle.

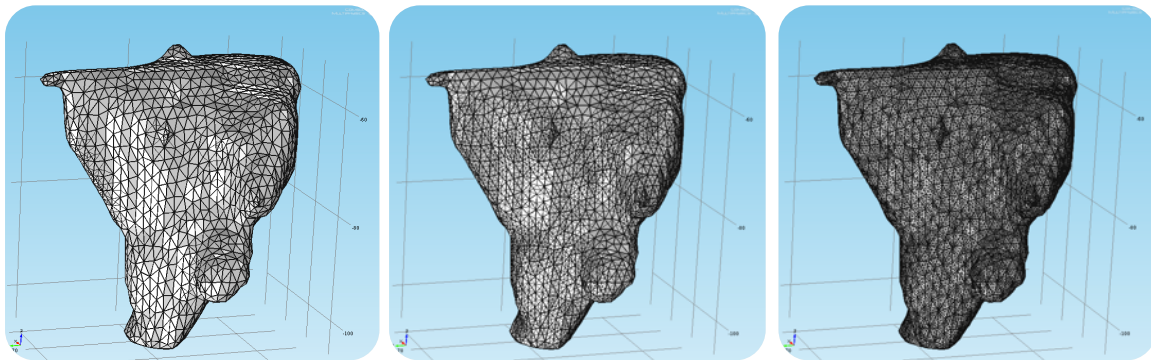


**Figure 58:** Example of normal, fine and extremely fine FEM mesh automatically created by COMSOL<sup>®</sup> for FEM implementation

Considering that in our situation the geometry contains small edges and faces, it is necessary to define a slightly finer mesh than the default setting suggests. This will give a more accurate result. Even though refining the mesh size to improve computational accuracy always involves some sacrifice in speed and typically requires increased memory usage.

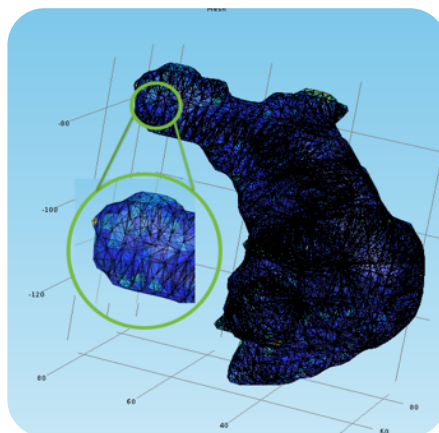


**Figure 59:** tetrahedral internal structure of our 3D FEM mesh

An important parameter to take into account to obtain a good *FEM* mesh is the quality of mesh element. Good shaped mesh element provides a more accurate solution. It is possible to evaluate mesh quality defining a mesh quality metric  $Q$  for tetrahedral element  $T$ :

$$Q(T) = \alpha \frac{\rho}{h} \quad (Eq.17)$$

$h$  : it is size of the element longest edge

$\rho$  : it is  $T$  in-radius

$\alpha$ : it is a scaling factor so that the quality of an equilateral element is 1.

Thus  $Q$  ranges from 0 at worst to 1 at best. Mesh quality histogram from extremely coarse, normal and finer mesh of parotid gland is reported (*fig 60*). The  $x$  axis represents element mesh quality value ranging from 0 to 1 while  $y$  axis represents the number of mesh elements belonging to the corresponding mesh quality value bin. We can see that increasing the number of tetrahedral elements, mesh quality histogram shows an increasing number of elements with high quality value. In order to balance result accuracy and computational time ,*finer FEM* mesh size has been choose.

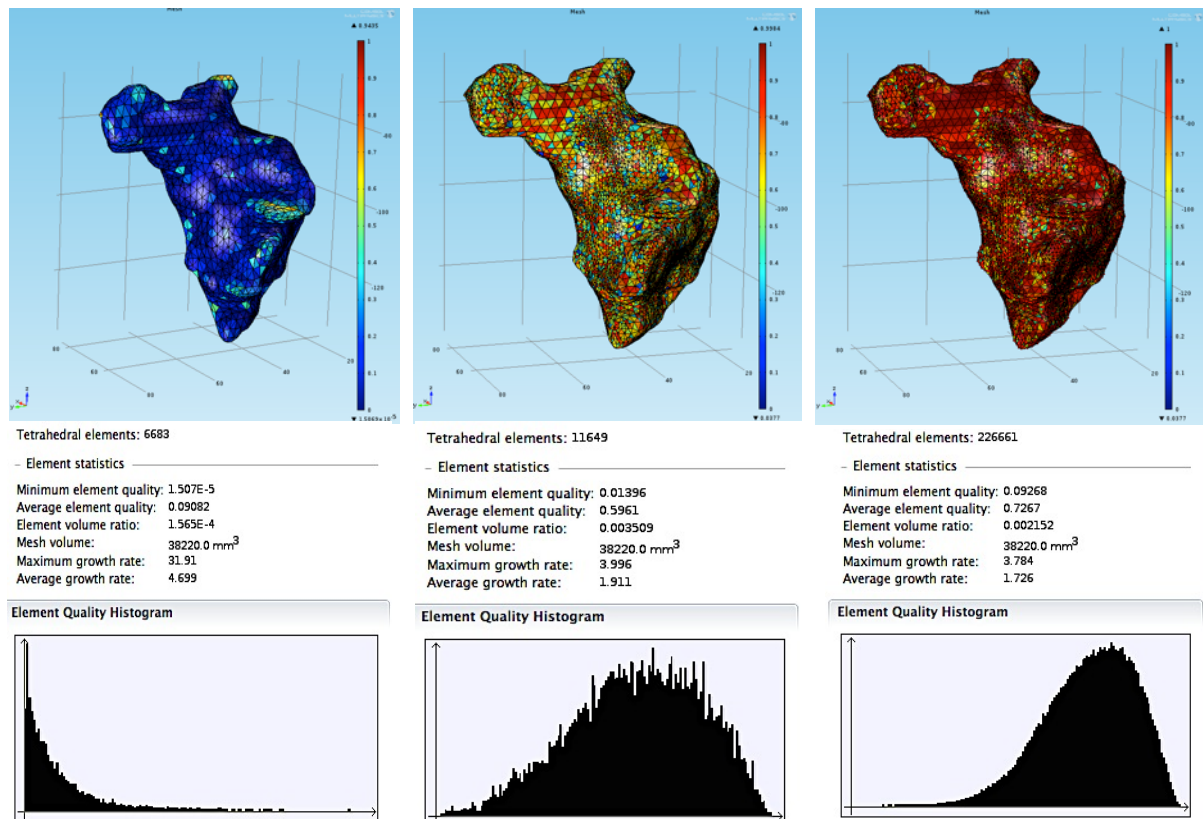


**Figure 60:** parotid surface with element quality coloured map and correspondent mesh quality histogram

### 3.2.4 RUN STUDY AND DISPLAY RESULTS

Selecting stationary study option, COMSOL® will use a stationary solver to solve the linear elastostatic problem defined by (Eq.15). A surface map visualization of the displacement with respect to initial configuration can be seen in the graphic window when the solver finishes to run. The assumption of a force field acting on each element along normal direction, pointing in the inner portion of the gland and fixed constraints depending on parotid duct, mandible and vein-artery system presence produce the pattern of deformation shown in *figure 61*. Posteromedial region is the one that shrink the most in agreement with real pattern of deformation observed (see. 4.1). Study node allows to perform parametric study in order to run several simulation with loading condition and elastic parameters ranging in predefined intervals. Parametric sweep option will be used to perform simulations with different load condition and elastic parameters in order to find optimal parameter model values able to match with the real pattern of deformation observed. For this reason the workflow reported in the following section has been implemented.

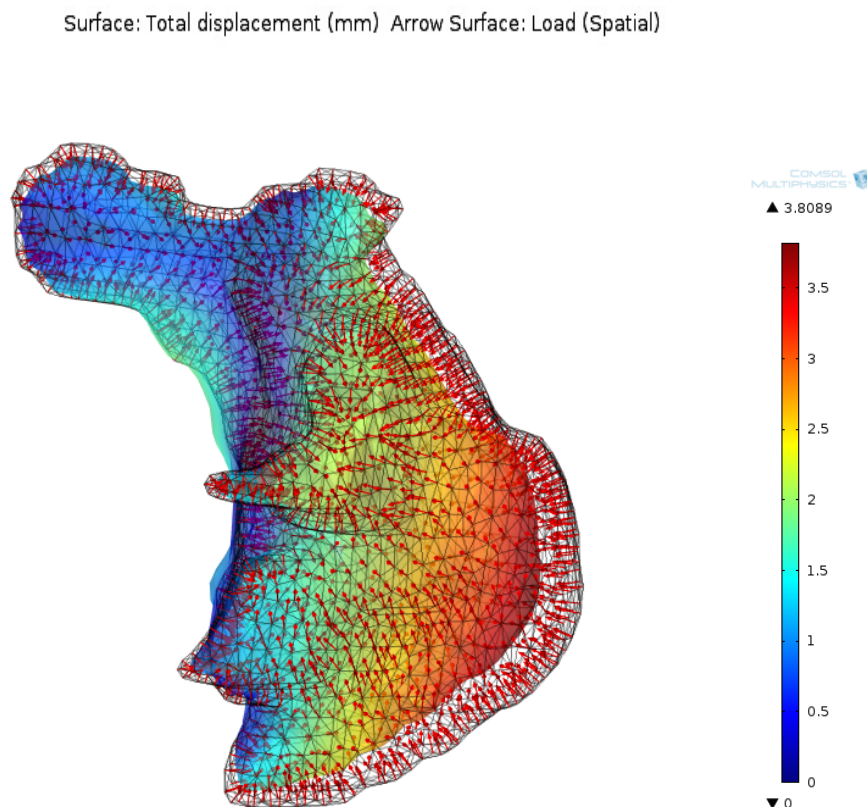


**Figure 61:** Illustration of total displacement surface coloured map obtained setting up force field with modulus value of 170 N for each vector acting on mesh element normal direction and a Young's Modulus of 6 kPa.

### 3.2.5 WORKFLOW OF THE SIMULATIONS

Using the basic steps of *FEM* modeling, the workflow in *figure 62* has been realized for each patient in order to predict parotid shrinkage at 15-th day and 31-st day of the treatment.

Since the range of elastic parameters that is often found in the literature can only be viewed as approximate, in our approach we have choose to estimate these elastic properties and force field intensity from the training set by using a leave one out cross validation approach following these steps:

1. Define a metric in order to quantify difference between real and simulated deformation
2. Leave one of the training samples out
3. For the remaining training samples run simulation for different value of force field intensity and elastic parameter
4. Compute optimal parameter values for the leave out sample as the average of the training sample value that have minimized metric defined at 1
5. Use the optimal values obtained from 4. to model and predict the leave one out sample deformation using *FEM* model procedure
6. Repeat steps 2 - 5 for each training sample

The metric that has been chosen to quantify difference that occurs between real and simulated deformation is the root mean square displacement error, defined as:

$$RMSDE = \sqrt{\frac{1}{n} \sum^n (x_{sim} - x_{real})^2 + \frac{1}{n} \sum^n (y_{sim} - y_{real})^2 + \frac{1}{n} \sum^n (z_{sim} - z_{real})^2} \cdot \sqrt{\frac{1}{3}} \quad (Eq.18)$$

where  $n$  represents number of mesh points,  $x_{real}$   $y_{real}$   $z_{real}$  represent real morphed mesh points coordinates while  $x_{sim}$   $y_{sim}$   $z_{sim}$  represent simulated morphed mesh points coordinates obtained as output of *FEM* simulation.



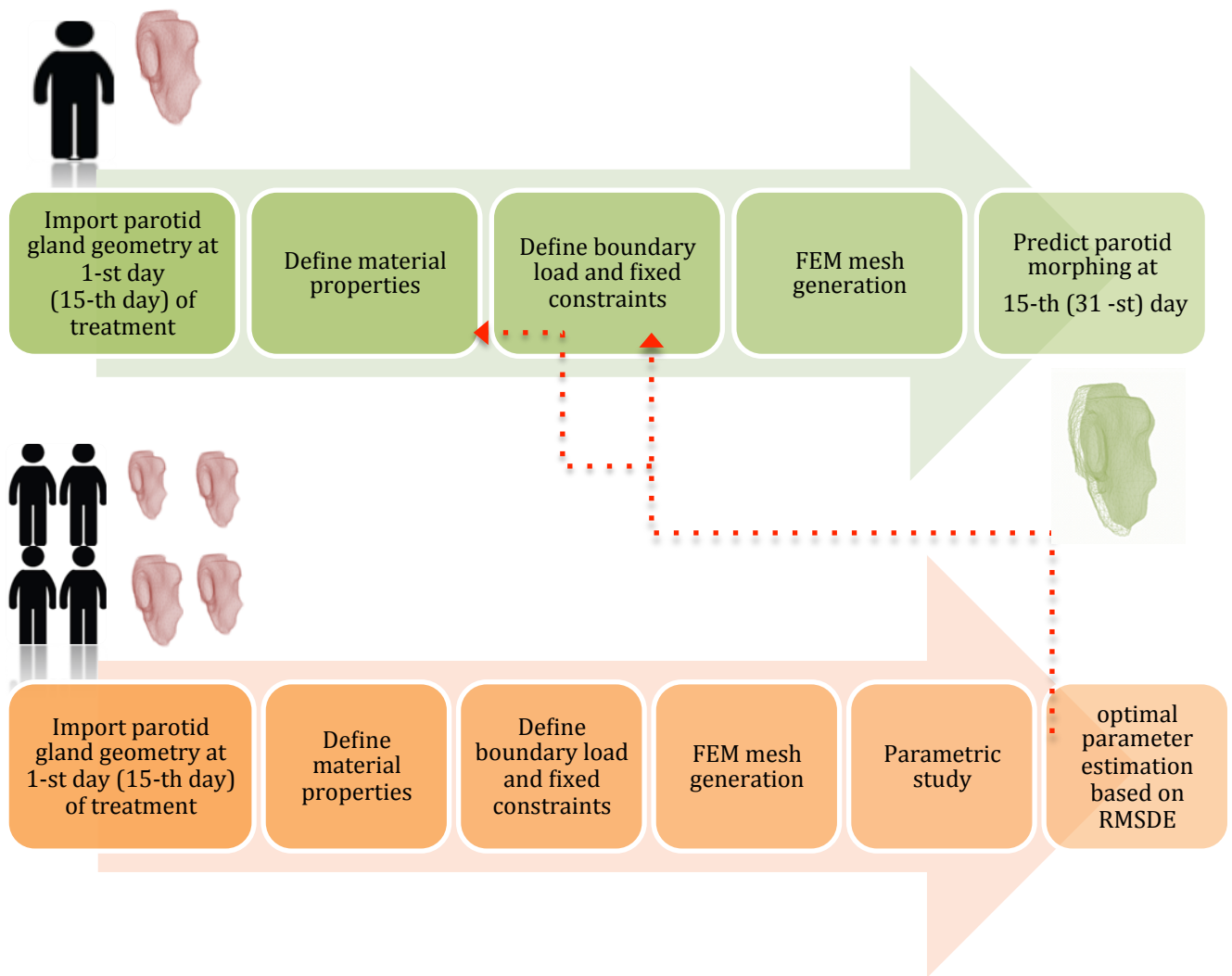


**Figure 62** :Workflow of the leave one out procedure implemented in order to estimate each patient optimal force field intensity and Young’s modulus of morphed parotid gland

<i>Number of parotid mesh used</i>	<i>Average tetrahedron mesh quality <math>Q (T)</math></i>	<i>Average number of tetrahedron elements for each mesh</i>	<i>Number of simulation performed</i>
32	0.7 [max 0.9 –min 0.5]	250000 [max 260000–min 220000]	2016 <sup>21</sup>

**Table 8:** summary of the simulations performed

<sup>21</sup>  $2(\text{period of morphing considered}) * 63 (\text{all possible combinations of load and elasticity parameters used}) * 16 (\text{number of parotids})$

## 4. RESULTS

### 4.1 QUANTIFICATION OF PAROTID GLANDS MORPHING

The availability of parotid surface mesh created by using the implemented workflow (*fig.23*) allows us to quantify and characterize the dynamic of parotid shrinkage process during the course of *RT* treatment in terms of:

- Volumetric variations
- Surface variation
- Shape morphing

All data analysed has been collected from 3D Slicer. First results reported regards the daily trend of parotid gland volume reduction with respect to treatment start (*fig.63*). A box plot notation has been utilized, where the minimum and maximum are represented by black extreme of the box. First and third quartile are coloured side of the box, a point represents median value. All patients showed a substantial reduction of parotid gland volume at the end of treatment with respect the first fraction in accordance with results from other authors (see *Table 2*) (Left PG volume reduction at the end of treatment: mean =28.5%, max=41.5%, min = 26.0% Right PG volume reduction at the and of treatment: mean= 28.4 %, max = 38 0%, min =23.0 %).

The daily trend of parotid surface area reduction with respect treatment start has also been investigated. Results are displayed for both PGs (*fig.64*); all patients showed a substantial reduction of parotid gland surface at the end of treatment with respect to the first day of treatment (Right PG: mean reduction =15.3%, max reduction=21.5%, min reduction = 11.5% Left PG: mean reduction =15.4%, max reduction=16.9%, min reduction = 14.5%).

Using DICE coefficient index the daily trend of gland shape deformation in terms of reduced overlap with its geometry at start of treatment has been evaluated. All patients PGs show at the end of treatment a decrease of DICE index with respect to parotid gland geometry at first fraction (Right PG: mean DICE = 0.79, max DICE = 0.8, min DICE = 0.59 Left PG: mean DICE=0.76, max DICE=0.84, min DICE = 0.67) in accordance with a deformation process consisting of gland motion towards the centre of the oral cavity and volume reduction at the same time (*fig.65*).

## PGS VOLUME CHANGE DURING TREATMENT COURSE

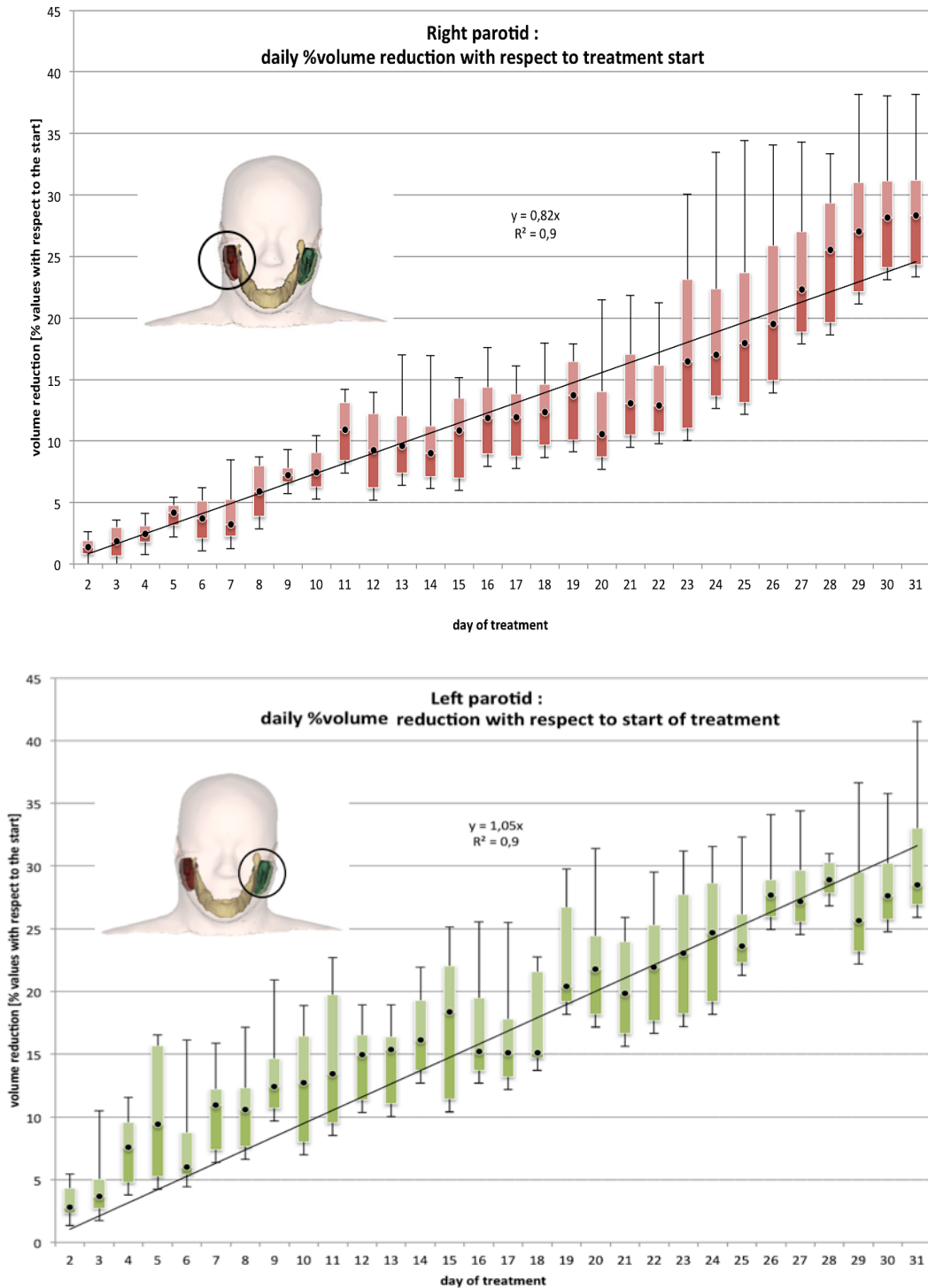


**Figure 63:** Box Plot of daily left (green) and right (red) parotid volume reduction. The black line is the linear regression of % volume reduction with respect to start of treatment

PGs SURFACE VARIATION DURING TREATMENT COURSE

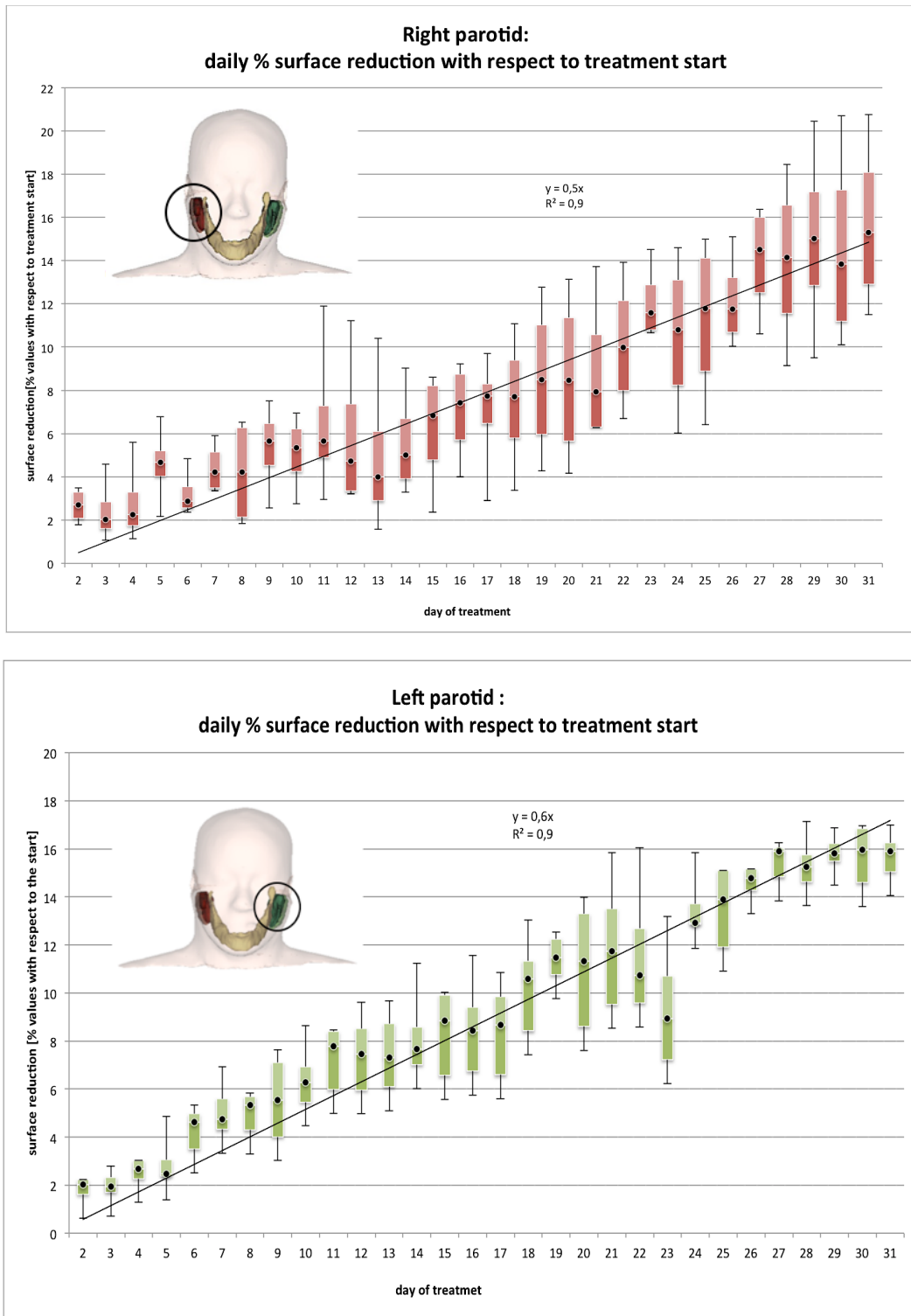


**Figure 64:** Box Plot of daily trend of right (red) and left (green) parotid surface reduction. The black line is the linear regression of % surface reduction with respect to start of treatment

PGS SHAPE MORPHING DURING TREATMENT COURSE

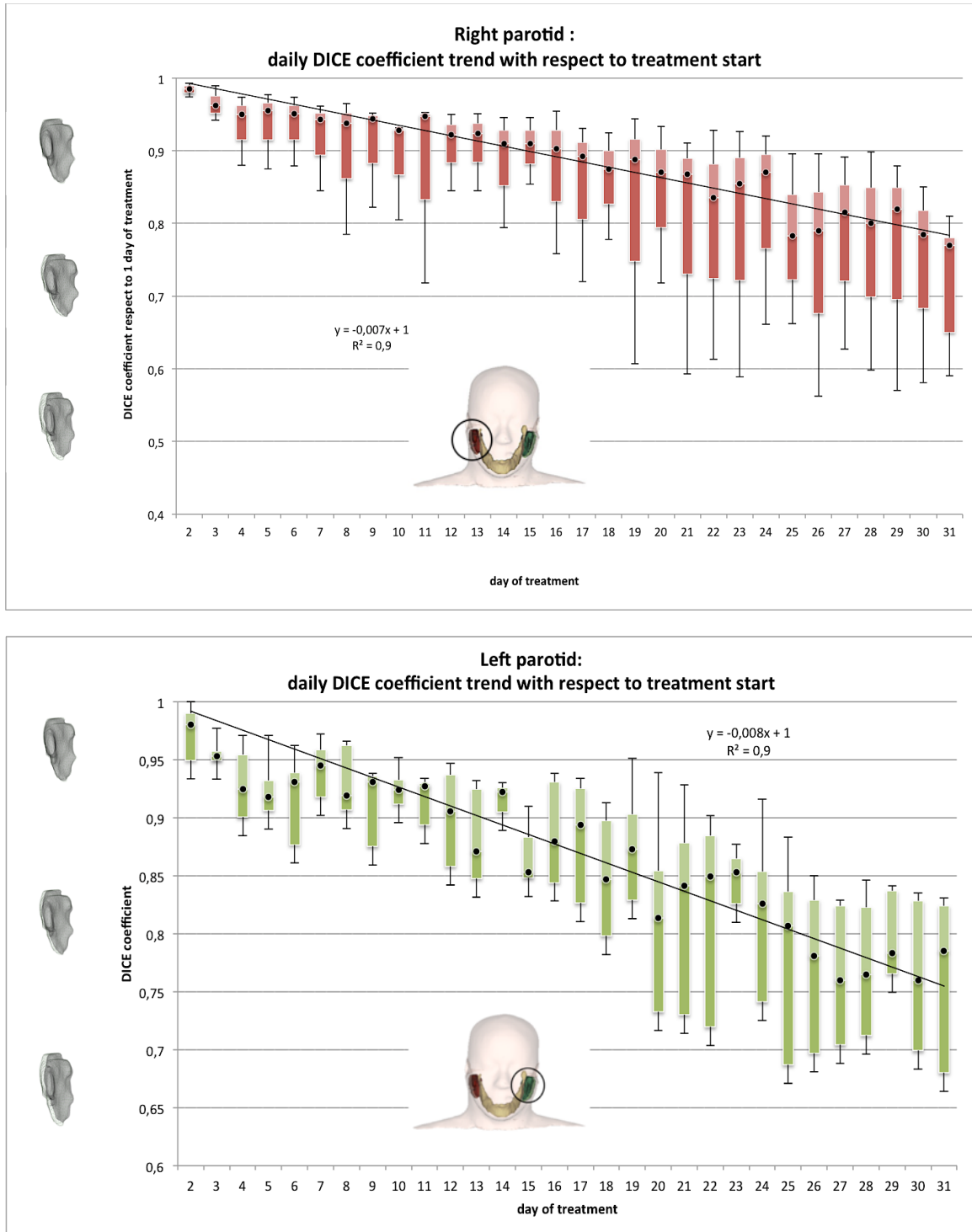


**Figure 65:** Box plots notation representing right and left PGs daily DICE index computed with respect to gland geometry at treatment start .

All the metrics used to evaluate parotid shrinkage suggest that it is a dynamic progressive process occurring in linear fashion in terms of volume, surface and *DICE index* reduction with respect to first fraction , as time of treatment elapses (*Table 9*).

ROI	Volume reduction	R <sup>2</sup>	Surface area reduction	R <sup>2</sup>	DICE Coefficient reduction	R <sup>2</sup>
Left parotid	Linear trend 1%/day	0,87	Linear trend 0,6%/day	0,94	Linear trend: 0,008 DICE unit/day	0,86
Right parotid	Linear trend 0,8%/day	0,92	Linear trend 0,5%/day	0,96	Linear trend: 0,007 DICE unit/day	0,91

*Table 9: Quantification of PGs shrinkage dynamic in terms of volume, surface and DICE daily trend*

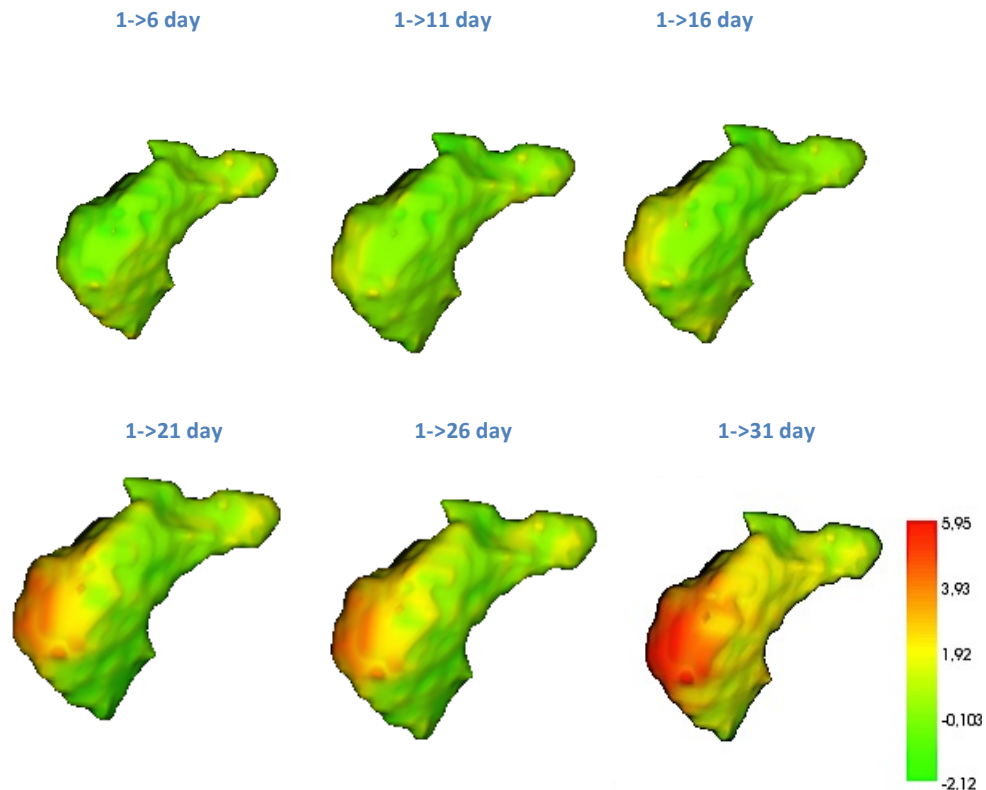


**Figure 66** :weekly distance map of right parotid gland posteromedial region respect to start of treatment. Red regions represent regions subjected to the highest displacement (shranked regions). Distance value (mm)

In order to investigate the spatial pattern of parotid surface change in shape, distance map obtained by using *model to model distance* (see 2.5) have been analyzed. *Figure 66* shows an example of the weekly trend of a single patient right parotid gland distance map with respect to treatment start. Each surface represents parotid gland geometry at first day of treatment with a color map showing each surface mesh point distance from parotid gland geometry at the end of *i*-th week of treatment (where *i* ranges from 1 to 6). As we can see from *figure 66* parotid gland

posteromedial region is subject to a weekly progressive shrinkage process; this process clearly appears at the half of treatment duration.

On the other hand superficial parotid region doesn't show localized pattern of deformation as time of treatment elapses; its displacement pattern is quite uniform as we can see from the displacement map of the same parotid gland reported in *fig.66* with a focus on superficial region (*fig.67*). We want to point out that, as explained in chapter 2.5, fixing parotid gland at treatment start as input mesh, distance map shows positive values for input mesh points placed on the exterior of the compared mesh (regions of the mesh at start of treatment that will shrink during treatment duration), negative distance value are assigned to that input mesh points placed on the interior of the compared mesh (regions of the mesh at start of treatment that will expand or move towards the center of the oral cavity).

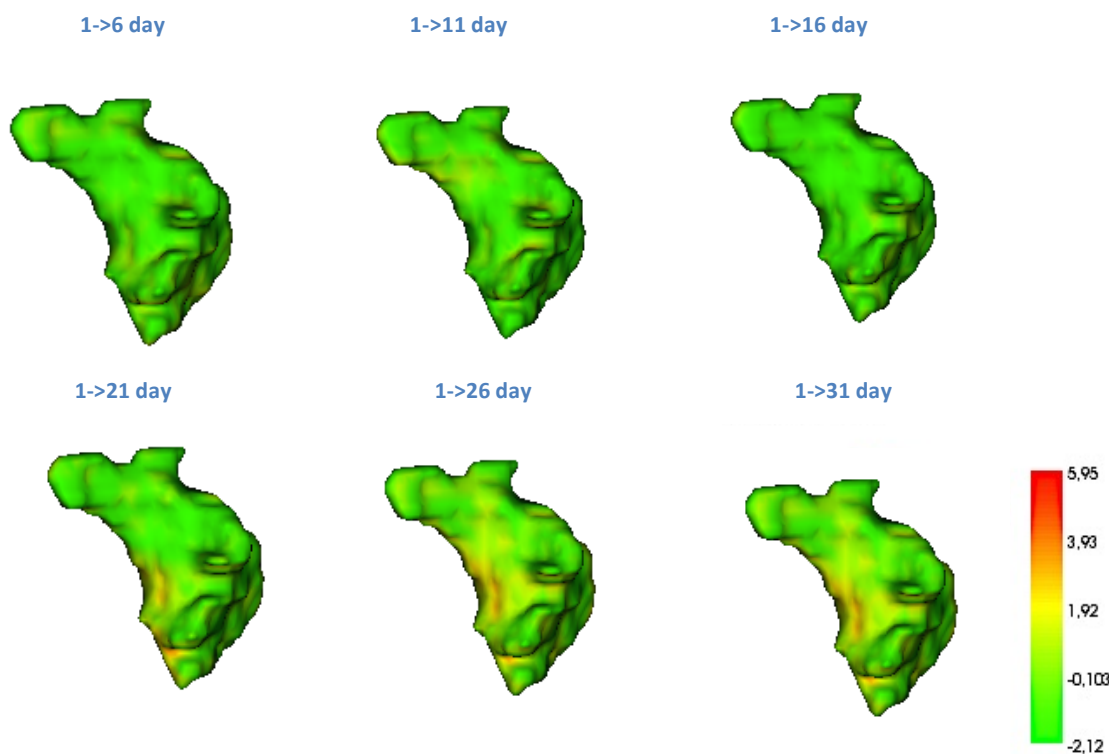


**Figure 67** : weekly distance map of right parotid gland superficial region respect to start of treatment.  
Distance value (mm)

Weekly displacement maps for each patient analyzed in our study are reported in Appendix 3. In order to quantify what have been visually represented in the displacement maps, an histogram representation of the information has been used. Taking into account a single week displacement map, an histogram can be created looking at the displacement value of each mesh point belonging to it and counting the number of points covered by a specific range of displacement.

Mean trend over all patients involved in our study for each week of treatment considered, is reported for both right and left parotid glands (*fig.68*).

Even though 3D histogram plots enclose a lot of information, they are not able to immediately display the dynamic of the investigated phenomenon so they have been represented as a family of 2D curves corresponding to different weeks, where the y-axis represents the % of parotid surface subject to displacement value reported along x-axis. As we can see from *figure 69* curves regarding first week (*1->6 day*) are peaked around 0 displacement value, due to the fact that patient parotid glands after only 5 days of treatment are usually not subjected to evident anatomical changes. As time of treatment elapses curves width enlarges, as it doesn't exist a single dominant value of displacement. At half of treatment duration a second peak appears because a greater amount of surface, usually localized on the posteromedial region, greatly change its position compared to the start of treatment.

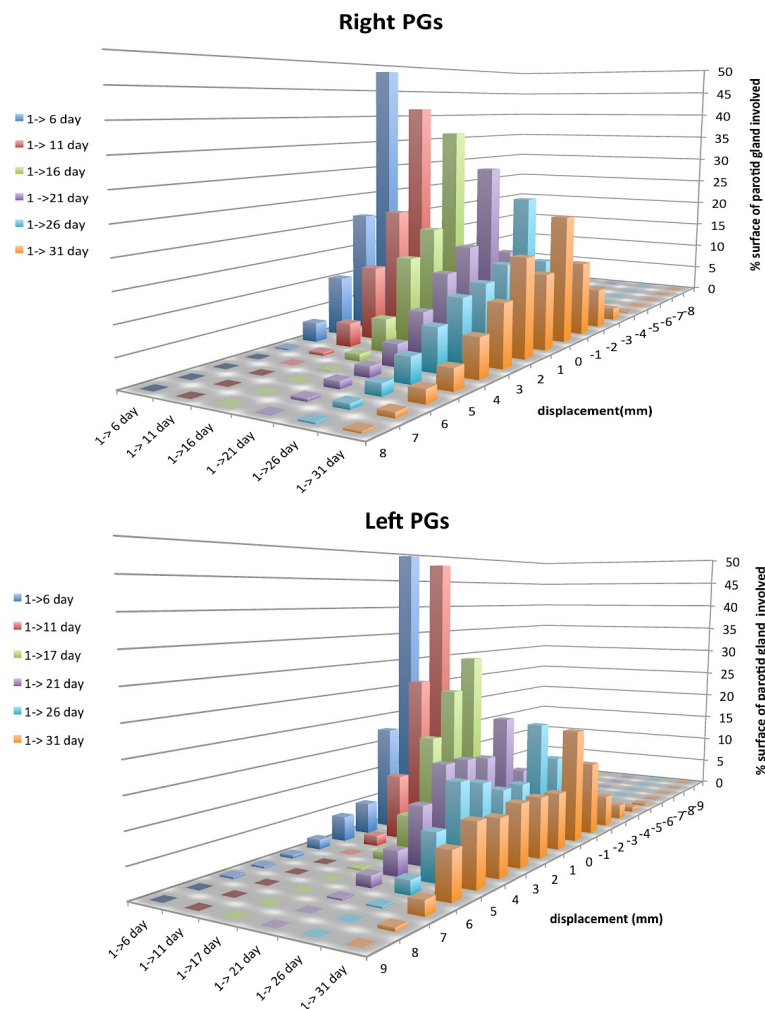


**Figure 68** : Right and Left PG glands 3D histogram plot representing the % amount of parotid surface subject to different values of displacement as time of treatment elapses



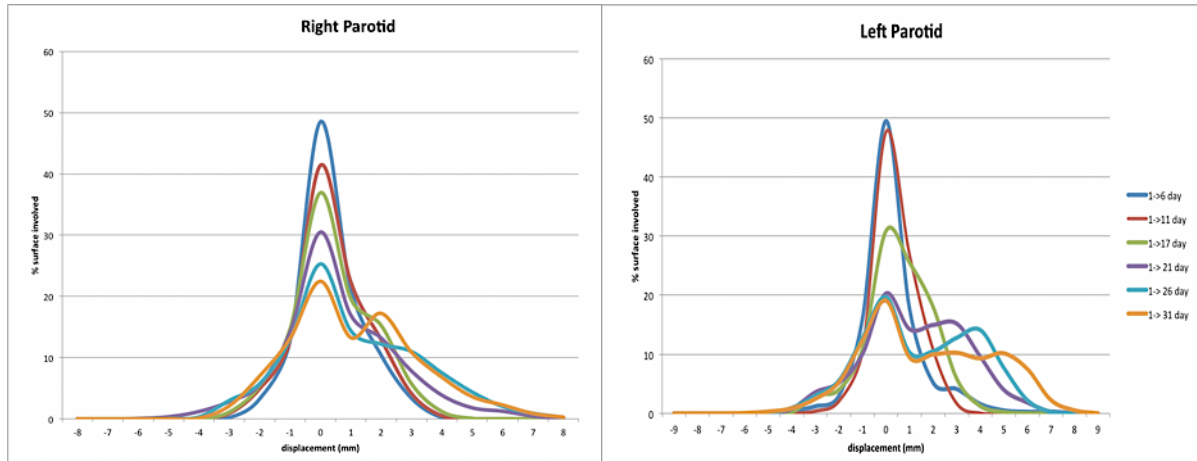


**Figure 69:** curves representing % of right and left parotid gland surface subjected to different value of displacement as time of treatment elapses

Right PG % surface involved						
Displacement (mm)	1->6 days	1->11 day	1-> 16 day	1->21day	1->26 day	1->31 day
0	48,5	41,4	36,9	30,5	25,3	22,5
1	21,3	22,4	19,6	16,9	14,4	13,1
2	10,4	12,9	15,2	13,2	12,2	17,2
3	3,35	4,1	5,7	7,8	10,9	10,9
4	0,2	0,4	1,2	3,8	7,5	6,8
5	0	0	0	1,8	4,36	3,6
>5	0	0	0	1,75	3,19	3,40
-1	12	12	14	14	12,9	13
<-1	4,43	6,8	7,4	10,25	9,25	9,5

**Table 10 :** percentage % values of right parotid gland surface subjected to different value of displacement as time of treatment elapses

Left PG %surface involved						
Displacement (mm)	1->6 days	1->11 day	1-> 16 day	1->21day	1->26 day	1->31 day
0	49,5	47,6	30,9	20,3	19,7	19
1	17,7	26,9	25,5	14,3	10,3	9,5
2	5,2	10,8	18	14,9	10,5	9,9
3	4,1	1,7	5,9	15,28	12,8	10,3
4	1,6	0	1,3	9,6	14,1	9,3
5	0,5	0	0,2	4	7,7	10,2
> 5	0	0	0	2,1	2,5	9,7
-1	15	10	10,9	10	12,8	12,4
< -1	6,4	3	7,3	9,5	9,6	9,7

**Table 11:** percentage % values of left parotid gland surface subjected to different value of displacement as time of treatment elapses

The histogram graphical representation just reported is able to quantify information about % of PGs surface subjected to various displacement values, but it offers no spatial information (it doesn't say where within a surface gland the greatest displacement has occurred). For this reason we have divided PGs surface in five region of interest (ROI) and monitored ROI mean displacement values as time of treatment elapses. ROI were defined on each surface mesh by using 3D Slicer toolbox *Pick and paints*. It belongs to the ShapeAnalysis extension and it allows user to define different regions of interest (ROIs) by positioning a landmark on the 3D model (*VTK file*) and defining a radius for the region (the radius is defined in term of neighbors). It is also possible to propagate ROIs over different models. ROI were defined by positioning landmarks and setting radius value in order to enclose deep PGs lobe (ROI1), lateral region touching parotid duct (ROI2), superficial region touching the duct (ROI3), the remaining superficial region which touches retromandibular ramus (ROI4) and medial region (ROI5). Results obtained and averaged over all 16 PGs of our set are reported in *figure 70* with error bars representing standard deviation values.

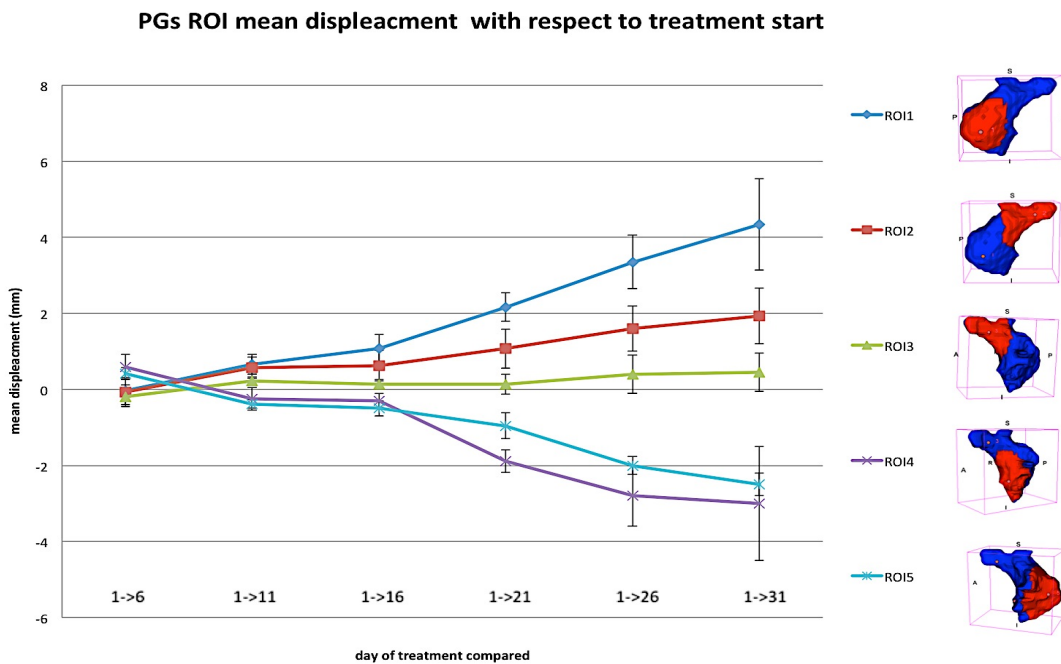


**Figure 70** : PGs ROI mean displacement values as time of treatment elapses. Example ROIs defined on a single patient gland are reported in the legend .

As we expected superficial regions (ROIs 4-5) show negative distance value with respect treatment start as time elapses due to their motion towards the center of the oral cavity, while deep posteromedial regions (ROIs 1-2-3) display increasing positive distance value with respect treatment start geometry due to a shrinkage process that involves especially ROI1.

## 4.2 ACCURACY OF SURFACE RECONSTRUCTION

In order to evaluate the ability of the implemented workflow to correctly reconstruct parotid gland surface from contours traced on CT images a quasar phantom has been used (*fig.71*) . The phantom consists of 3 types of removable inserts. Within the removable inserts there are several objects with known geometry: 1 cube, 2 sphere of different sizes and 1 cone. The phantom has an oval shape and it is made up of a material having the same attenuation coefficient of human soft tissue. Parotid gland surface reconstruction error can be estimated by using a spherical insert ; the parotid gland structure can be thought as made up of a combination of different spheres ,so the ability of recreating curvatures of its surface can be brought back to the problem of reconstructing a spherical surface from its contours.

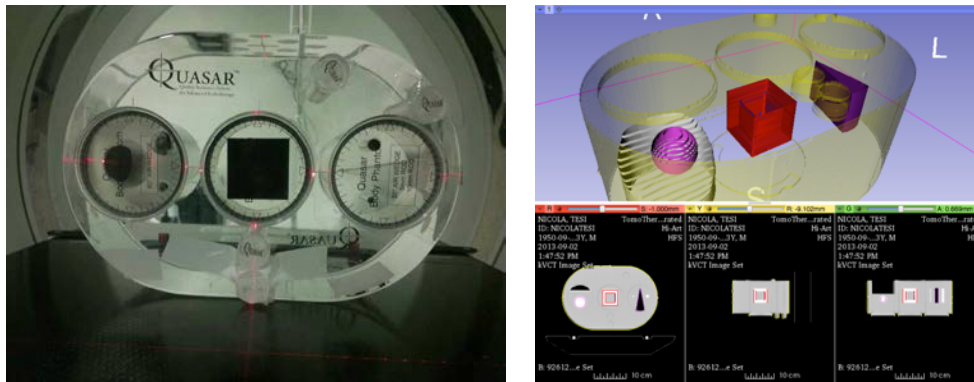


**Figure 71:** Image of the quasar phantom used and its contours representation within 3D Slicer environment

The operations performed in order to evaluate our implemented workflow error in surface reconstruction are reported :

1. The phantom was placed in the *Acquilon CT large bore* unit and aligned with lasers.
2. It has been positioned the insert containing the sphere with a diameter of 3 cm.
3. Acquired image has been sent and imported into RayStation® and the sphere has been contoured.
4. The CT image with contours has been exported and used within 3D slicer environment to reconstruct sphere surface using our method based on marching cube algorithm.
5. Different reconstructions have been performed by using different sampling factor option available within 3D slicer contours node in order to increase the number of element in mesh creation.
6. The created meshes have been compared with the surface of a virtual sphere created using COMSOL® built in geometry creation node and meshed with extremely fine option.

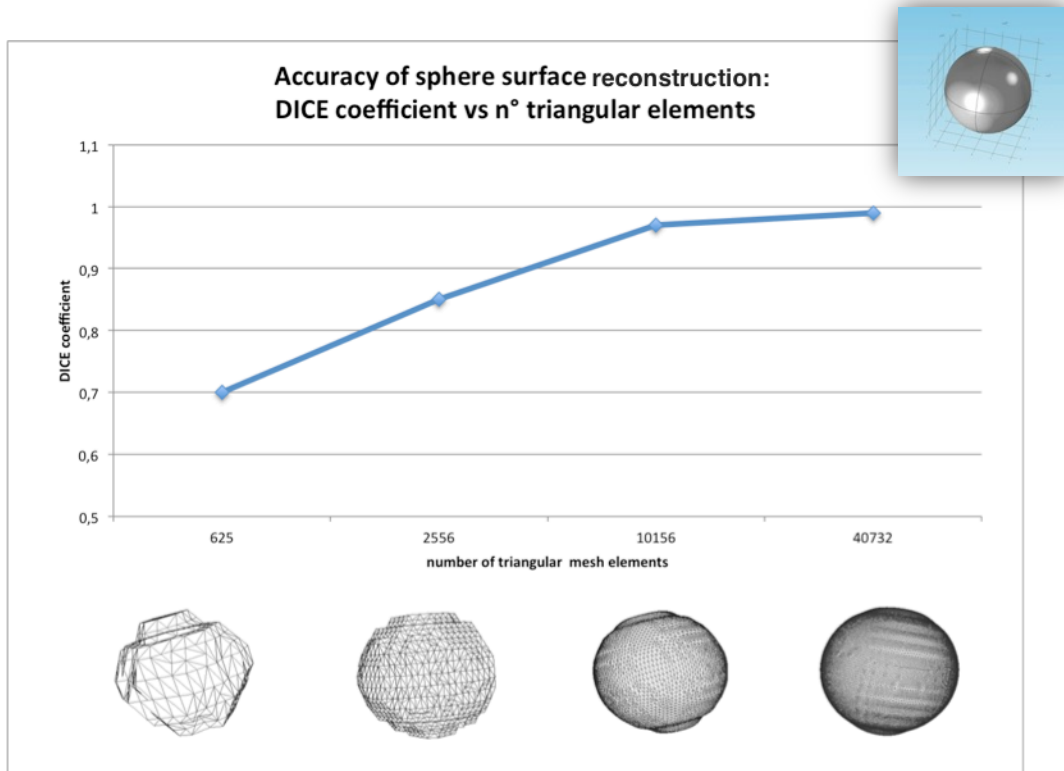


**Figure 72:** error in spherical surface reconstruction process expressed in terms of DICE coefficient with respect to true geometrical model for different mesh size. Bottom light blue box represents the virtual sphere created by using COMSOL<sup>®</sup> and used as true geometrical model.

As we can see from plot in *figure 72*, increasing the number of triangular elements used to reconstruct surface, results in an increase of accuracy expressed in terms of the overlap (*DICE coefficient*) with the true spherical geometry. *DICE* coefficient, surface and volume difference between true and reconstructed spherical surface for different triangular mesh size are reported in *table 12*. Using the maximum value of march cube sampling factor available within *3D Slicer contours tool* we can reconstruct spherical surface by using 40732 triangular elements with a surface difference of 0.7% value with respect to true spherical geometry and a volume error of 1% value, obtaining a complete overlap with the real geometry (*DICE coefficient*= 0.99).

n° triangular elements	Volume difference	Surface difference	DICE coefficient
625	10%	10,5%	0,7
2556	6,8%	8%	0,85
10156	1,5%	1%	0,97
40732	1%	0,71%	0,99

**Table 12 :** *DICE* coefficient, % volume and surface difference between true sphere geometry and its reconstruction by using different number of triangular elements.

### 4.3 FEM BIOMECHANICAL MODEL RESULTS

During the implementation of *FEM* biomechanical model it has been necessary to examine the effect of mesh size and quality *vs.* computational time in order to obtain results with good accuracy in reasonable time. The simulations of a single parotid gland morphing were performed nine times with mesh size varying from extremely coarse to extremely fine. The results of these simulations in terms of computational time and average tetrahedron mesh element quality are reported below (simulations were performed by using Intel core i7 processor (2.2 Hz) with 4GB RAM):

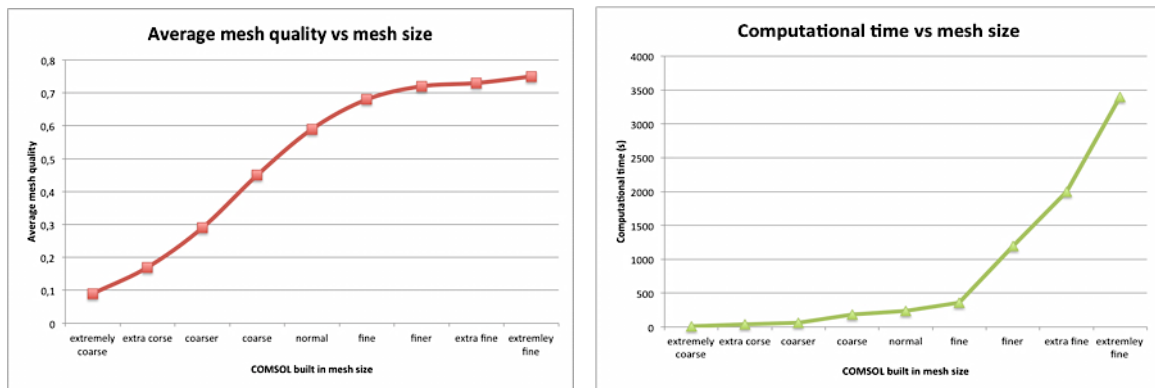
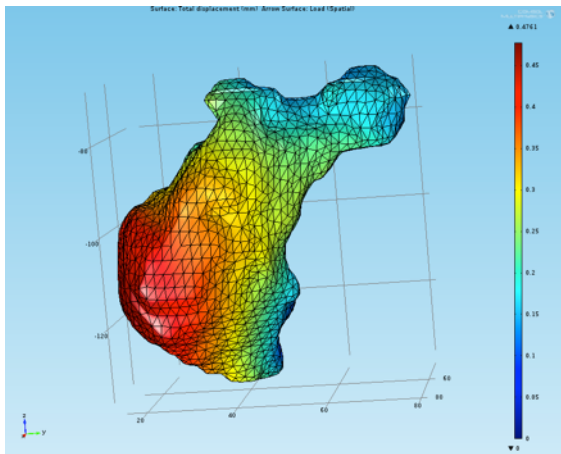
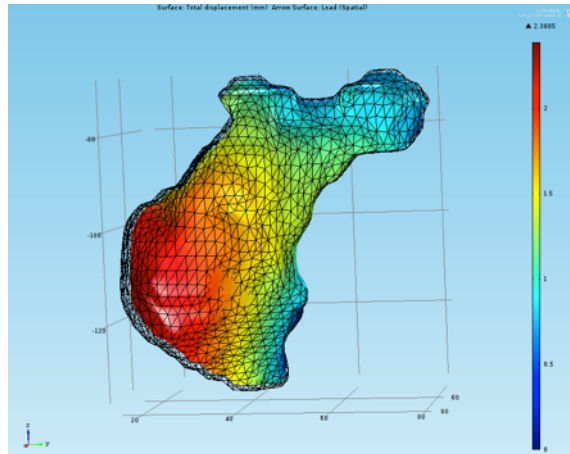


**Figure 73:** average tetrahedron mesh quality for different COMSOL® built-in mesh size single simulation computational time for different COMSOL® built-in mesh size

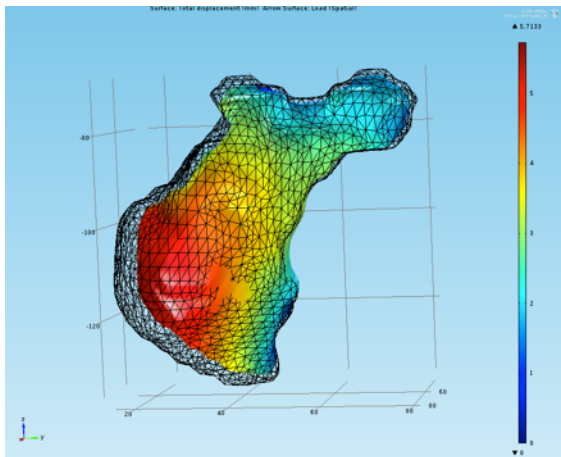
From the above plots we can see that upper fine size, an increase in mesh size yields a minimal increase in mesh quality and so in FEM accuracy results; on the other hand computational time undergoes large increase. We can conclude that the best mesh size to be used is the *fine* mesh size as the *finer* size takes more than twice as long to run a single simulation while providing only a small increase in accuracy. The assumption of a force field acting on each element along normal direction, pointing in the inner portion of the gland and fixed constraints depending on parotid duct, mandible and and vein-artery system presence seems to be correct in terms of re-producing a pattern of deformation similar to the one observed in reality as we can see comparing *fig.74* (output of FEM simulation) with real displacement map (*fig.66*). However we have to find the optimal force field intensity and Young's modulus value capable to re-produce the deformation pattern in a correct range of displacement. This goal has been reached by using a leave one out approach as described in 3.5 monitoring RMSDE (*Eq.18*) value, computed comparing pattern of deformation obtained from FEM simulation with the real one obtained from the quantitative analysis of parotid gland morphing.



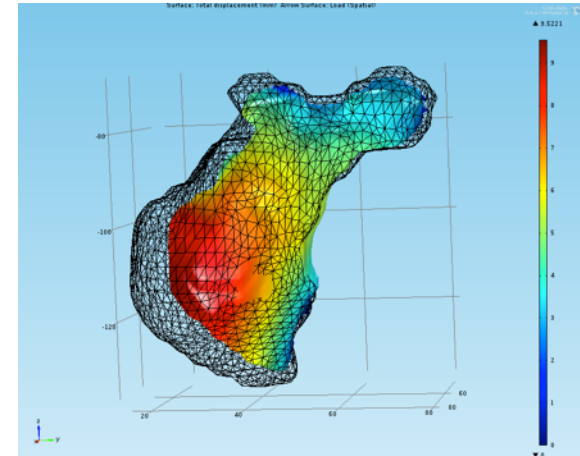
Young modulus 7000 (Pa) Force field 100 N



Young modulus 7000 (Pa) Force field 200 N



Young modulus 7000 (Pa) Force field 400 N



Young modulus 7000 (Pa) Force field 500 N

**Figure 74:** Visual representation of parotid gland deformation obtained with FEM method for different value of force field intensity and a fixed value of Young modulus (7000 Pa). Black wireframe mesh represents non deformed gland surface and coloured map represents total displacement map (mm)

FEM simulations for each patient were performed in order to represent parotid morphing in the first half of treatment duration (1- > 15-th day) and in the second half of treatment (15- > 31-st day) by using respectively as imported geometry to be morphed, parotid gland mesh at first and 15-th day of treatment. Fixed the period of treatment (1 or 2 half of treatment duration), several simulations have been performed for each patient, for all the possible combination of Young's modulus values ranging in [6000-14000] Pa interval with step of 1000 Pa, and force field ranging in [173-692] N interval with step of 86 N. At the end of each simulation post-process of results has been performed computing RMSDE between real and simulated pattern of deformation. The results of the simulations in terms of average RMSDE values computed over all 16 PGs for different value of Young's modulus and force field intensity, are reported for both period of morphing simulated (fig.75-76).

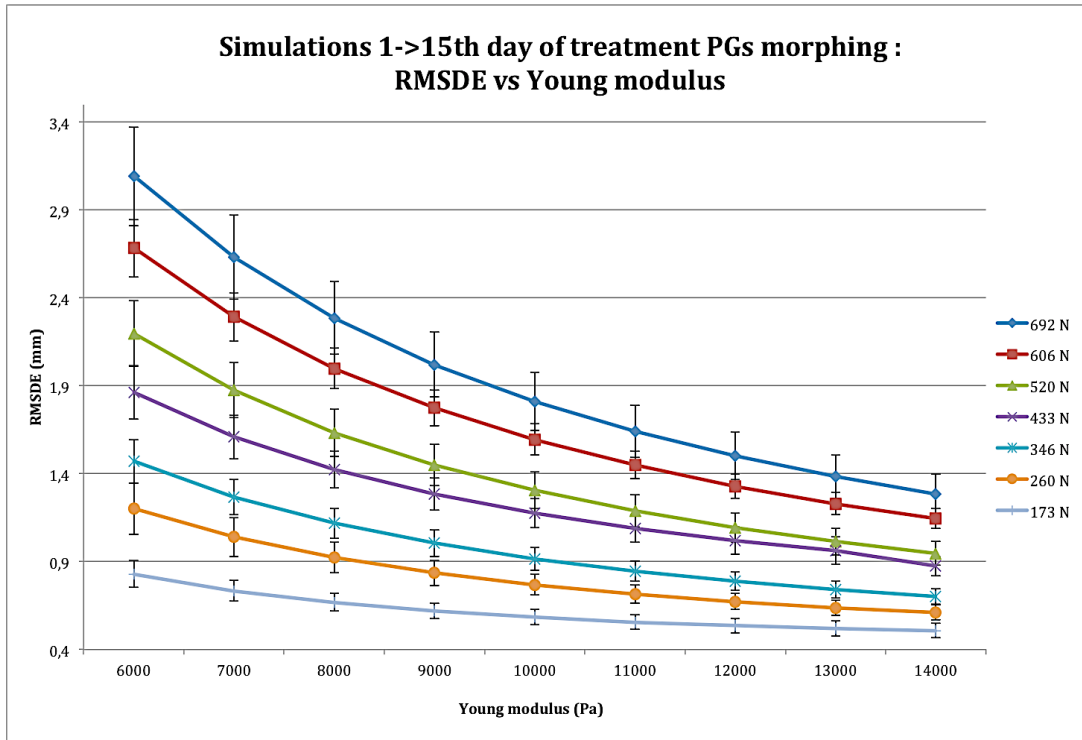


**Figure 75:** plot showing RMSDE trend obtained running FEM models with different values of soft tissue Young's modulus and force field intensity considering parotid gland morphing in in the first half of treatment duration

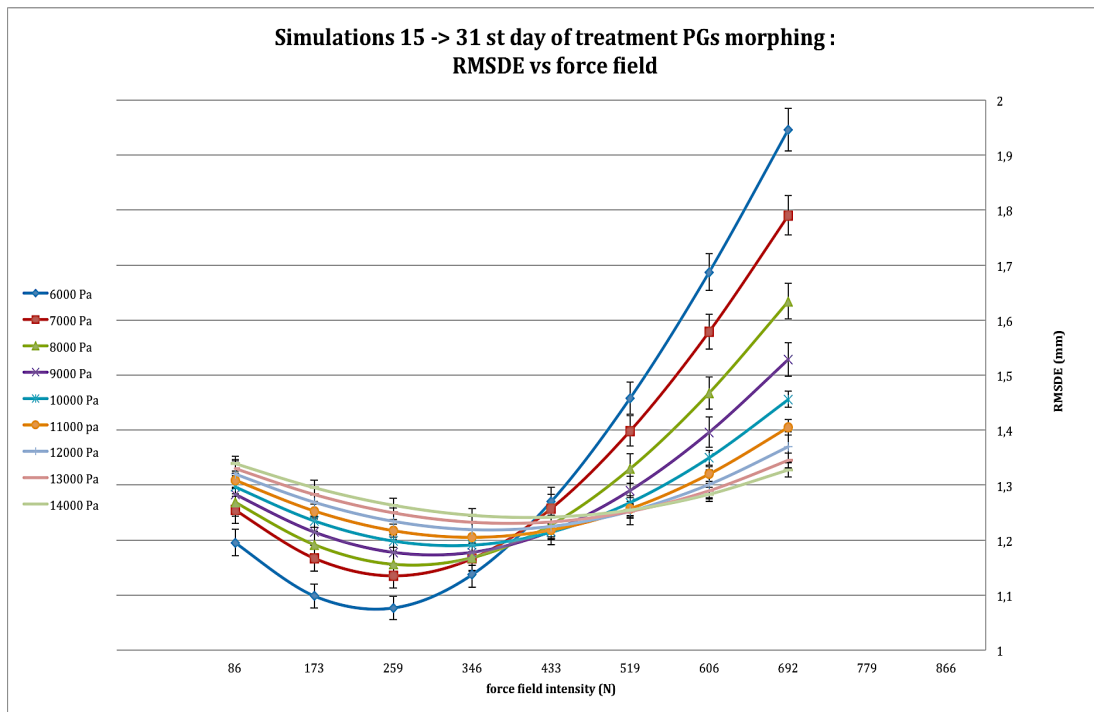


**Figure 76:** plot showing RMSDE trend obtained running FEM models with different values of soft tissue Young's modulus and force field intensity considering parotid gland morphing in the second half of treatment duration

*Figure 75* shows *RMSDE* trend for parotid gland morphing in the first half of treatment averaged for PGs of all patients. Error bars represent standard deviation values. As we can see from this plot, the best match between real and simulated PGs deformation (minimum of *RMSDE*) is reached at a force field intensity of 173 N and a Young's modulus value of 14000 Pa. Increasing force field intensity for a fixed elastic parameter, results in an increase of *RMSDE*; this is due to the fact that gradually increasing force intensity will produce a pattern of deformation gradually larger which will be more and more different from the real one observed; this effect is more pronounced for low values of elasticity in fact a low Young's modulus value belongs to a flexible material which under increasing load condition changes its shape considerably. On the contrary a stiff material has a higher Young's modulus and it changes its shape only slightly. *Figure 76* shows *RMSDE* trend for parotid gland morphing in the second half of treatment averaged over PGs of all patients. As we can see from this plot the best agreement between real and simulated PG deformation (minimum of *RMSDE*) is reached at a force field intensity of 259 N and at a Young's modulus value of 6000 Pa. Considering a single elastic parameter value, increasing or decreasing force field intensity from the condition that minimizes *RMSDE* value, results in an increase of *RMSDE*; this is due to the fact that gradually increasing or decreasing force field intensity will produce a pattern of deformation gradually different from the real one. This effect is more pronounced for low values of elasticity due to the greater flexibility of such material. From the simulation results obtained comes up that in the first half of treatment optimal correspondence between real and predicted deformation is reached modeling parotid soft tissue as a linear elastic material with Young's modulus value of 14000 Pa. On the contrary the best accordance between real and predicted deformation in the second half of treatment is reached modeling parotid soft tissue as a more flexible linear elastic material with Young's modulus of 6000 Pa; this findings agree with the fact that parotid glands in the second half of the treatment are subjected to a greater pattern of deformation with respect to the first half of treatment, therefore its modeling requires a more flexible soft tissue material and a greater force field intensity to be used.

The leave one out cross validation method produced the following optimal parameter findings for all PGs involved in our simulations:

Optimal findings	1 – 15 th day morphing	15– 31 st day morphing
Young's modulus (Pa)	14000	6000
Force field intensity (N)	173	259

*Table 13 : optimal simulation parameters*



By using the optimal parameter values (*table 13*) and performing *FEM* simulation for each parotid in the first and second half of treatment duration, it is possible to export surface mesh of the simulated deformation and quantify difference between real and predicted pattern of deformation in terms of *DICE* coefficient and volume difference (*fig.77*). To visualize the overlap obtained between real gland geometry and simulated one by using optimal parameter findings for all PGs involved in our study see Appendix 4.

1 -&gt; 15 -th day morphing

15 -&gt; 31 -st day morphing

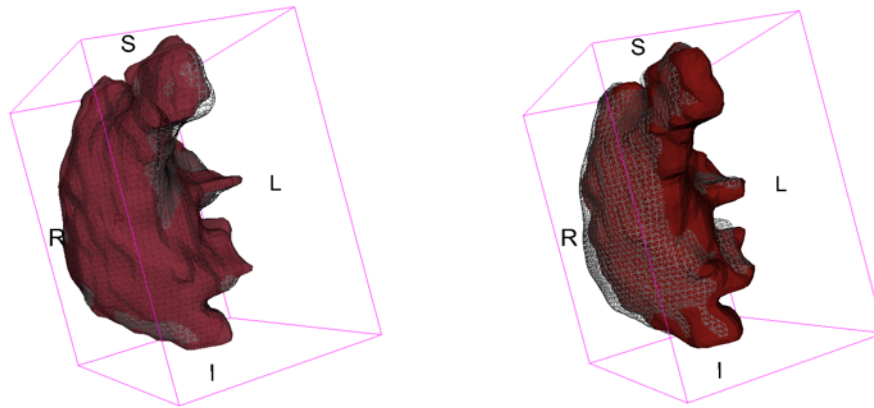


**Figure 77:** an example of the overlap between real (red surface) and simulated (grey wireframe) parotid gland deformation for both period of morphing considered obtained by using optimal findings values

As we can see from plot in *figure 78(b)* the implemented procedure is able to represent parotid gland morphing with % volume difference between real and simulated parotid deformation comparable for both morphing period considered (1->15 day treatment: mean %volume difference =1.36% min=0.9% , max=2 % 15->31 day treatment : mean %volume difference =1.5 % min=0.8% , max=2.1 % ) . On the opposing evaluating correspondence between real and predicted deformation in terms of *DICE* coefficient (*fig.78(a)*) results in worst performance for the second half of treatment ( 15->31 day treatment mean *DICE* =0.64 unit ) respect to the first half where a good correspondence is reached ( 1->15 day treatment mean *DICE* =0.9 unit) . As the *DICE* coefficient gives us information on the overlap between geometries compared, the results obtained in the second half of the treatment indicate an inability to correctly predict the position of the deformed gland geometry although its reduction in volume has been correctly predicted . Even in terms of *RMSDE* the agreement between real pattern of deformation and simulated one in the second half of the treatment reaches a worst result with respect to gland morphing simulated in the first half of treatment.

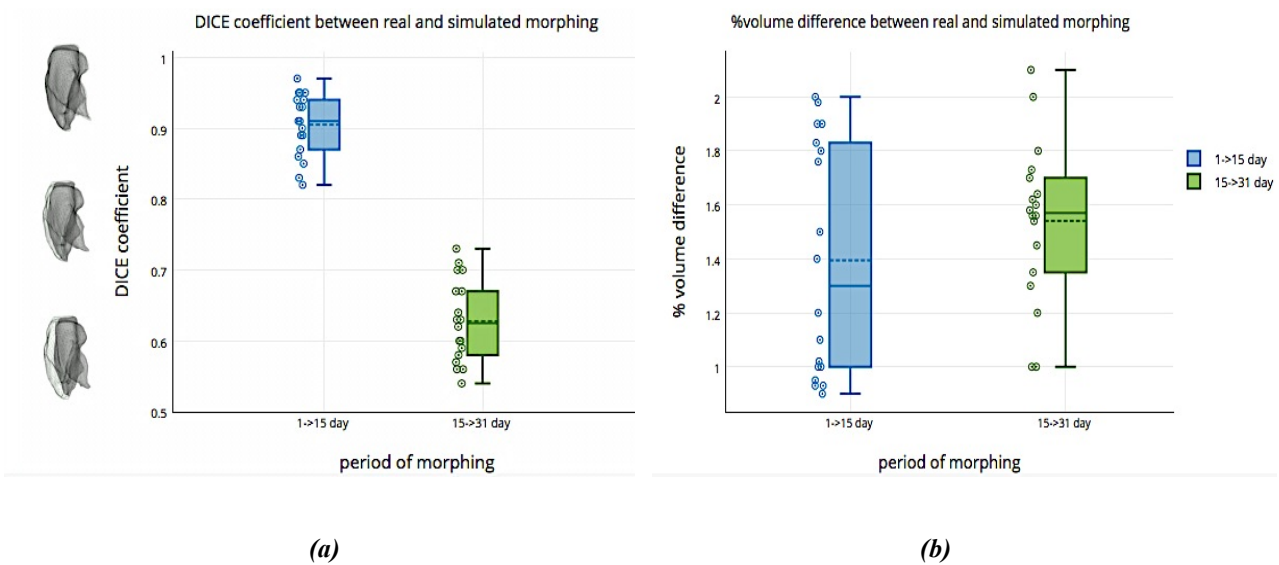


**Figure 78** : (a) box plot that shows DICE coefficient computed between real and simulated parotid gland deformation for both morphing period considered and (b) box plot that shows % volume difference computed between real and simulated parotid gland deformation for both morphing period considered

These results can be attributed to an effect that appears in the second half of treatment and that we have not considered in the model: patient's facial slimming process. It is reasonable in fact that the effect of the facial slimming becomes particularly evident towards the end of the treatment as we can see from *figure 79*. We can consider that the loss of facial fat and muscle mass and tumour shrinkage lead to a compression of the glands towards the centre of the oral cavity exerted by the surrounding facial structures that shrink; we can introduce this effect in our model through an additional force field acting only on the posteromedial region of the gland in the neck direction and consider as fixed constraints only the retro mandibular branch touching the gland. The first results of the simulations performed by using these assumptions are able to produce a pattern of deformation similar to the one observed in the real case (*fig. 80*).

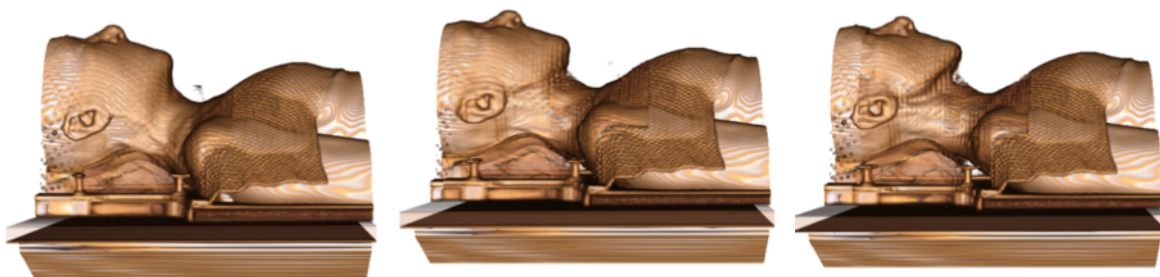


**Figure 79**: 3D surface reconstruction obtained using 3D Slicer muscle mass volume rendering filter showing patient progressive facial slimming ( 1-st day of treatment, 15-th day of treatment, 31-st day of treatment).

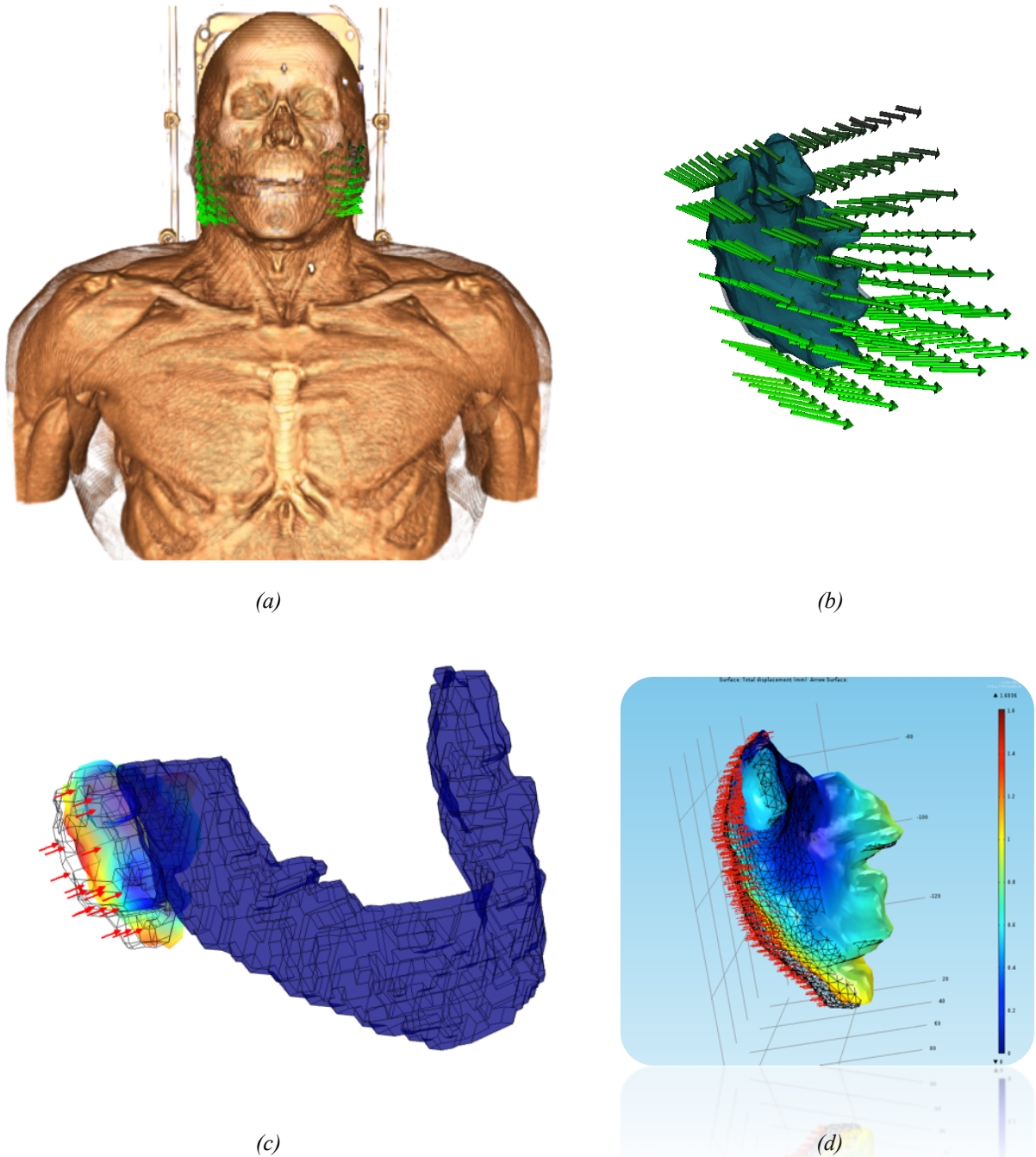


**Figure 80** : (a) 3D surface reconstruction of patient anatomy with displacement vector field necessary to align our simulated deformed mesh at the end of treatment with the real one with a zoom on right PG (b). First COMSOL simulations performed considering facial slimming process as force field acting on lateral and posterior-medial region with mandible as fixed constrained (c-d)

## 5. FUTURE CHALLENGES

Our biomechanical model, designed to deal with the challenge of 3D parotid morphing modeling and prediction in *RT* treatment, could be improved in the future in such ways :

1. Automatize interaction between softwares and improve computational resources in order to model weekly or daily parotid morphing process.
2. Perform studies in order to quantify how *FEM* elastic parameter values and material model match with the real elastic properties of patients' gland :
  - a. Acquire share-wave elastograph images of the gland .
  - b. Perform stress test on parotid gland tissue .
3. Enlarge the cohort of patients in order to study the correlation between optimal *FEM* force field intensity and dose delivered to glands.
4. Model patient face slimming and tumour shrinkage by monitoring facial shrinkage process and introduce into the model the interaction between muscle mass ,vein ,artery and parotid duct obtained from MRI images.
5. Develop a COMSOL<sup>®</sup> app that any user could run in order to obtain user friendly and interactive simulation of PGs morphing that could be used into a TPS software.
6. Implement statistical model of gland shape deformation in order to obtain a statistical knowledge about 3D pattern of deformation that could be used to define force field used in the *FEM* simulation.

First steps of statistical shaped based model have been already implemented by using a Matlab<sup>®</sup> homemade program (see Appendix5) involving PGs of five patients.

It utilizes the principal modes of co-variation between anatomy and deformation in order to statistically forecast organ warping . The main challenge of the statistical shape based approach is the point correspondence problem in the model construction phase: on every training sample for the model, landmarks have to be placed in a consistent manner.

The SPHARM-PDM approach, used in several studies of brain morphometry [38], has been successfully employed in our 3D shape modeling problem to reach this goal. It is a method based on a parametric description using spherical harmonics (SPHARM) of 3D point distribution (PDM). The input of SPHARM-PDM algorithm is a set of binary segmentation of a single structure, the parotid gland in our case. This segmentation is first processed to fill any interior holes and a minimal smoothing operation is performed. The binary segmentations are converted

to surface meshes and a spherical parameterization is computed for the surface meshes by using an area preserving, distortion minimizing spherical mapping.

Using a uniform icosahedron-subdivision of the spherical parameterization, we obtain a Point Distribution Model (PDM). Correspondence of SPHARM-PDM representation of the different parotids is determined by normalizing the alignment of the spherical parameterization to an object-specific frame. After this normalization, correspondence between surface points across different objects is reached. SPHARM-PDM approach has been applied to 12 parotids of our training sample by using dedicated 3D Slicer toolbox (*fig.81*).

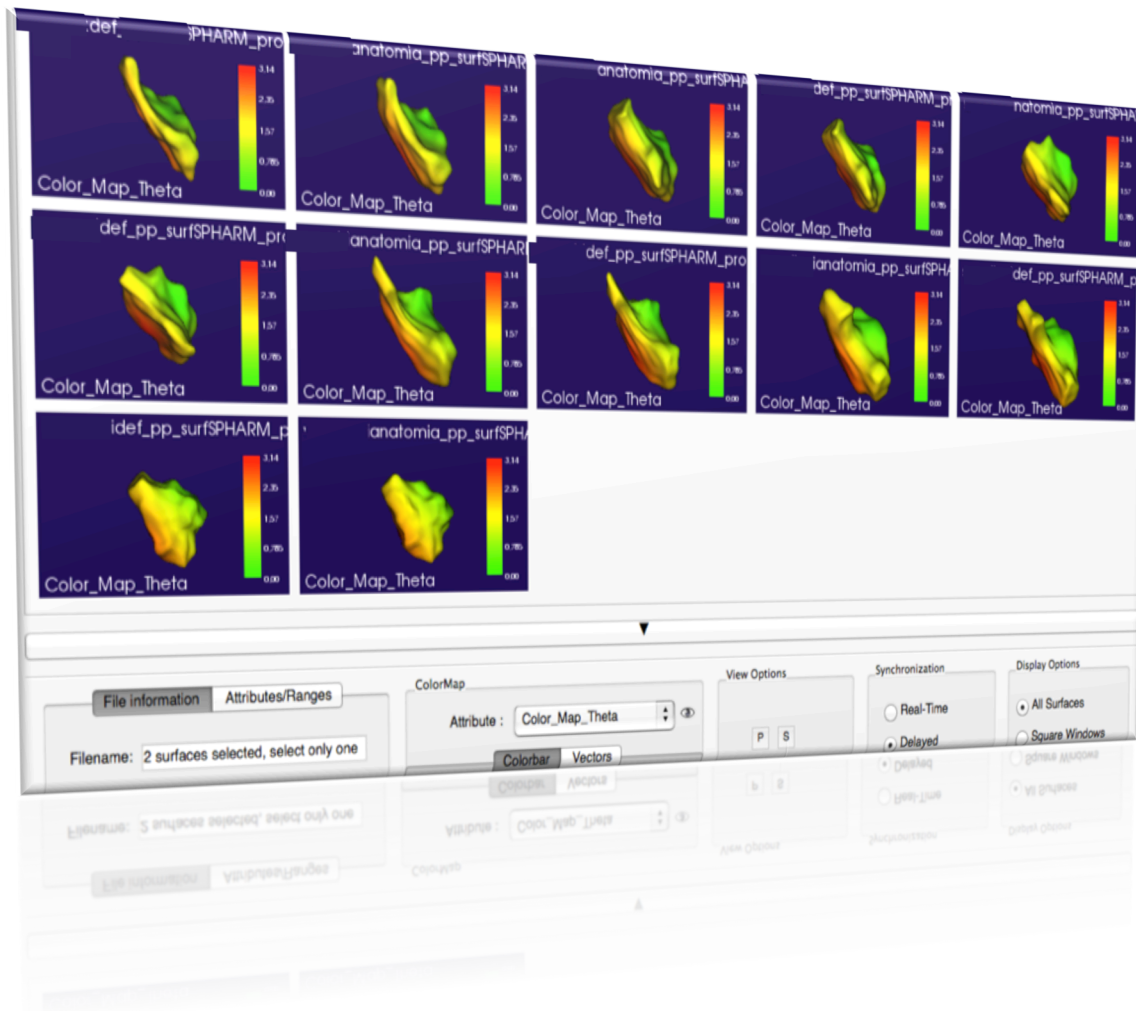


**Figure 81** : 3D Slicer output for SPHARM-PDM algorithm implementation over 12 parotids (6 gland at start of treatment named anatomy and 6 correspondent deformation at the end of treatment). Coloured map represent theta value coordinates of the spherical parametrization; regions with the same colour among different surfaces represent correspondent areas

Once the point correspondence problem has been overcome it is possible to represent each parotid gland at the start of treatment as a collection of points (landmarks) arranged in a vector  $s$  to which corresponds a vector  $q$  representing displacement vectors at the end of treatment defined on their respective landmark. Applying principal component analysis (*PCA*) to the training data and via an optimization procedure, when presented with a new shape, which corresponds to the geometry of the gland at the start of treatment, its deformation can be predicted (Appendix 5).

In order to test the predictive power of the statistical framework in estimating anatomical deformation of parotid gland between the first and the last day of treatment, we used the leave-one-out cross validation method. In particular, we selected one training sample and used the remaining to train the predictive model and each time we calculated the estimation error expressed in terms of *DICE* coefficient between the mesh of the true and predicted deformed parotid mesh.

The average estimation error computed over five training samples is 0.86 DICE unit (0.9 max - 0.84 min). On-going work focuses on including the knowledge about the deforming anatomy obtained with this statistical method assessing the principal modes of co-variation between shape and forces so that it can be implemented in conjunction with the finite element analysis software.

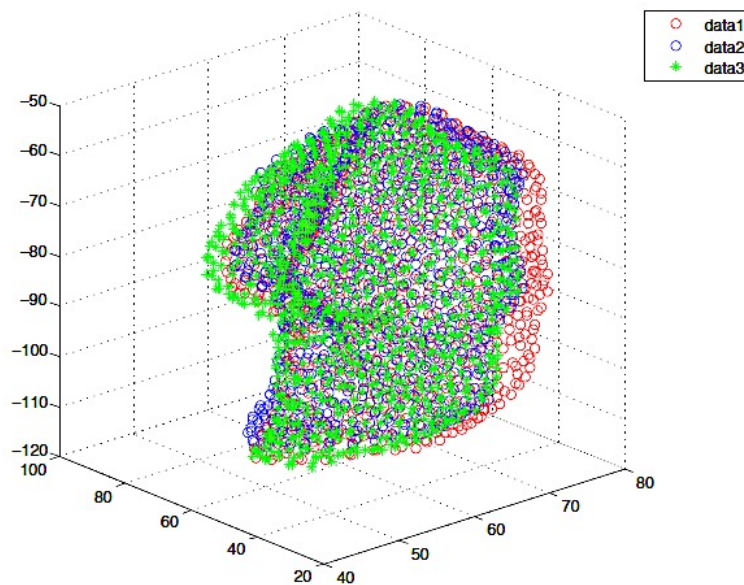


**Figure 82** : Matlab output for the implemented statistical shape model. Red points represent parotid gland anatomy at the start of treatment, blue points represent real pattern of deformation at the end of treatment, green points represent prediction of gland deformation obtained using PCA and considering the current patient as leave out patient of our sample

## 6. CONCLUSIONS

This thesis work proposes an innovative approach in the field of the modeling and prediction of parotid gland deformation in head and neck patients via *FEM* biomechanical model implementation; unlike classical *FEM* biomechanical model of organ deformation proposed in literature, where force field responsible of organ warping is known (as due to the action of bistoury or an external object exerting some known load condition) in our approach some hypothesis have been made to include into the model several different unknown effects that cause parotid change in shape such as loss of acinar cells due to exposure to ionizing radiation .

Definition of model boundary condition represented a challenge task due to the complexity of parotid gland anatomical relations with surrounding structures, so same simplification has been made introducing tubular structures as fixed constraints to mimic parotid duct, vein, artery and muscle presence.

The *FEM* software COMSOL<sup>®</sup> commonly used for structural mechanics studies, has been successfully used to address the problem of modeling gland soft tissues as a linear elastic material and to study its deformation under different load and boundary conditions. The implementation of our *FEM* model has required an initial phase consisting in the creation of parotid gland 3D geometry. This goal has been reached combining use of RayStation<sup>®</sup> and 3D Slicer<sup>®</sup> softwares: the first due to a scripting procedure is able to automatic re-contour parotid glands on daily MVCT images then used by 3D Slicer<sup>®</sup> to create organ surface mesh. Once parotid mesh for all patients involved in our study have been realized *FEM* model implementation started.

The *FEM* model has been implemented to reproduce parotid slimming process in two period of morphing (*1->15-th day* and *15->31-st day* of treatment duration). In order to find optimal load condition and elastic parameter able to produce patterns of deformation that match with the real ones observed, different simulations have been performed. Based on *RMSDE* metric minimization, optimal parameter value obtained are: Young's modulus of 14kPa and 173 N force field intensity for the *1->15-th day* period of morphing, Young's modulus of 6kPa and 259 N force field intensity for the *15->31-st day* period of morphing.

By using optimal parameter values, the implemented procedure is able to represent parotid slimming process with a mean volume difference with respect to real pattern of deformation of 1.4 % [*max 2% –min 0.75%*] for *1->15-th day* of treatment period and 1.5% [*max 2,2%–min 1%*]

---

for 15->31-st day of treatment period. On the opposing evaluating the agreement between real and predicted deformation in terms of *DICE* coefficient results in worst performance for the second half of treatment (15->31-st day treatment mean *DICE* =0.64 unit [max 0.74–min 0.56]) compared to the first half where a good correspondence is reached (1->15-th day treatment mean *DICE* = 0.9 unit [max 0.97–min 0.83] ).

From this results comes up that an additional effect has to be considered in our model in order to obtain a good overlap between real and simulated deformation: patient face slimming . This effect could be introduced into the model as force field acting on PGs posteromedial region in the neck direction with retro mandibular branch as fixed constraints.

Due to the availability of PGs surfaces for the whole treatment duration, quantitative analysis of parotid morphing process has been performed. From our results come up that PGs are subjected to a shrinkage process characterized by volume reduction rate with respect treatment start of 1%/day (Left PGs.) and 0.8%/day (Right PGs.). Parotid shrinkage process has also be investigated in terms of *DICE* coefficient and surface reduction compared with treatment start , obtaining results in agreement with a progressive shrinkage process of the whole gland (daily rate of surface reduction 0.5%/day, daily rate of *DICE index* reduction 0.008 unit/day ). Furthermore distance map between daily gland surfaces and its initial geometry have been analysed in order to investigate about the location of the region interested by the greatest pattern of deformation. From our analysis comes up that posterior-medial region is the one, which deforms the most, and its change in shape becomes particularly evident starting from the 3-th week of *RT* treatment.

Although our workflow has been designed to handle the challenge of modeling PGs morphing process in *H&N* patients, in theory it can be used to represent organ deformation of any *RT* structures of interest just changing load and boundary condition in order to match with the specific different morphing process considered. Even thought the implemented method is quite efficient we hope in the future to improve the limitations that emerged during model construction phase in order to represent daily parotid morphing process in such a way that it can be used by an off line *ART* protocol to reduce dose delivery to these structures.



## APPENDIX 1

### MATHS OF FEM

Consider the following Dirichlet boundary value problem defined in two-dimensional space :

$$u_{xx}(x, y) + u_{yy}(x, y) = f(x, y) \text{ in } \Omega \quad (Eq.19)$$

$$u = 0 \text{ on } \partial\Omega$$

where  $\Omega$  is a connected open region in the  $(x, y)$  plane whose boundary  $\partial\Omega$  is smooth, and  $u_{xx}$  and  $u_{yy}$  denote the second derivatives with respect to  $x$  and  $y$ , respectively. This is the steady state heat transfer equation. The following steps are used to solve the boundary value problem using *FEM* method: 1) formulating the problem as in variational form, 2) discretization of the continuous domain, 3) choosing a basis functions, 4) deriving the numerical matrix expression of the equilibrium equations for all elements , 5) assembling them into a global matrix equation and solving the derived matrix equation.

#### 1) Variational formulation

Let a function  $v$  named *test function* be a function in the *Hilbert space*  $H_0^1(\Omega)$  consisting of functions which are differentiable and have zero values on the boundary  $\partial\Omega$  as a subset of the domain  $\Omega$ . Multiplying the function  $v$  to both sides of the Dirichlet equation and integrating by parts using a form of *Green's identities*, results in:.

$$\int_{\Omega} f v dx dy = - \int_{\Omega} \nabla u \cdot \nabla v dx dy = -\phi(u, v) \quad (Eq.20)$$

The weak formulation, or variational formulation, of *Eq.19* is obtained by requiring this equality (*Eq.20*) to hold for all test functions in the *Hilbert space*. It is called “*weak*” because it relaxes the requirement of *Eq.19*, where all the terms of the *PDE* must be well defined in all points. The relations in *Eq.20* instead only requires equality in an integral sense. It is possible to show that the weak formulation, together with boundary conditions, is directly related to the solution from the pointwise formulation and for cases where the solution is differentiable enough (i.e., when second derivatives are well defined), these solutions are the same.

With the weak formulation, it is possible to discretize the mathematical model equations to obtain the numerical model equations.

### 2) Domain discretization

Suppose to divide the domain with triangular grid. The basic idea is to replace the continuous form of the Dirichlet boundary value problem with a discretized form to find the solution  $u$  in a space  $V$  of functions which are linear on each subdivision of the domain as shown in *figure 83* where the space  $V$  consists of functions which are linear on each triangle. The triangular grid can be finer and finer so that the solution of the discrete problem can be more approximate to the real solution. Although different types of elements are allowed for one volume, normally one single type of elements is used.

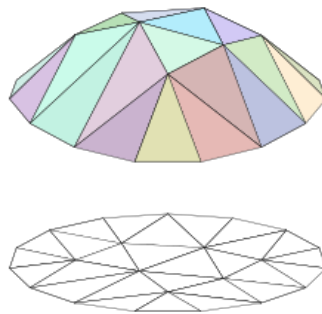


**Figure 83:** Piecewise linear solution function  $u$  on subdivisions of a discretized domain

### 3) Choise of basis

The domain discretization implies looking for an approximate solution to *Eq. 20* in a finite-dimensional subspace of the *Hilbert* space. For two-dimensional domain reported in this example, one basis function per vertex of the triangulation of the planar region  $\Omega$  is chosen. The basis function is a unique function of  $V$  with value 1 at one vertex and zero at other vertices of a triangular element. The basis function is zero on any other triangular regions. The inner product of any two different basis functions is zero. So, these basis functions are linear independent in the function space  $H_0^1(\Omega)$ . Let  $\{v_k\}_{1 \leq k \leq n}$  be the basis functions. The solution  $u$  and the function  $f$  can thus be expressed as a linear combination of the basis functions:

$$u = \sum_{k=1}^n u_k v_k \quad (Eq.21)$$

$$f = \sum_{k=1}^n f_k v_k \quad (Eq.22)$$

Therefore, substituting Eq.21 and Eq.22 in Eq.20 the Dirichlet boundary value problem can be written as:

$$-\sum_{k=1}^n u_k \phi(v_k, v_j) = \sum_{k=1}^n f_k \int_{\Omega} v_k v_j dx dy \quad \text{for } j = 1, \dots, n \quad (Eq.23)$$

Once the basis functions have been determined, all values within an element can be interpolated.

#### 4) Assembling the element equations

To find the responses of the overall system modeled by the network of triangular elements, all the element equations must be assembled to form the global system matrix equation expressing the behavior of the entire system. The global system matrix is often referred to as the *stiffness matrix*, harkening back to the finite element method's first application as well as its use in structural mechanics. The basis for the assembly procedure stems from the fact that at a node, where elements are interconnected, the value of the field variable is the same for each element sharing that node. From the derived expression (Eq.21) (Eq.22) using the basis functions, the unknown column vectors  $(u_1, \dots, u_n)^t$  and  $(f_1, \dots, f_n)^t$  are denoted by  $\mathbf{u}$  and  $\mathbf{f}$ . Then the global stiffness matrix equation yields :

$$-L\mathbf{u} = M\mathbf{f} \quad (Eq.24)$$

where

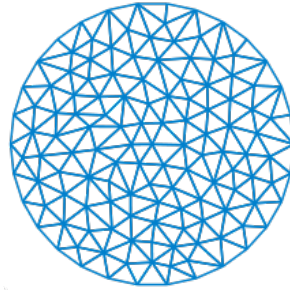
$$L = (L_{ij}) = \phi(v_i, v_j) \text{ and } M = (M_{ij}) = \int_{\Omega} v_i v_j dx dy \quad (Eq.25)$$

#### 5) Imposing the boundary conditions and solving the global system equation

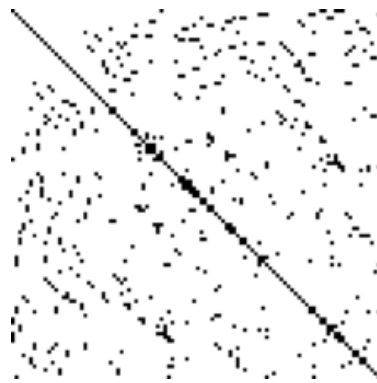
Before solving the global system equation, it is needed to impose the known boundary conditions such as known nodal values or force loads on known nodes. These conditions can be changed based on the real physical environment and the prior known information.

The matrices  $L$  and  $M$  in Equation 24 are called sparse matrices due to the fact that most entries in these two matrices are zero. If these matrices are not large, it is easy to invert the matrix  $L$ .

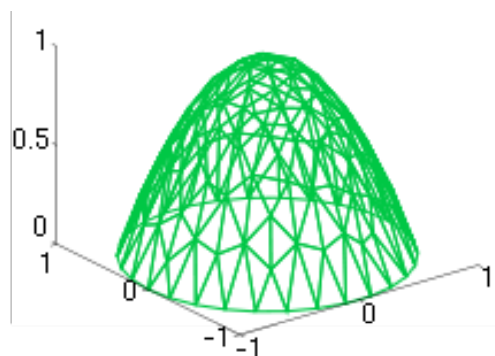
However in three-dimensional space, a fine mesh of a solid may have millions of vertices. So, efficient computing techniques are needed to find the solution instead of inverting the matrix  $L$  such as the conjugate gradient method an iterative technique currently used in most *FEM* softwares. Such method solves large systems faster compared to the direct method.



(a)



(b)



(c)

**Figure 84** :Solving the two-dimensional problem  $u_{xx}(x,y) + u_{yy}(x,y) = -4$  in the disk centered at the origin of  $(x,y)$  plane with a radius 1 and with zero boundary conditions: (a) The triangulation, (b) the sparse matrix  $L$  of the discretized linear system, (c) the computed solution  $u(x,y) = 1 - x^2 - y^2$

---

## APPENDIX 2

### SLICER PYTHON SCRIPT

We report the Python script to run into 3D Slicer Python interactor window in order to convert the contour representation of the loaded structures of interest into model.

```
#convert contourn structure into model

allContours = slicer.util.getNodes('vtkMRMLContourNode*')
organs = allContours.keys()
a = organs
b = ['CT']
y= [sa for sa in a if any(sb in sa for sb in b)]
for structure in y : structure
o = raw_input('Insert name of the structure you want to convert into model:')
o=[o]
z=[sa for sa in a if any(so in sa for so in o)]
for i in z :
contour = getNode(i);
surface = contour.GetClosedSurfacePolyData();
surfaceCopy=vtk.vtkPolyData();
surfaceCopy.DeepCopy(surface);
surfaceCopy.GetNumberOfPoints();
modelNode=slicer.vtkMRMLModelNode();
modelNode.SetName(contour.GetStructureName());
modelNode = slicer.mrmlScene.AddNode(modelNode);
polyDataProducer=vtk.vtkTrivialProducer();
polyDataProducer.SetOutput(surfaceCopy);
modelNode.SetPolyDataConnection(polyDataProducer.GetOutputPort());
displayNode=slicer.vtkMRMLModelDisplayNode();
slicer.mrmlScene.AddNode(displayNode);
displayNode.VisibilityOn();
modelNode.SetAndObservedDisplayNodeID(displayNode.GetID());
```

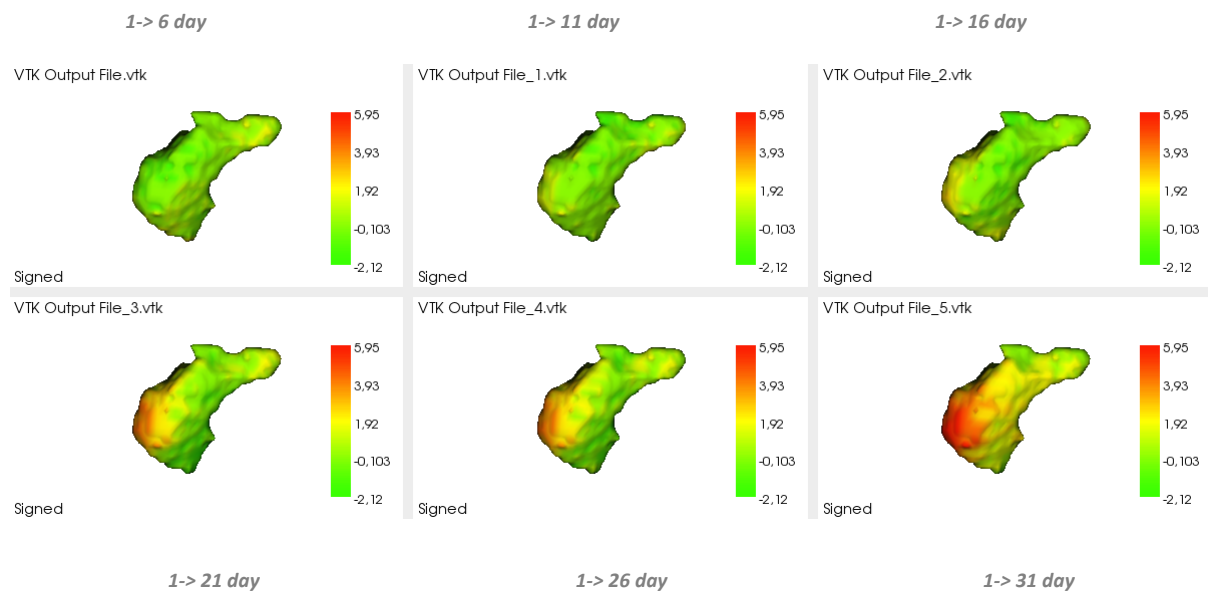
## APPENDIX 3

### DISPLACEMENT MAPS

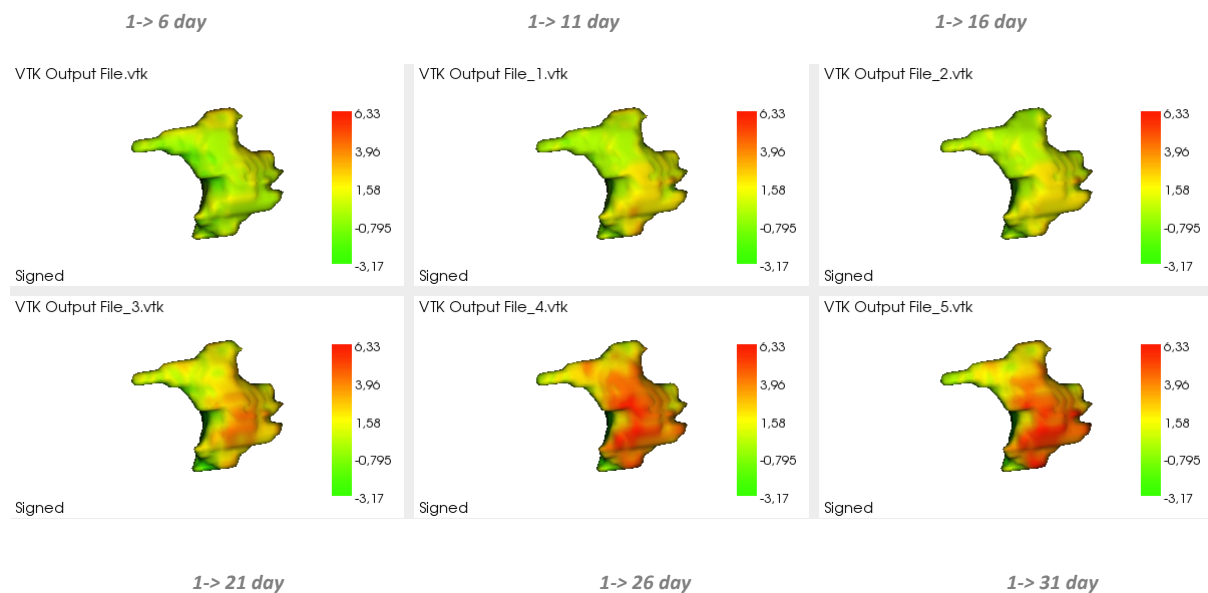
This appendix contains displacement maps (values expressed in terms of *mm*) created for all the 16 parotid glands of our sample in order to monitor the shrinkage process during treatment course with respect to the start.

#### #Patient 1

##### RightPG

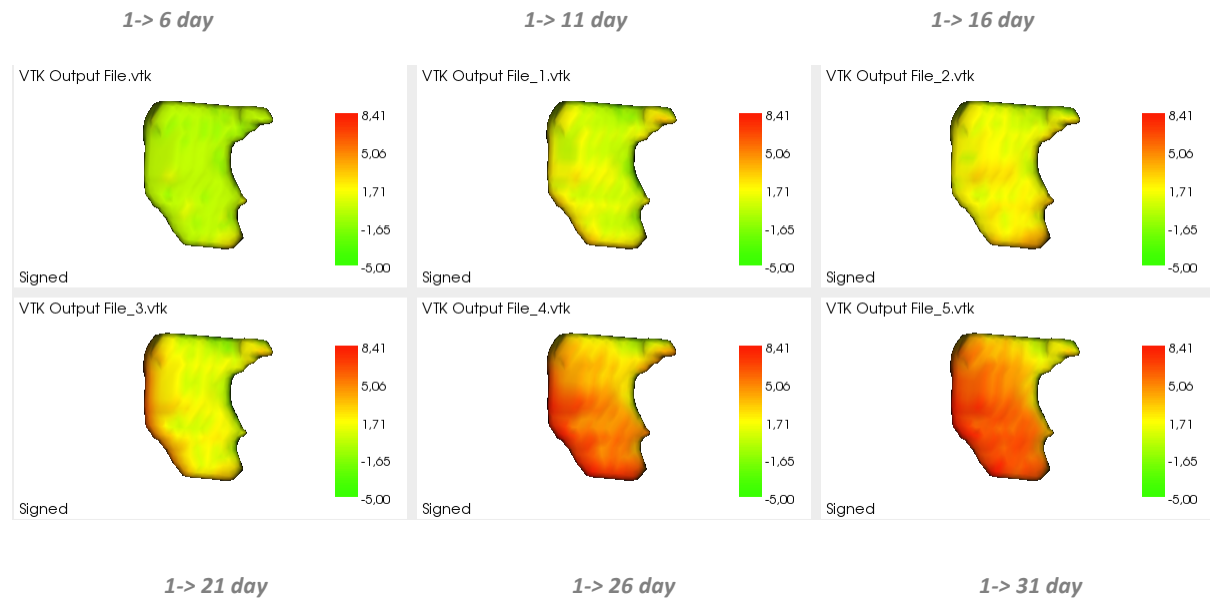


##### Left PG

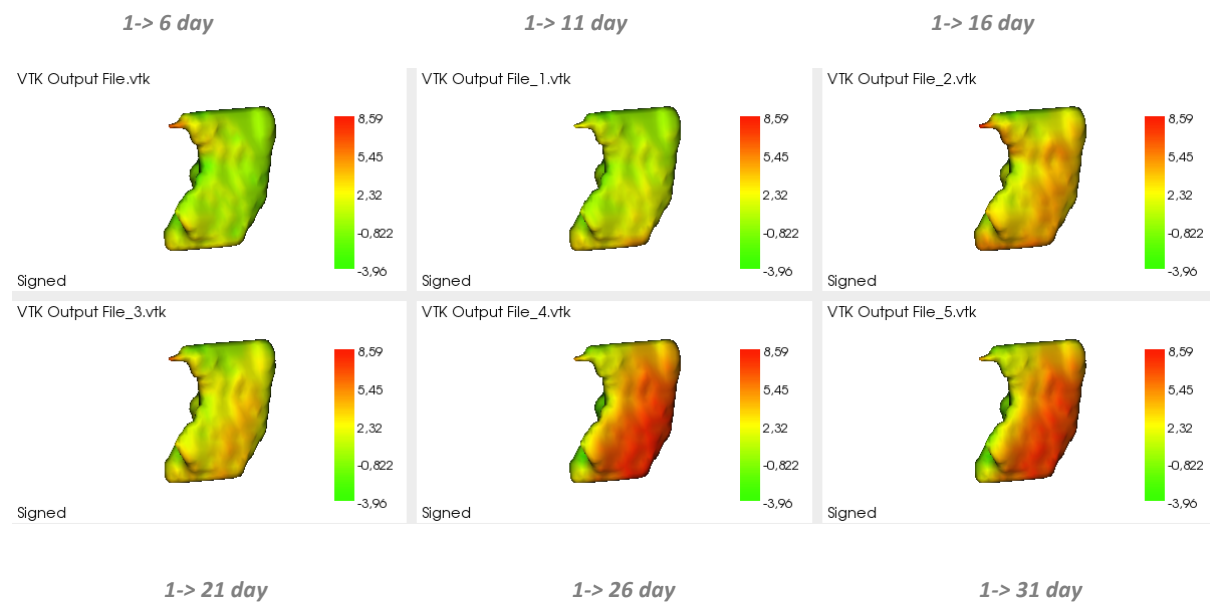


**#Patient 2**

**Right PG**

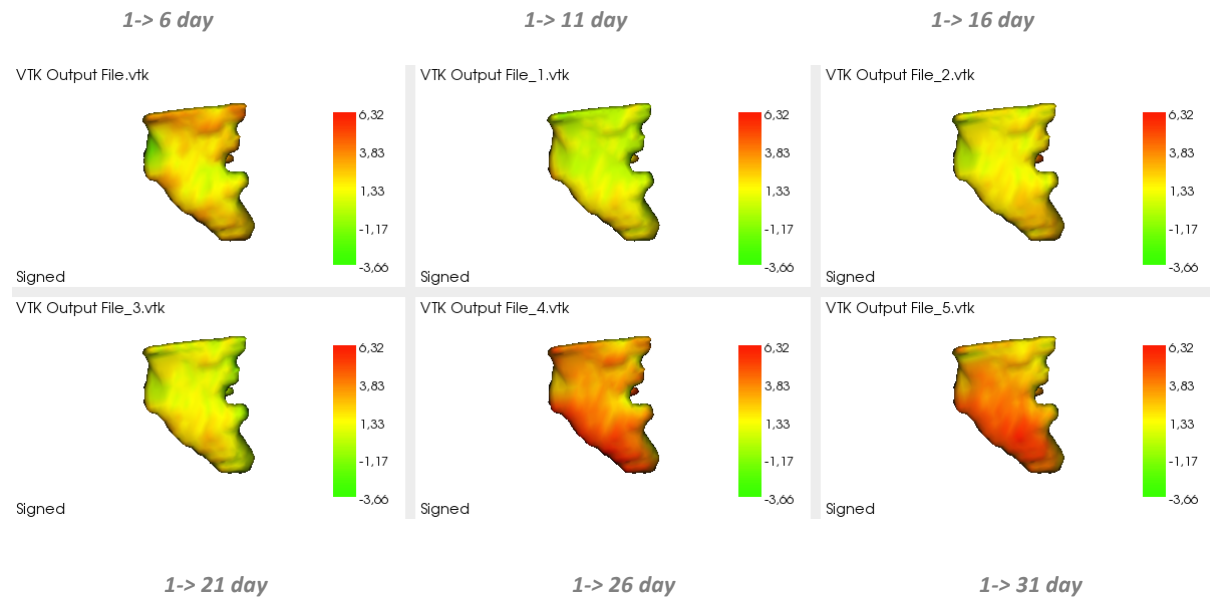


**Left PG**

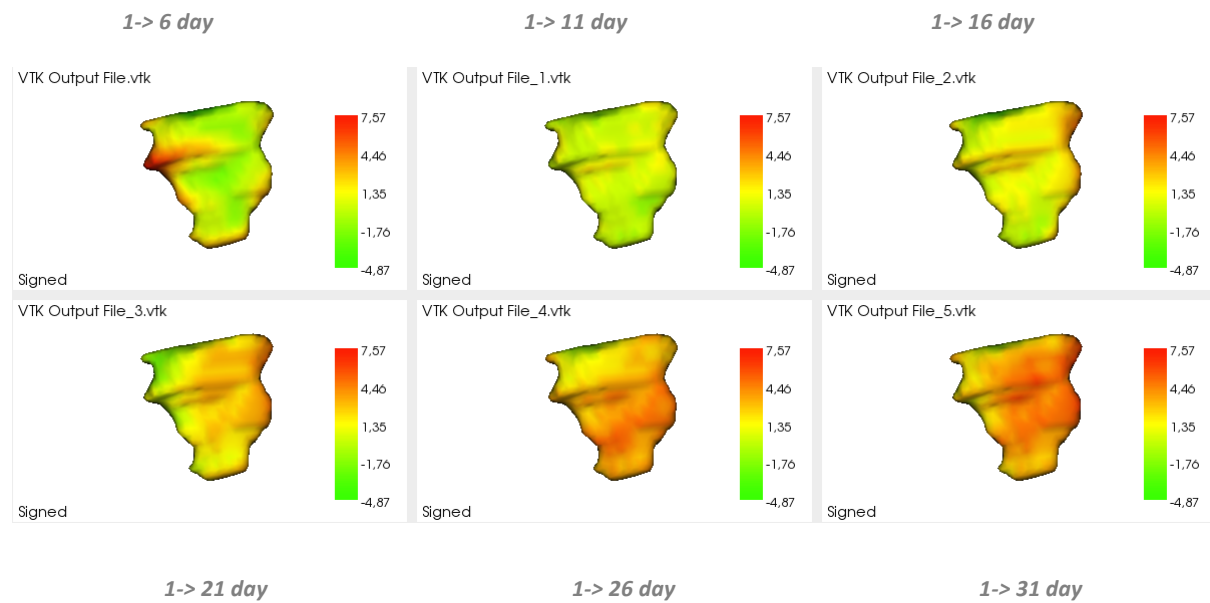


**#Patient 3**

**Right PG**



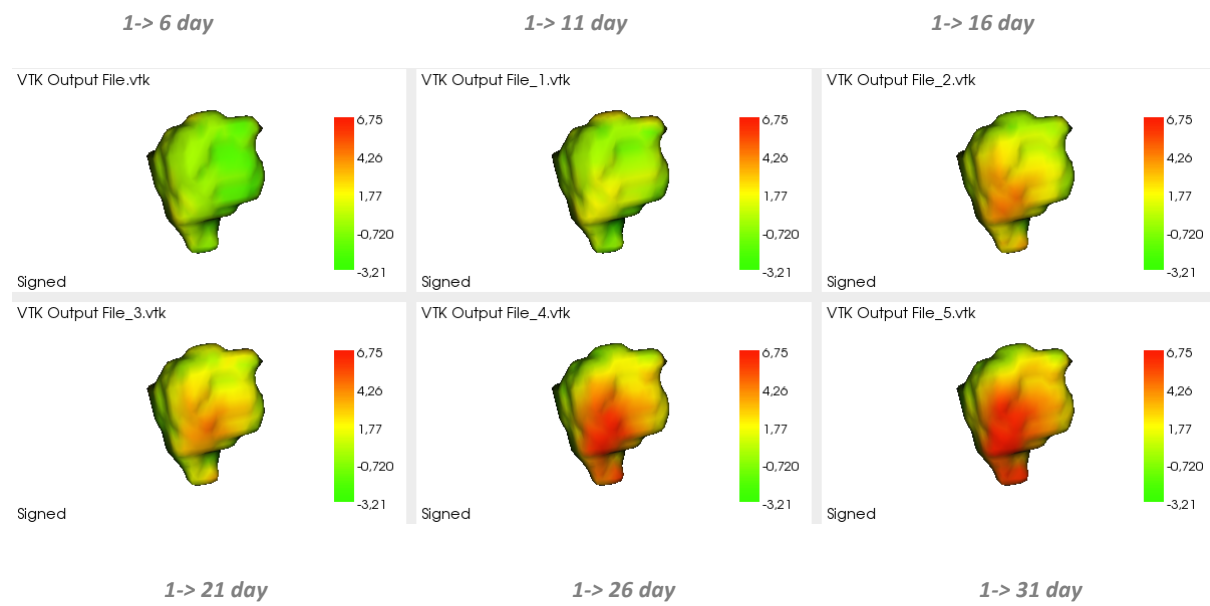
**Left PG**



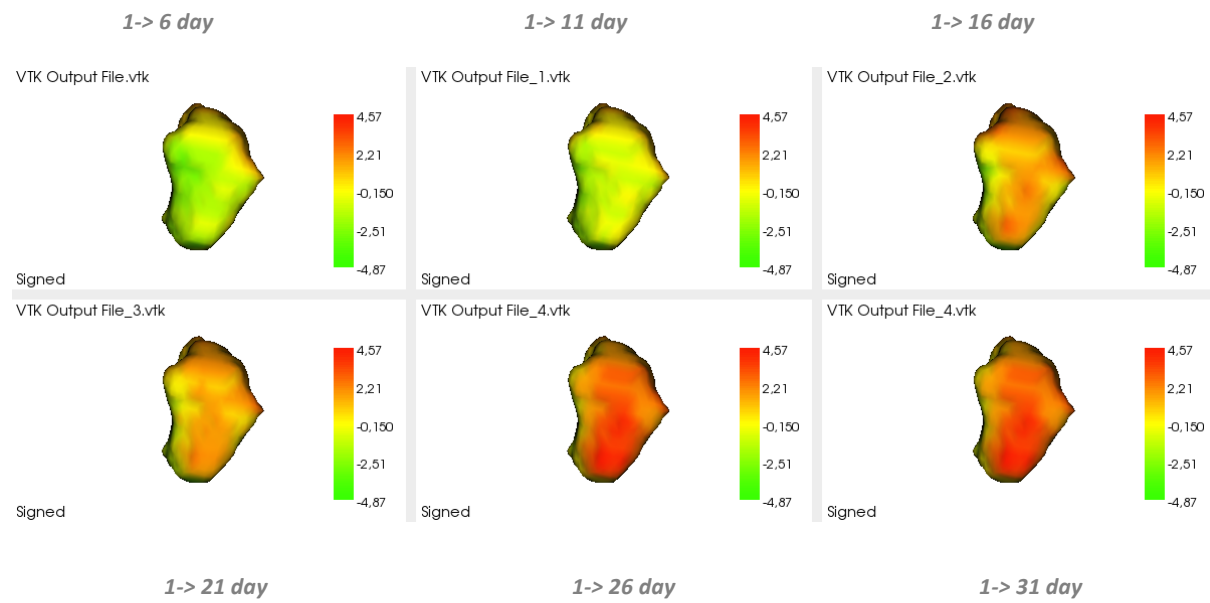


**#Patient 4**

**Right PG**

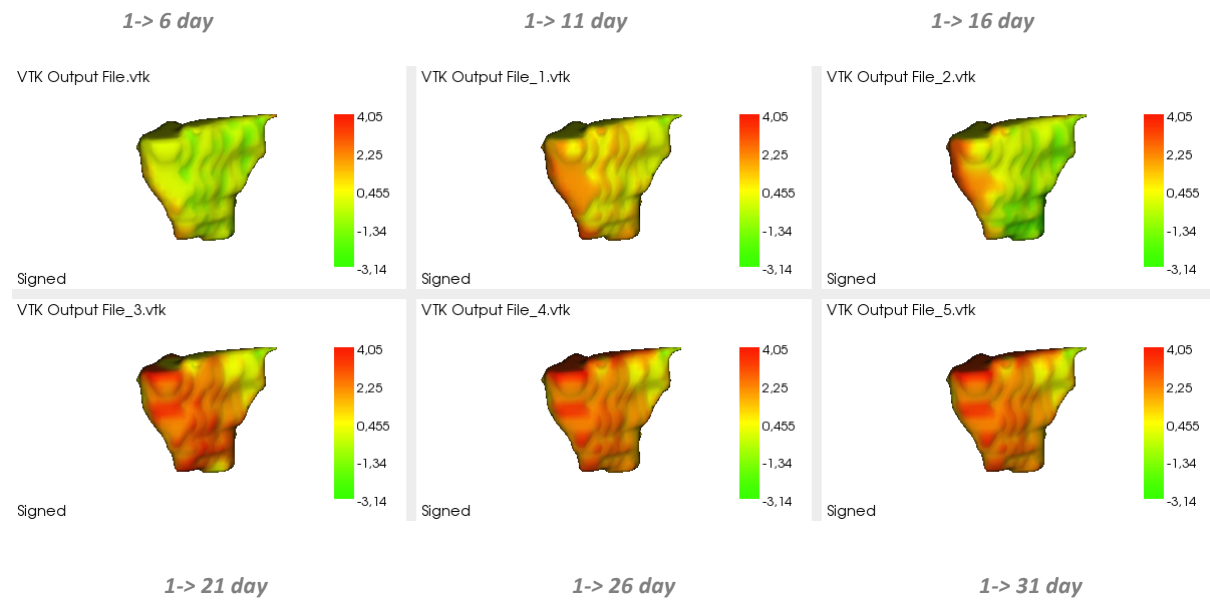


**Left PG**

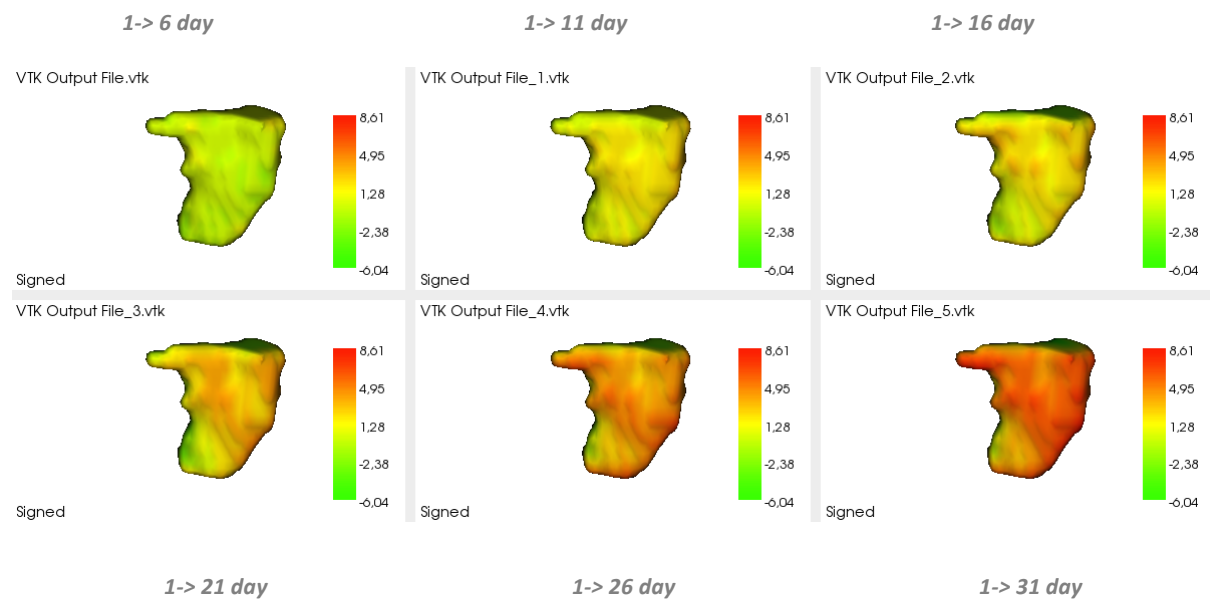


**#Patient 5**

**Right PG**

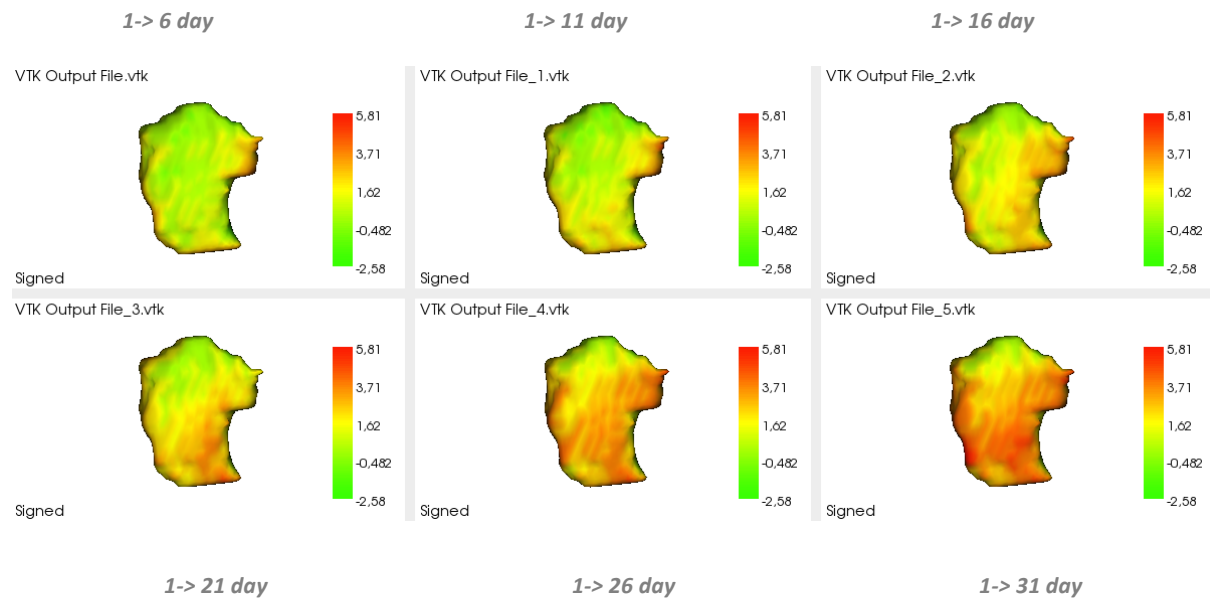


**Left PG**

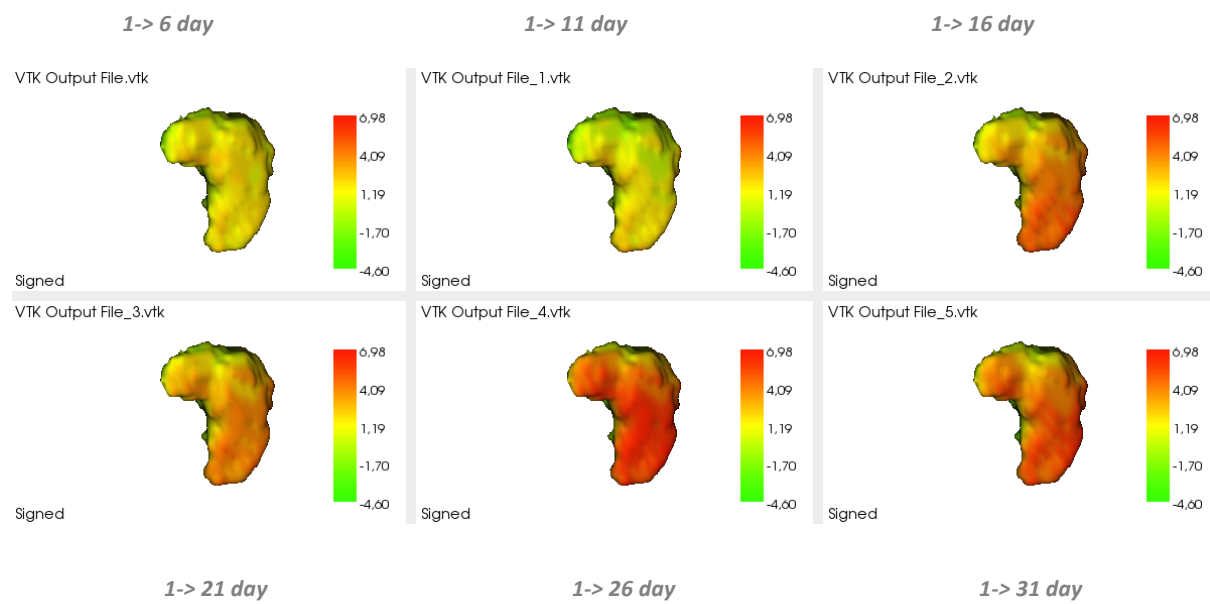


**#Patient 6**

**Right PG**

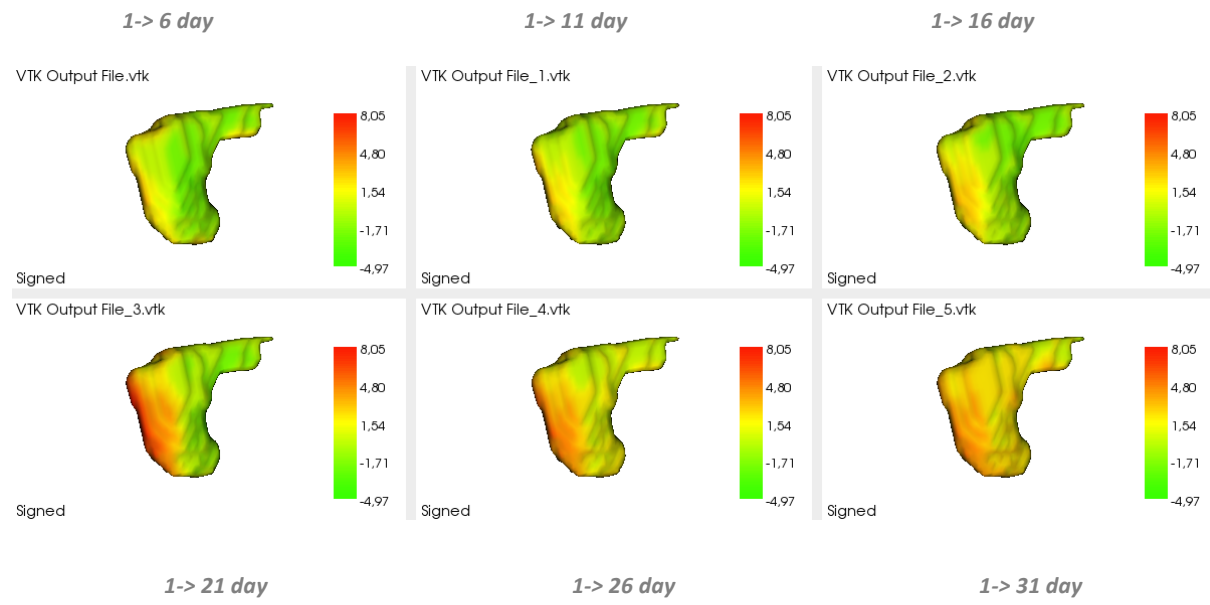


**Left PG**

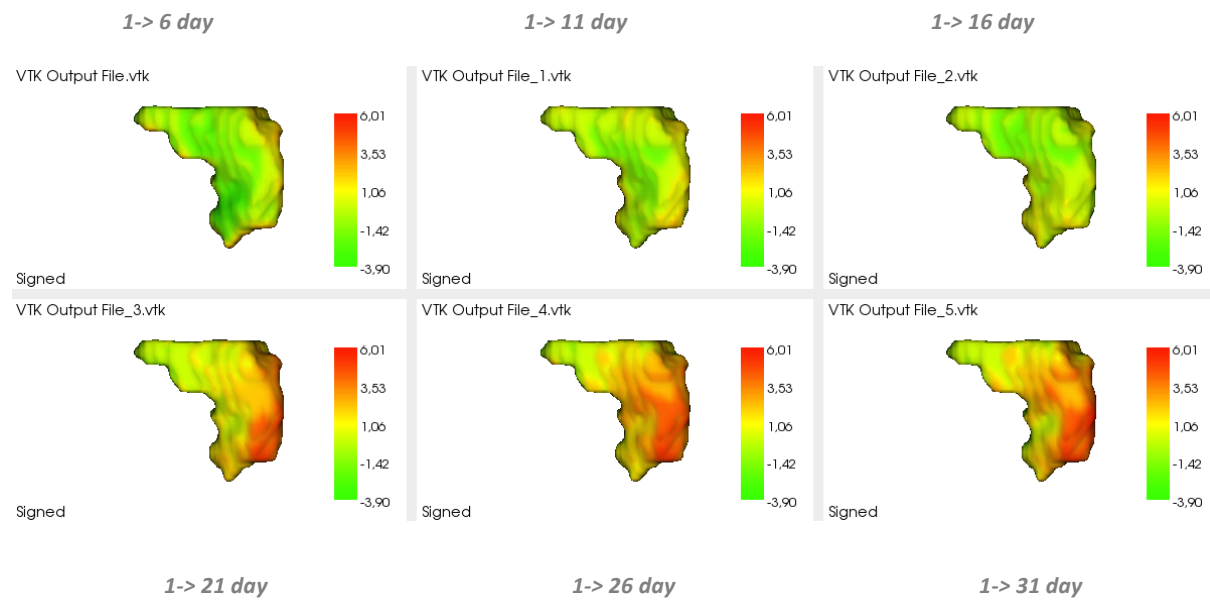


**#Patient 7**

**Right PG**

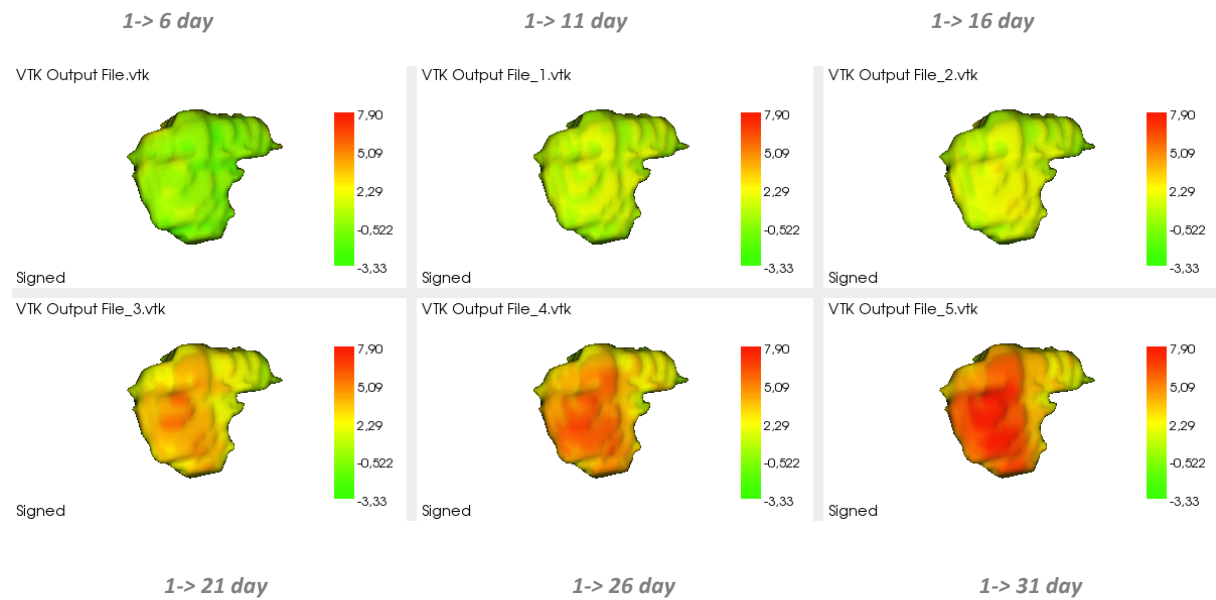


**Left PG**

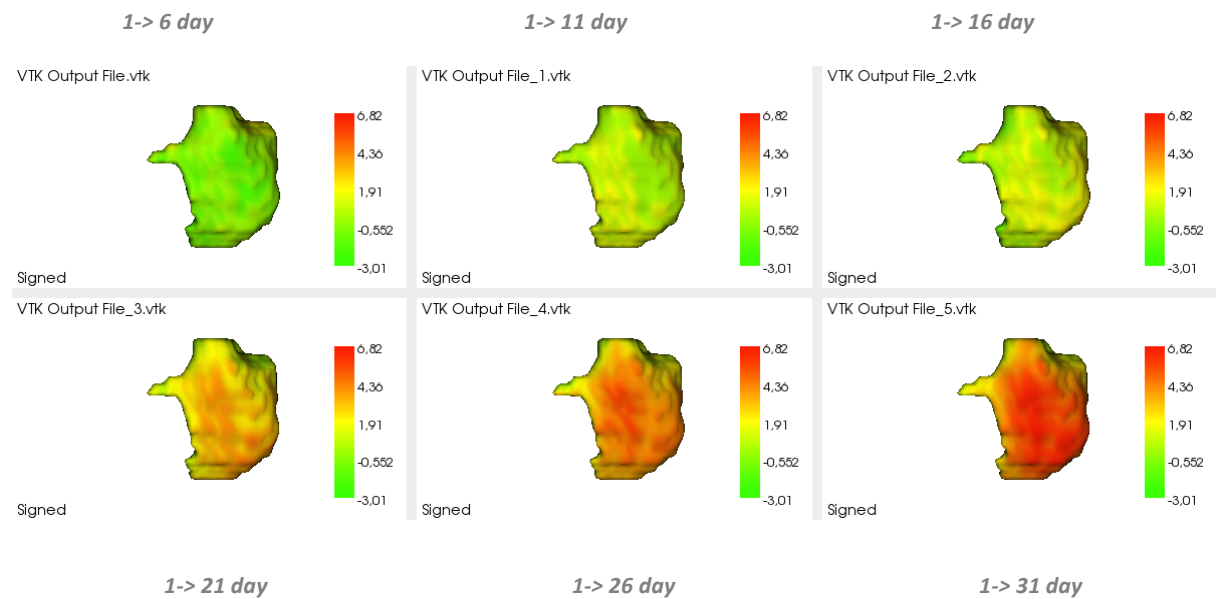


**#Patient 8**

**Right PG**



**Left PG**



## APPENDIX 4

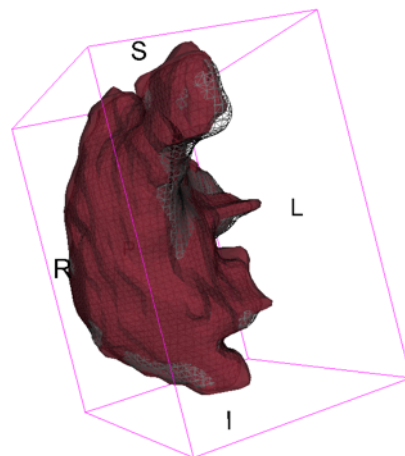
### FEM MODEL RESULTS : MORPHED MESHES

This appendix contains each patient surface mesh representation of the morphed geometries obtained with FEM simulation for both period considered. Wireframes represent simulation results compared with the real pattern of deformation displayed as red surfaces. DICE coefficient values for the compared geometries are reported.

#### *Patient #1*

##### **1 -> 15 th day morphing**

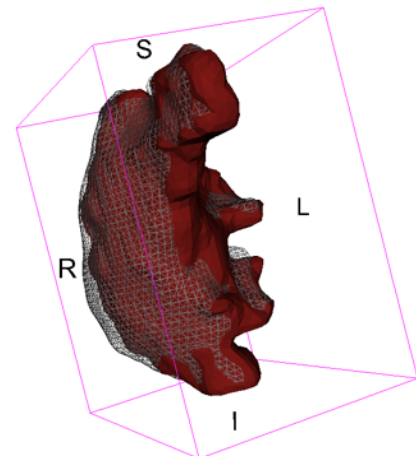
DICE = 0.95



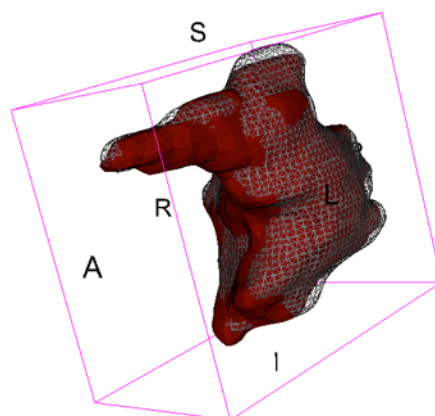
**Right PG**

##### **15 -> 31 day morphing**

DICE = 0.7

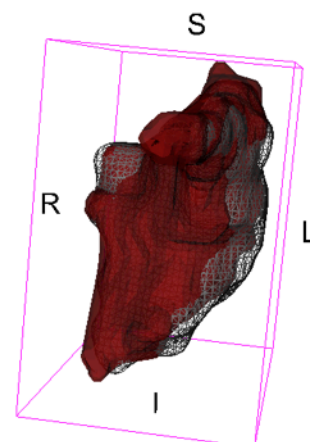


DICE = 0.92



**Left PG**

DICE = 0.72

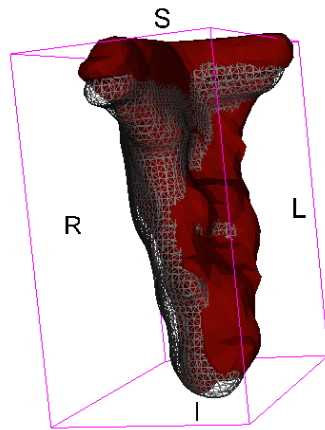


**Patient #2**

**1 -> 15 th day morphing**

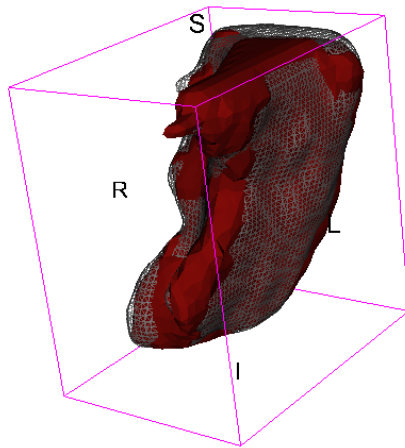
DICE = 0.89

**Right PG**



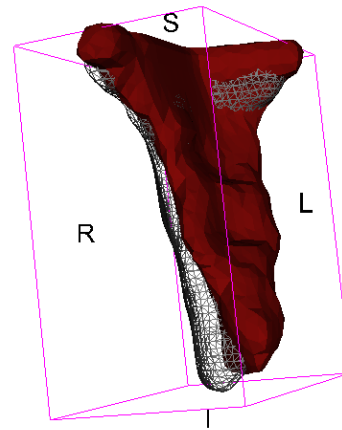
DICE = 0.96

**Left PG**

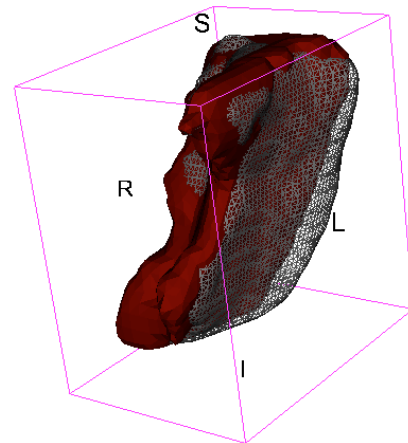


**15 ->31 day morphing**

DICE = 0.68



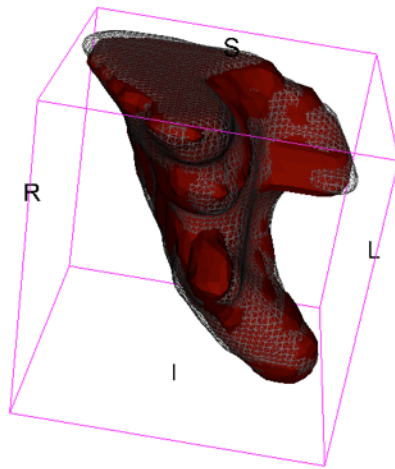
DICE = 0.59



**Patient #3**

**1 -> 15 th day morphing**

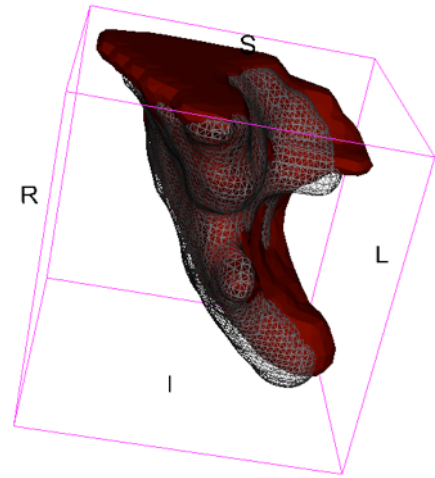
DICE = 0.95



**Right PG**

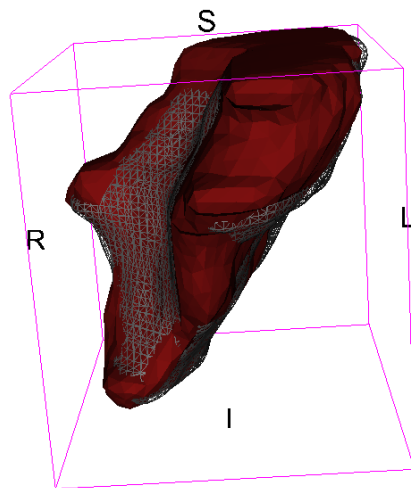
**15 ->31 day morphing**

DICE= 0.68

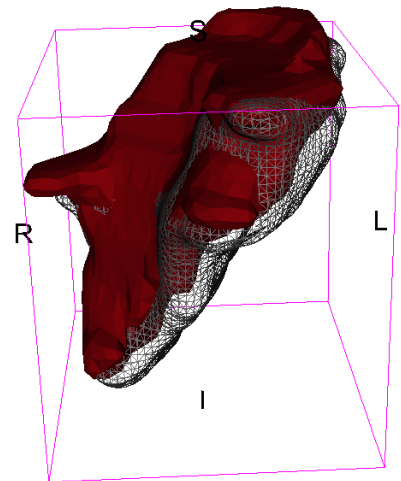


DICE = 0.96

DICE = 0.6



**Left PG**

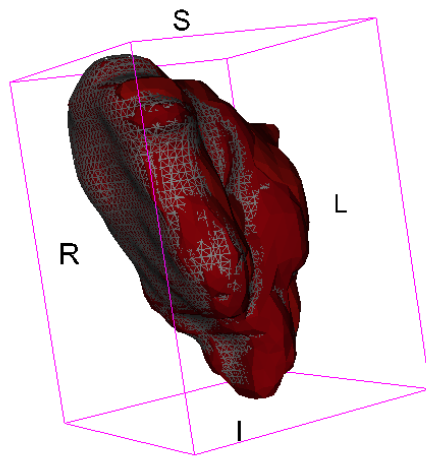




**Patient #4**

**1 -> 15 th day morphing**

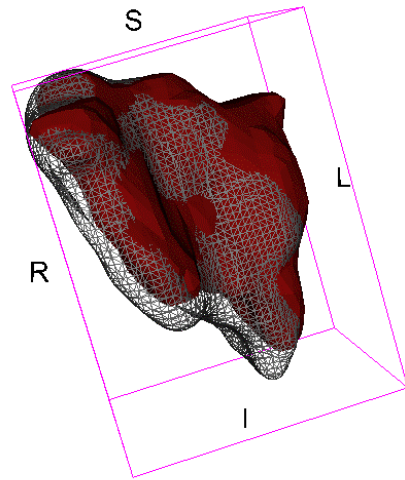
DICE = 0.96



**Right PG**

**15 ->31 day morphing**

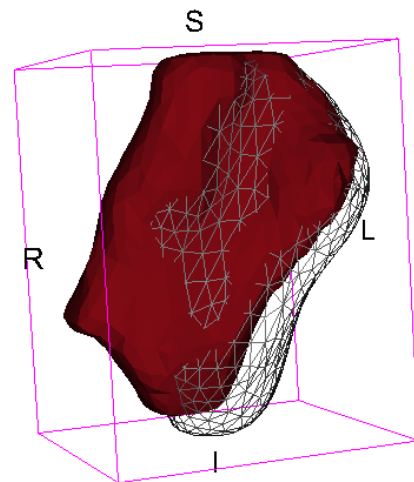
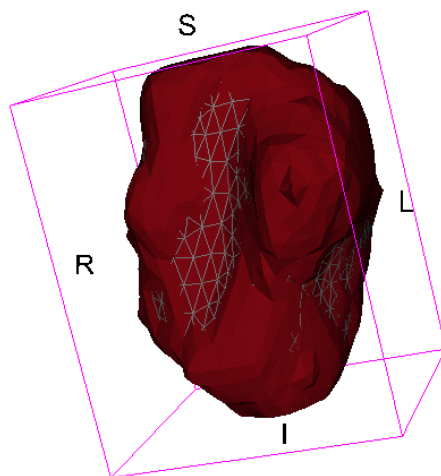
DICE = 0.63



DICE = 0.97

DICE = 0.6

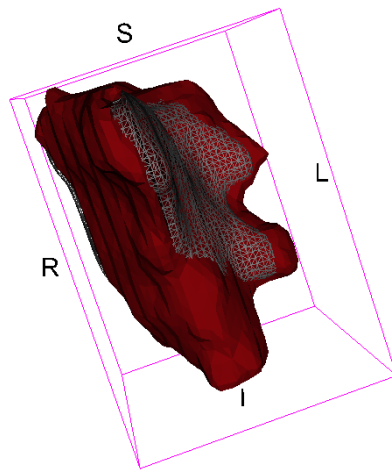
**Left PG**



**Patient #5**

**1 -> 15 th day morphing**

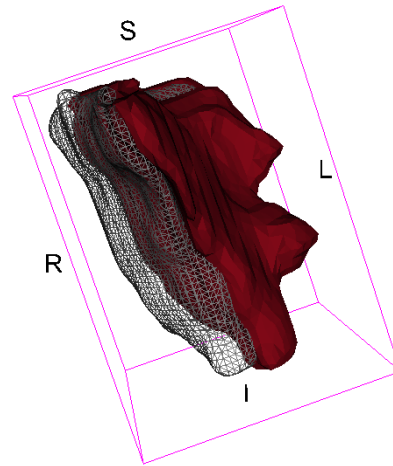
DICE = 0.95



**Right PG**

**15 ->31 day morphing**

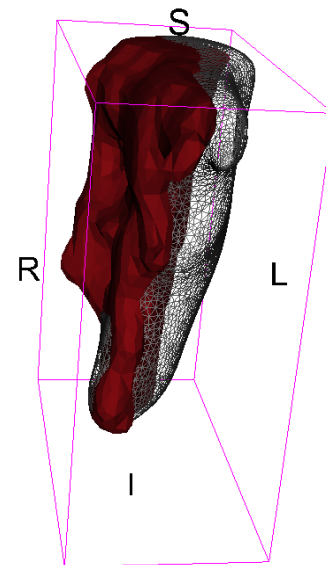
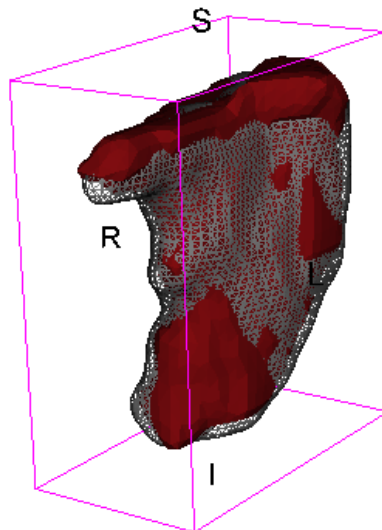
DICE = 0.59



DICE = 0.84

DICE = 0.57

**Left PG**

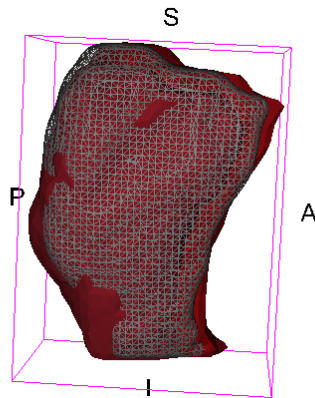


**Patient #6**

**1 -> 15 th day morphing**

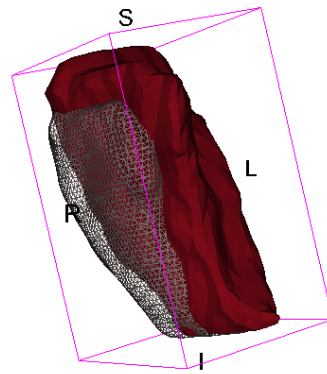
DICE = 0.9

**Right PG**



**15 ->31 day morphing**

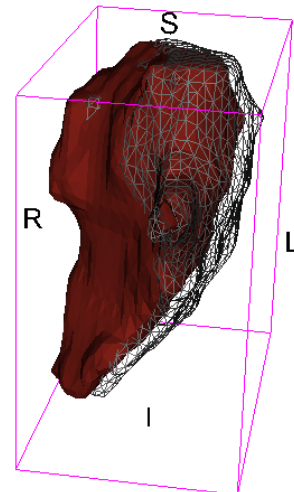
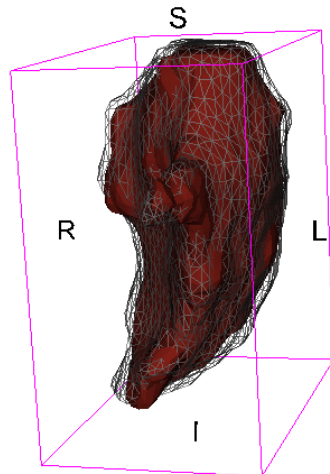
DICE = 0.57



DICE = 0.83

DICE = 0.6

**Left PG**



**Patient #7**

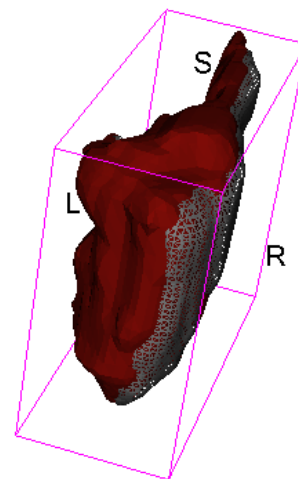
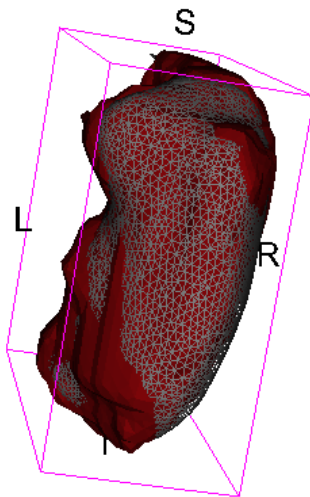
**1 -> 15 th day morphing**

DICE = 0.91

**15 ->31 day morphing**

DICE = 0.74

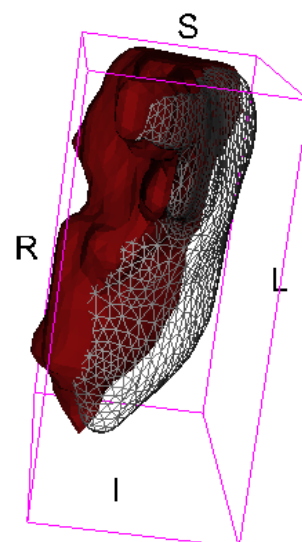
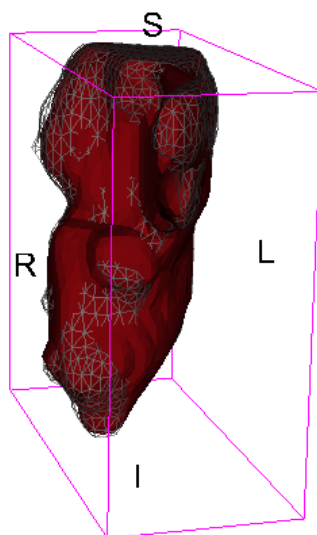
**Right PG**



DICE = 0.86

DICE = 0.56

**Left PG**

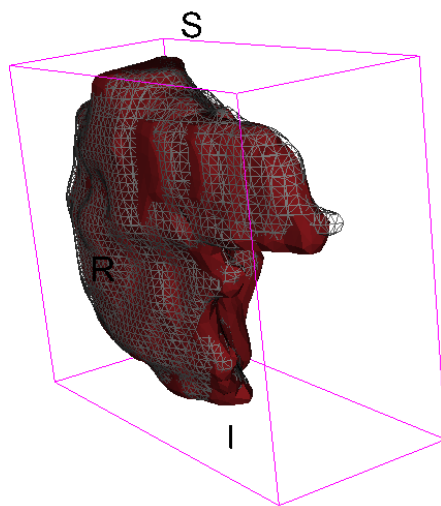


**Patient #8**

**1 -> 15 th day morphing**

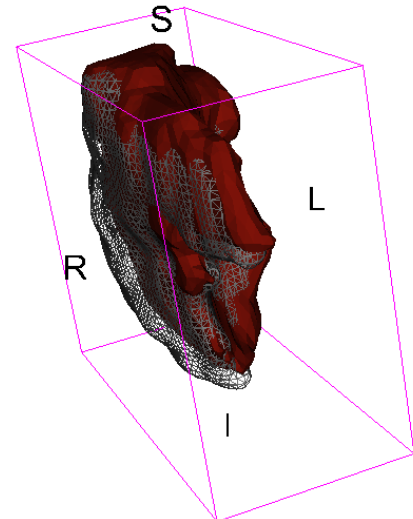
DICE = 0.87

**Right PG**



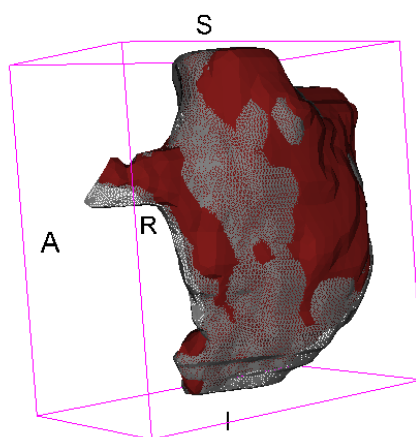
**15 -> 31 day morphing**

DICE = 0.58

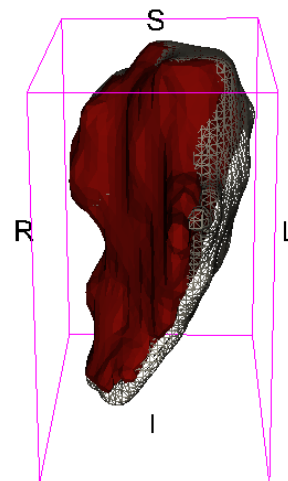


DICE = 0.85

**Left PG**



DICE = 0.59



## APPENDIX 5

### MATHS OF THE STATISTICAL SHAPE BASED MODEL AND MATLAB CODE

#### 3.3 SHAPE BASED STATISTICAL MODEL

Assume that the deformation of parotid glands is known for a number of patients that are our training sample. Our goal is to find the component of the deformation that can be predicted from patient gland starting geometry, based on the premise that anatomy to some extent determines or constraints possible deformation. Statistical shape models (SBE) requires that each patient starting gland geometry has to be expressed with a collection of points (landmarks) arranged in a vector  $\mathbf{s}$  to which corresponds a vector  $\mathbf{q}$  representing displacement vectors defined on their respective landmark.

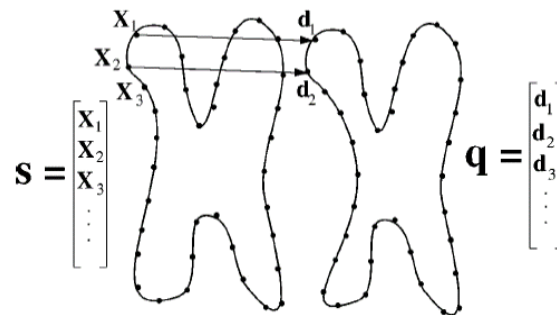


**Figure 85:** A schematic diagram showing a number of landmarks that comprise the vector  $\mathbf{s}$  which represent patient's starting geometry. The vector  $\mathbf{q}$  holds the respective displacement vector.

Consider the vector  $\mathbf{x}$  created by concatenating  $\mathbf{s}$  and  $\mathbf{q}$ . SBE assume that  $\mathbf{x}$  follows a multivariate Gaussian distribution with density  $f(\mathbf{x})$  that it is parameterized by its mean and covariance matrix:

$$\mu = \begin{bmatrix} \mu_s \\ \mu_q \end{bmatrix} \quad (\text{Eq.26}) \quad C = \begin{bmatrix} C_{ss} & C_{sq} \\ C_{sq} & C_{qq} \end{bmatrix} \quad (\text{Eq.27})$$

The probability density function (*pdf*)  $f(\mathbf{x})$ , or equivalently  $\mu$  and  $C$  that parameterize it, can be estimated from a set of cases in which the patient's anatomy, and the way in which this anatomy deforms, are both known. In that case, a number of vectors  $\mathbf{x}_i$ ;  $i = 1; \dots; K$ , are used to calculate  $\mu$  and  $C$ . Let the eigenvectors of  $C$  be denoted by:

$$v_i = \begin{bmatrix} v_{si} \\ v_{qi} \end{bmatrix} \quad i = 1, \dots, K-1 \quad (Eq.28)$$

where  $v_s$  and  $v_q$  are the parts of  $v_i$  corresponding to  $s$  and  $q$ , respectively.

Then,  $x$  can be parameterized as follows:

$$x = \mu + \sum_{i=1}^M \alpha_i v_i \quad M \leq K-1 \quad (Eq.29)$$

from which it follows that

$$s = \mu_s + \sum_{i=1}^M \alpha_i v_{si} \quad (Eq.30) \quad q = \mu_q + \sum_{i=1}^M \alpha_i v_{qi} \quad (Eq.31)$$

The vector  $s$  and  $q$  are then represented entirely by  $\alpha_i$ ,  $i = 1, \dots, M$ , provided that the mean,  $\mu$ , and the eigenvectors of the covariance matrix,  $C$ , of  $f(x)$  have been determined from the training set. Equation can be written in a more compact form as :

$$x = \mu + Va \quad a = [\alpha_1, \dots, \alpha_M]^T \quad (Eq.32)$$

$V$  is a matrix containing the eigenvectors of  $C$  that correspond to the  $M$  largest eigenvalues.

The *pdf* of the coefficient vector  $a$  is given by

$$g(a) = c \exp \left\{ -\sum_{i=1}^M \frac{\alpha_i^2}{2\lambda_i} \right\} \quad (Eq.33)$$

where  $i$  denotes the  $i$ -th eigenvalue of  $C$ , and  $c$  is a normalization constant.

In order to estimate the statistical parameters (mean and covariance matrix), we need a number of training samples for which the vector  $x$  is known, samples for which both the shape and its deformation are known. Let us assume that  $q$  represents the deformation of patient's gland between first and  $i$ -th day of treatment. Let the patient's gland anatomy at the first day of treatment, as determined from the patient's images, be represented by the vector  $s_0$ . Knowing  $s_0$ , our goal is to predict the vector  $q$ , which will determine the deformation for this patient. Since we know  $s_0$ , we can express it in terms of the eigenvectors and the coefficients vector,  $a$ . In order to find the vector  $a$  which represents an expansion of  $s_0$  in terms of  $v_s$  and  $g$ , we solve an optimization problem. Specifically, for a given  $s_0$ , we find the vector  $a$  that minimizes the following objective function:

$$\varepsilon(a) = \|s - s_0\|^2 + w \frac{1}{g(a)} = \left\| \mu_s + \sum_{i=1}^M \alpha_i v_{si} - s_0 \right\|^2 + w \frac{1}{g(a)} \quad (Eq.34)$$

where  $w$  is a relative weighting factor. The first term in Eq.34 seeks vectors that get as close as possible to the patient's observed undeformed anatomy,  $\mathbf{s}_o$ , whereas the second term favors shape representations as in that are likely, according to what has been observed in the training samples.

The solution is found using the *Levenberg–Marquardt (LM)* nonlinear optimization scheme.

Let  $\hat{\mathbf{a}}$  be the vector minimizing  $\varepsilon(\mathbf{a})$ , and let it be expressed as

$$\hat{\mathbf{a}} = [\hat{\alpha}_1, \dots, \hat{\alpha}_M]^T \quad (\text{Eq.35})$$

Therefore, our estimate of  $s_o$  is given by

$$\hat{s}_0 = \mu_s + \sum_{i=1}^M \hat{\alpha}_i v_{si} \quad (\text{Eq.36})$$

At this point, we have determined the coefficients of expansion Therefore we can obtain an estimate of the unknown deformation field

$$\hat{q}_0 = \mu_q + \sum_{i=1}^M \hat{\alpha}_i v_{qi} \quad (\text{Eq.37})$$

#### STATISTICAL SHAPE MODEL: MATLAB CODE

```
%using stlread function to import mesh points obtained as output from SPHARM-PDM
Slicer toolbox we can create for each patient a vector with corrdinates of PG gland
at the start of treatment and a vector with suffix D containing coordinates of PG
gland at the and of treatment
```

```
%concatenating vectors of deformed and non deformed PGs anatomy for each patient
```

```
x1=[vector1,vector1D];
x2=[vector2,vector2D];
x3=[vector3,vector3D];
x4=[vector4,vector4D];
x5=[vector5,vector5D];
```

```
dati=[x1;x2;x3;x4;x5];
```

```
%leave one out procedure
```

```
for i= 1 :5
```

```
    mydati=dati;
```

```
    test=mydati(i,1:3006);
    mydati(i,:)=[];
```

```
C=cov(mydati); % covariance matrix
```

```
[mu,sigma] = normfit(mydati); %mean
```



---

```

[V,D] = eigs(C,100); %eigenvectors
V=V';

myf=@(x)myfunction %import of the defined objective function

ini=0.1*sqrt(diag(D)');
[x,ssq,cnt]=LMFsolve(myf,ini); %use Levenberg-Marquardt scheme to optimize
objective function

                qpred=mu(1,3007:end);

                V=V';
for t=1:100
    %V=V';
    qpred=qpred + ( x(t,1)*V(3007:end,t)' ) ;
end

h=1;
b=size(qpred,2)/3;
for u=1:b
    qp(u,:)=qpred(1,h:h+2);
    h=h+3;
end

h=1;
b=size(test,2)/3;
for o=1:b
    test3(o,:)=test(1,h:h+2);
    h=h+3;
end

qp=real(qp);

%qp is a matrix Nvertex*3 containing predicted displacment

%export output in .txt file format

string2 = ['deformazione_prevista_parotide' num2str(i) '.txt'];
qp=real(qp)
M=[qp(:,1)+test3(:,1),qp(:,2)+test3(:,2),qp(:,3)+test3(:,3)];

dlmwrite(string2,M)

%export output in .stl file format

%stlwrite('def.stl',f4,M)

end

%example of result visualization where CT is a matrix containing real observed
displacement points
scatter3(CT7(:,4),CT7(:,5),CT7(:,6),'r'),hold
on,scatter3(CT7(:,4)+CT7(:,1),CT7(:,5)+CT7(:,2),CT7(:,6)+CT7(:,3),'b'),hold
on,scatter3(qp(:,1)+CT7(:,4),qp(:,2)+CT7(:,5),qp(:,3)+CT7(:,6),'g','*')

```

## LIST OF ABBREVIATIONS

ART: Adaptive Radiation Therapy	ROI: Region of Interest
CM : Continuum mechanics	SNR: Signal to Noise Ratio
CRT : Conformal Radiation Therapy	VMAT: Volumetric Radiation Therapy
CT: Computed Tomography	
CTV : Clinical Target Volume	
DIBH: Deep Inspiration Breath Holding	
DIR: Deformable Image Registration	
DVH: Dose Volume Histogram	
FDM: Finite Difference Method	
FEM: Finite Element Method	
GTV: Gross Tumour Volume	
HT: Helical Tomotherapy	
H&N: Head and Neck	
IGRT: Image guided radiation therapy	
IMRT: Intensity Modulated Radiation therapy	
IORT : Intra Operative Radiation Therapy	
KVCT: Kilo Voltage Computed Tomography	
MRI : Magnetic Resonance Image	
MSD: Mass Spring Damper model	
MVCT:Mega Voltage Computed Tomography	
OAR: Organ at Risk	
OBI: On Board Imaging	
PGs: Parotid Glands	
PS: Parotid Space	
PTV: Planning Target Volume	

## SITOGRAPHY

### MODELING CONSTRUCTION

[HTTPS://WWW.SLICER.ORG](https://www.slicer.org)

<https://www.slicer.org/slicerWiki/index.php/Documentation/4.3/Training>

<http://wiki.slicer.org/slicerWiki/index.php/Documentation/Nightly/Extensions/ModelToModelDistance>

<http://wiki.slicer.org/slicerWiki/index.php/Documentation/Nightly/Modules/DiceComputation>

<http://wiki.slicer.org/slicerWiki/index.php/Documentation/Nightly/Extensions/CurveMaker>

<https://www.comsol.it>

<http://cdn.comsol.com/documentation/5.1.0.145/IntroductionToCOMSOLMultiphysics.pdf>

<https://www.comsol.com/multiphysics/finite-element-method>

### LITERATURE SEARCH

<http://www.ncbi.nlm.nih.gov/pubmed>

<http://www.sciencedirect.com>

<http://www.medphys.org>

<http://medicalphysicsresearch.weebly.com/2013-et-al.html>

<http://www.raysearchlabs.com/products/>

---

## BIBLIOGRAPHY

- [1] Langen KM., Jones DT. et al. , «Organ motion and its management.», *Int. J. Radiat. Oncol. Biol. Phys.*, n. 50(1) (May 2001): 265-78.
- [2] Ciarmatori A. , «Dose accumulation in head and neck cancer patients: through implementation of Adaptive Radiotherapy in clinical practice» , Bologna: Medical Physics School University of Bologna, 2015.
- [3] Castadot P. et al. , «Adaptive radiotherapy of head and neck cancer.», *Semin. Radiat. Oncol.*, n. 20(2) (April 2010): 84-93.
- [4] Scalco E. et al. , «Texture analysis for the assessment of structural changes in parotid glands induced by radiotherapy.», *Radiother. Oncol.*, n. 109(3) (Dec 2013): 384-7.
- [5] Teshima K. et al. , « Histopathological Changes in Parotid and Submandibular Glands of Patients Treated with Preoperative ChemoradiationTherapy for Oral Cancer.» *J. Radiat. Res.*, n. 53 (2012): 492–496 .
- [6] Xiaofeng Y. et al. , «Ultrasound GLCM texture analysis of radiation-induced parotid-gland injury in head-and-neck cancer radiotherapy: An in vivo study of late toxicity» , *Medical Physics* ,n. 39(9) (Sept 2012): 5732-101.
- [7] Fiorino C., Maggiulli E., Broggi S. et al. «Introducing the Jacobian-volume-histogram of deforming organs: application to parotid shrinkage evaluation.» *Phys Med Biol.*, n. 56(11) (Jun 2011): 3301-12.
- [8] Chan YH et al. ,«Human Salivary Gland Acinar Cells Spontaneously Form Three-Dimensional Structures and Change the Protein Expression Patterns.», *Journal of Cellular Physiology*, n. 226(11) (Nov 2011): 3076-85.
- [9] Someya M. et al. , « Impact of conventional radiotherapy on health-related quality of life and critical functions of the head and neck.», *Jpn. J. Clin. Oncol.* , n. 33 (2003): 336-40.
- [10] Kielbassa AM et al. ,«Radiation-related damage to dentition.», *Lancet Oncol* , n.7(4) (2006): 326-35.
- [11] Maffei N. , «Reti Neurali e Modelli Fisico-Predittivi: dati clinici e analisi di trattamenti in Tomotherapy.»,Bologna: Physics Dpt. University of Bologna, 2014.
- [12] Broggi S. et al. ,«A two-variable linear model of parotid shrinkage during IMRT for head and neck cancer.», *Radiother. Oncol.*, n. 94(2) (Feb 2010): 206-12.
- [13] Fiorentino A. et al. ,«Parotid gland volumetric changes during intensity-modulated radiotherapy in head and neck cancer.», *Br. J. Radiol.*, n. 85, (Oct 2012): 1415-19.

- 
- [14] Teshima K. et al., «Radiation-induced parotid gland changes in oral cancer patients: correlation between parotid volume and saliva production.», *Jpn. J. Clin. Oncol.*, n. 40(1) (Jan 2010): 42-6.
- [15] Fiorino C. et al., «Density variation of parotid glands during IMRT for head-neck cancer: correlation with treatment and anatomical parameters.», *Radiother. Oncol.*, n. 104(2) (Aug 2012): 224-9.
- [16] Vecchi C. , «Scripting Automation e Modelli Bayesiani: applicazioni cliniche in radioterapia e sviluppo di tecniche innovative per Adaptive Radiation Therapy. » , Bologna: Physics Dpt. University of Bologna, 2014.
- [17] Ayache N. and H.Delingette editors, «International Symposium on Surgery Simulation and Soft Tissue Modeling » , LNCS 2673, Juan-Les-Pins, France, jun 2003 , Springer-Verlag , 386 pages.
- [18] Botsch M. , «Polygon Mesh Processing.» , A.K. Peters/CRC Press, 2007.
- [19] Ruchala KJ et al. , «Megavoltage CT on a tomotherapy system.» , *Phys. Med. Biol.* , n.44 (1999): 2597–2621.
- [20] Pluim J.P.W. et al. , « Mutual-information-based registration of medical images: a survey.» , *IEEE Transactions on Medical Imaging* , n.22 (Aug 2003): 986 - 1004.
- [21] Weistrand O. et al. ,«The ANACONDA algorithm for deformable image registration in radiotherapy.», *Medical Physics*, n.42 (2015).
- [22] Fedorov A. et. al, «3D Slicer as an Image Computing Platform for the Quantitative Imaging Network.», *Magnetic Resonance Imaging* n. 30(9) (2012): 1323-41.
- [23] William E.L., Harvey E.C. ,«Marching cubes: a high resolution 3D surface construction algorithm.», *Computer Graphics* , n.21(4) (July 1987): 163:169.
- [24] Aspert N. et al., «MESH: Measuring Errors between Surfaces using the Hausdorff distance», *IEEE International conference in multimedia and Expo*,n.1 (2002): 705-708.
- [25] Lee C., Langeon K M, Lu W, «Evaluation of geometric changes of parotid glands during head and neck cancer radiotherapy using daily MVCT and automatic deformable registration» ,*Radiotherapy and Oncology*,n.89 (2008): 81-88.
- [26] Freutel M. et al., «Finite element modeling of soft tissues: Material models, tissue interaction and challenges» , *Clinical Biomechanics*, Elsevier, April 2014
- [27] Kenedi R. M. et al. ,«Tissue Mechanics » , *Phys. Med. Biol.*, n.20(5) (1975): 699-717.
- [28] Shi, Hongjian, «Finite element modeling of soft tissue deformation. » , (2007) *Electronic Theses and Dissertations*. Paper 1321.
- [29] Roger W. ,« Multiphysics Modeling Using COMSOL®: A First Principles Approach » , Jones & Bartlett Learning, 1 edition (December 21, 2009)
- [30] Kermal Arda et al. , « Quantitative assessment of normal soft-tissue elasticity using shear-wave ultrasound elastography » , *AJR Am J Roentgenol*, n. 197(3) (Sept 2011):532-6.

- 
- [31] Benzley, Perry et al. , «A comparison of all hexagonal and all tetrahedral finite element meshes for elastic and elasto-plastic analysis (1995) », In Proceedings, 4th International Meshing Roundtable.
- [32] Guidi G, Mistretta G M, Maffei N et al., «Dose accumulation and Organ deformation for IGRT and Adaptive RT: possible incompatibility in radiation oncology, research and prospects for the new era», AIFM 2013
- [33] Vecchi C., Guidi G., Maffei N. et al., « Deformable registration using Python scripting for clinical automation», ESTRO 33 , 2014, (in press).
- [34] Maffei N., Guidi G., Vecchi C. et al., « Warping methods for Tomotherapy and IGRT: challenge and predictive analysis in clinical practice, ESTRO 33, 2014, (in press).
- [35] Maffei N., Guidi G., Vecchi C. et al., «An Artificial Neural Network To Predict Time Of Replanning For Tomotherapy Treatments. », ICMMB-XIX, 2014.
- [36] Vecchi C, Guidi G, Maffei N et al., « Scripting Automation And Biomechanical Modeling For Adaptive Radiation Therapy. », ICMMB-XIX, 2014.
- [37] Maffei N., Guidi G., Vecchi C. et al. « Predictive Neural Network for parotid glands deformation using IGRT and dose warping systems. », Medical Physics. , n.41(177) ,2014.
- [38] Styner M., Oguz I., Xu S., et al., « Framework for the Statistical Shape Analysis of Brain Structures using SPHARM-PDM. »,The insight journal. ,n.(1071) :242-250. , 2006
- [39] Davatzikos C. at al. , « A Framework for Predictive Modeling of Anatomical Deformations», IEEE Transactions on medical imaging, n. 20(8) (Aug 2001) : 836-43
- [40] Cory Quammen, Chris Weigle C., Russ Taylor, «Boolean Operations on Surfaces in VTK Without External Libraries»,VTK Journal -2011 January ,December Submissions.
- [41] Lohr. F., «Deep Inspiration Breath Hold—Based Radiation Therapy: A Clinical Review» , Radiother Oncol., n.94(3) (March 2016) :478-92
- [42] Guidi G.,«Metodi predittivi per adaptive radiation therapy: effetti del movimento d'organo, degli algoritmi di registrazione deformabile e dell'accumulo di dose»,Bologna: Physics Dpt. University of Bologna, PhD thesis, 2016.
- [43] Konings AW et al., «On the mechanism of salivary gland radiosensitivity»,Int J Radiat Oncol Biol Phys. 2005 Jul 15;62(4):1187-94.
- [44] Barker et al. ,«Quantification of volumetric and geometric changes occurring during fractionated radiotherapy for head and neck cancer using an integrated CT/linear accelerator system», Int J Radiat Oncol Biol Phys. 2004 Jul 15;59(4):960-70.
- [45] Robar et al , «Spatial and dosimetric variability of organs at risk in head-and-neck intensity-modulated radiotherapy. », Int J Radiat Oncol Biol Phys. 2007;68:1121-30.
- [46] Hansen et al , «Repeated CT imaging and replanning during the course of IMRT for head-and-neck cancer.», Int J Radiat Oncol Biol Phys. 2006; 64:355–62

- [47] Vásquez Osorio et al. , «Local anatomical changes in parotid and submandibular glands during radiotherapy for oropharynx cancer and correction with dose, studied in detail with non-rigid registration. » Int J Radiat Oncol Biol Phys 2008;70:875–82
- [48] Lee et al. , «Assessment of parotid gland dose changes during head and neck cancer radiotherapy using daily megavoltage computed tomography and deformable image registration. »,Int J Radiat Oncol Biol Phys 2008;71:1563–7

## ACKNOWLEDGEMENT

There are a number of people to whom I am indebted for their help in the preparation of this thesis. It is a pleasure to convey my gratitude to them all in my humble acknowledgment.

I gratefully acknowledge my supervisor Prof. Giuseppe Baldazzi for giving me the opportunity to develop this work in collaboration with University of Bologna and the "Azienda Universitaria Ospedaliera di Modena " Policlinico.

I gratefully acknowledge my thesis advisor Dr. Gabriele Guidi, Medical Physics department responsible, for his valuable advice , supervision, encouragement , support and guidance from the very early stage of this work.

I am grateful to the Medical Physics department director Dr. Tiziana Costi and to the Radiation Oncology department director Prof. Frank Lohr.

My sincere thanks go to all the medical physicians of the department for the kindness and assistance in this experience and to Dr. Nicola Maffei, researcher in charge, for his constant support and active interest.

Last but not the least I would like to thank my family and friends for their unending support and encouragement.